



JAGIELLONIAN UNIVERSITY  
IN KRAKOW

# Long-Range Interactions on Optical Lattices

by

Michał Maik

A thesis submitted in partial fulfillment for the  
degree of Doctor of Philosophy

in the

Marian Smoluchowski Institute of Physics  
Department of Atomic Optics

February 2014

JAGIELLONIAN UNIVERSITY

# *Abstract*

Marian Smoluchowski Institute of Physics

Department of Atomic Optics

by Michał Maik

In this thesis we discuss several different methods that can be used to create the elements of future quantum computers. The main focus will be on cold atomic gases in optical lattices and trapped ions. Each of these systems has the capability of having long-ranged dipolar interactions and can be studied by at multiple of different methods. First we will describe a very simple system of soft-core dipolar bosons on an optical lattice ring. The key element of this study will be to examine the long-ranged behavior of the dipoles on a true ring topology and to examine the behavior of different polarizations. We will use exact diagonalization to analyze this system. Next, we will look at trapped ions on a two dimensional triangular lattice and study the effects of these frustrated systems. Again we will be studying the long ranged nature of the dipolar interactions (and also long-ranged hopping). We will do this by using QMC simulations. Finally we continue to use QMC methods to examine a two dimensional square lattice system filled with soft-core bosons. The unique characteristic of this section will be that the Hamiltonian will not only contain the dipole-dipole term but will also have a density dependent hopping parameter. This additional hopping term can be of like or opposite sign with the regular hopping which will influence the behavior of the entire phase diagram.

# *Acknowledgements*

First of all I would like to thank my supervisor, Prof. Jakub Zakrzewski for taking me on as one of his PhD students. Throughout my doctorate he has kept me on track and focused even though I am sure this was not an easy task. I am sure that I have tried his patience on more than one occasion. I would also like to thank Prof. Maciek Lewenstein, who was my supervisor during my time in Spain, for his collaborations on several projects. His opinions and wealth of knowledge were very useful when starting a new topic. Thanks to the two of them I have learned a great amount over the last 4 years.

I would like to thank Prof. Krzysztof Sacha for joining in on many of our discussions and providing his input and expertise to our work. His thoughts and opinions were very insightful.

I would like to thank the thesis committee for taking the time to read through and assess this work.

I would like to thank my friends and coworkers at Jagiellonian University, especially Kasia Targońska, Bartosz Głowacz, and Marcin Płodzien for our many scientific and non-scientific discussions. They made coming to the office an actual pleasure.

I would like to thank all my friends and coworkers at ICFO, especially Omjoti Dutta, and Philipp Hauke for the cooperation on several projects. Their help and guidance throughout our many discussions allowed me to do some of the best work during my time as a PhD student.

I would like to thank Fiona Beck, Sam Reid, Silke Diedenhofen, Julia Fekete, JP Szczepanik, and John Hainsworth (AKA the Castelldefels Posse) for making my time in Spain as memorable as possible. Their friendship has really enriched my life.

I would like to thank my family for supporting me when I decided to embark across the ocean and begin my PhD in Poland.

I would like to thank the KrakUF Ultimate Frisbee team for giving me something to be passionate about outside of my studies. Among them I not only found great teammates but also many great friends.

A final thanks goes to Marcelina Zengel. Had I not met her I probably would have finished this PhD much earlier. However our conversations have helped to keep me sane throughout the last few months of my work.

# Contents

<b>Abstract</b>	<b>i</b>
<b>Acknowledgements</b>	<b>ii</b>
<b>List of Figures</b>	<b>vi</b>
<b>List of Tables</b>	<b>viii</b>
<b>1 Introduction</b>	<b>1</b>
1.1 Quantum computing . . . . .	1
1.2 Ultra-cold dipolar atoms . . . . .	2
1.3 Trapped ions . . . . .	10
1.4 Methods . . . . .	12
1.5 Thesis outline . . . . .	13
<b>2 Dipolar bosons on an optical lattice ring</b>	<b>15</b>
2.1 Introduction . . . . .	15
2.2 Exact diagonalization . . . . .	16
2.3 Symmetries of the EBHM . . . . .	19
2.4 Observables . . . . .	22
2.5 Results . . . . .	26
2.5.1 Polarized out of plane . . . . .	26
2.5.2 Polarized in plane . . . . .	32
<b>3 Hard-core dipolar bosons on a triangular lattice</b>	<b>40</b>
3.1 Introduction . . . . .	40
3.2 1D review and results . . . . .	43
3.3 2D results . . . . .	46
3.3.1 Vanishing tunneling . . . . .	50
3.3.2 Low-temperature phase diagram at finite tunneling . . . . .	51
3.3.3 Finite temperature results . . . . .	59
3.4 Conclusion . . . . .	62

---

<b>4</b>	<b>Density dependent tunneling in the extended Bose-Hubbard model</b>	<b>63</b>
4.1	Introduction . . . . .	63
4.2	The model . . . . .	65
4.2.1	Considered observables . . . . .	67
4.3	Ground-state phase diagrams . . . . .	69
4.3.1	Phase diagrams at vanishing density-dependent tunneling . .	70
4.3.1.1	Phase diagram at strong on-site repulsion ( $U = 20$ )	70
4.3.1.2	Phase diagram at moderate on-site repulsion ( $U = 5$ )	72
4.3.2	Phase diagrams at finite density-dependent tunneling . . . .	74
4.3.2.1	Phase diagram at strong on-site repulsion . . . . .	75
4.3.2.2	Moderate on-site repulsion ( $U = 5$ ) . . . . .	79
4.4	Conclusions . . . . .	82
<b>5</b>	<b>Conclusion</b>	<b>84</b>
<b>A</b>	<b>Guide to long-ranged interactions using ALPS</b>	<b>89</b>
A.1	Building the lattice . . . . .	90
A.2	Building the model . . . . .	95
A.3	Building the parameter file . . . . .	97
	<b>Bibliography</b>	<b>100</b>

# List of Figures

1.1	An illustration of the Mott insulator to superfluid phase transition.	3
1.2	An illustration of dipole-dipole interactions.	6
1.3	Raman transition between hyperfine states.	11
2.1	Superfluid fraction, condensate fraction, and variance of occupation for different $U$ values of dipoles polarized perpendicular to the ring.	27
2.2	Geometry of an 8 site ring.	33
2.3	Graphs for a shallow lattice, $U/J = 1$ , with polarization parallel to the ring.	34
2.4	Superfluid fraction for different $U/J$ for dipoles polarized parallel to the ring.	35
2.5	Avoided level crossing for $U/J = 6$ .	36
2.6	The mean occupation and the variance of type-I states for $U/J = 6$ and the $V/U$ dependence of the condensate fraction.	37
2.7	Occupation and variance of type-I sites for $U/J = 10$ and $U/J = 20$	38
3.1	Phase diagram of the 1D system with dipolar interactions with nearest-neighbor tunneling and dipolar tunneling.	44
3.2	An illustration of frustration on a triangular and square lattice.	48
3.3	Density graphs for different system sizes and different temperatures.	51
3.4	Density and superfluid graphs for short-ranged, dipolar, and long-ranged interactions.	52
3.5	Cuts at $\mu/J = 0$ for short-ranged, dipolar, and long-ranged interactions.	54
3.6	Cuts at $\theta = -0.15$ for short-ranged, dipolar, and long-ranged interactions.	56
3.7	Density and superfluid graphs for short-ranged interactions at $\theta = -0.28$ and dipolar interactions at $\theta = -0.23$ .	57
3.8	Density and superfluid graphs for short-ranged, dipolar, and long-ranged interactions with the sign problem.	58
3.9	Stiffness, structure factor, and supersolid regions for different interactions with changing temperature.	60
3.10	The melting of crystal lobes for different interactions.	61
4.1	The phase diagram in the $\rho - V$ parameter space without density-dependent tunneling term.	70
4.2	Density and structure factor graphs for $U = 20$ and $V = 3.0$ .	71

---

4.3	Density and structure factor graphs for $U = 5$ with $V = 3.0$ , $V = 4.5$ , and $V = 6.0$ . . . . .	73
4.4	The phase diagrams for $U = 20$ at finite $T$ . . . . .	74
4.5	Density and structure factor graphs for $U = 20$ with $T = -0.3$ , $T = -0.5$ , and $T = -0.6$ . . . . .	76
4.6	Density graph for $U = 20$ and $T = 1.0$ with long-ranged interactions. . . . .	77
4.7	Density graph for $U = 20$ and $T = -1.0$ with long-ranged interactions. . . . .	78
4.8	Phase diagrams for $U = 5$ and finite $T$ . . . . .	79
4.9	Density and structure factor graphs for $U = 5$ with $T = -0.3$ , $T = -0.4$ , and $T = -0.8$ . . . . .	80
4.10	Density graph for $U = 5$ and $T = -0.6$ with long-ranged interactions. . . . .	81
A.1	A triangular lattice with 5 nearest neighbor interactions. . . . .	94

# List of Tables

2.1	Probability distributions for 8 sites with dipoles polarized perpendicular to the ring. . . . .	30
2.2	Probability distributions for 9 sites with dipoles polarized perpendicular to the ring. . . . .	32
2.3	Probability distributions at sites of type I and II for dipoles polarized parallel to the ring. . . . .	35

*For Michał Maik, without him this thesis would never  
have been written.*

# Chapter 1

## Introduction

### 1.1 Quantum computing

The concept of the quantum simulator was first proposed in a paper by Richard Feynman in 1982 [1]. In it Feynman claims that one can construct a many-body system which would imitate a different quantum mechanical system. In other words one needs to create a probabilistic simulator in order to properly represent probabilistic reality (quantum mechanics). If we are able to implement such a simulator then we would be able to precisely study this probabilistic nature of quantum mechanical systems as well as the physical world. This idea of a quantum simulator could then be used to create a universal quantum computer. This quantum computer would perform operations on data in the same manner as a classical computer but instead of manipulating classical bits it would utilize qubits (or quantum bits) and quantum logic gates instead of classical ones [2]. Using qubits allows one to employ the special properties of quantum mechanics such as superposition and entanglement in order to perform different calculations. Of course the function of such a quantum computer would be limited to very specific tasks that a classical computer would not be capable of accomplishing in polynomial time. For example a quantum computer would be able to do extremely

fast factorization of very large numbers which could then be used for decryption purposes by using the Shor algorithm [3].

Many scientists are currently looking at different ways of constructing a universal quantum computer that will be capable of accurately simulating the quantum world. However the field is still at a very young stage and there are many obstacles still in the way of creating such a machine. There are many theories on how to make such a device but none of them have been shown to be ideal candidates. One of the most basic, yet important, elements is finding the best way to represent the qubits. Some of the suggestions that exist are: spin-1/2 particles, hard-core bosons, internal states of trapped ions, and many others. In this thesis we will focus mainly on two of these possibilities: cold atoms (in optical lattices) and trapped ions. More specifically we will focus on the behavior of long-ranged dipolar interactions in optical lattices and their influences on different quantum mechanical systems.

## 1.2 Ultra-cold dipolar atoms

Let's begin with a quick review of cold atomic gases. In 1995, Eric Cornell and Carl Wieman produced the first ever Bose-Einstein condensate (BEC) from rubidium  $^{87}\text{Rb}$  atoms at the University of Colorado in Boulder [4]. This experiment became the first major step in the development of the study of cold atoms. This field grew rapidly and along the way there were many great discoveries such as the creation of a fermionic condensate [5] and the BEC-BCS crossover [6]. Another major milestone was reached, when in 2002 Marcus Greiner and his associates showed experimentally, for the first time, the transition from a Mott insulator to a superfluid in a three dimensional optical lattice [7]. In Fig. 1.1 we can see a graphical representation of the two phases from the transition on a two dimensional lattice. Fig. 1.1 (a) shows the superfluid state where the particles are delocalized across the whole lattice due to a strong kinetic energy. Fig. 1.1 (b) shows the Mott insulating state that is now dominated by the interaction energy which causes

complete localization and therefore allows only a single particle to exist in an individual site.

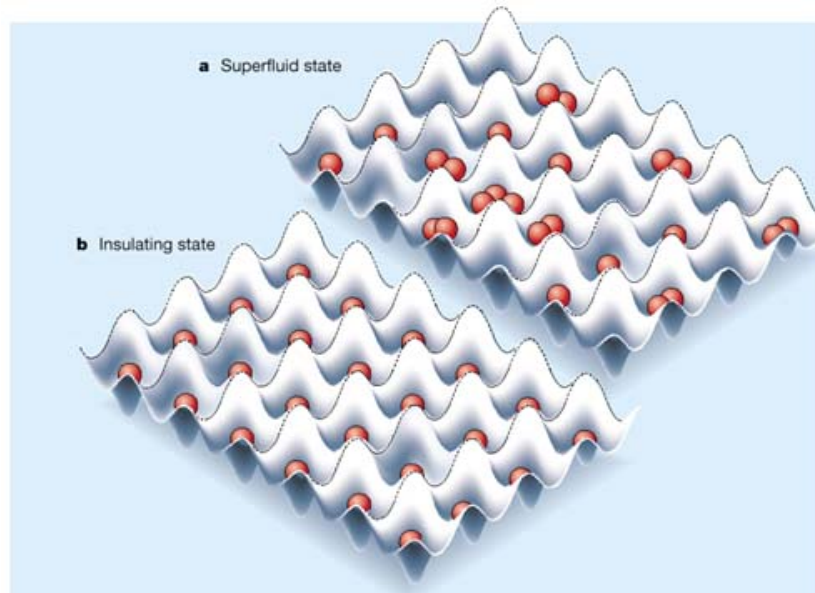


FIGURE 1.1: An illustration that helps visualize the behavior of the superfluid and Mott insulating phases. In (a) we see that in the superfluid phase the particles are delocalized across the lattice and that multiple particles can occupy a single site. In (b), which shows the Mott insulating phase, we have a single particle in a single site. This phase has strong localization and is incompressible.

The diagram is taken from [7].

Such an optical lattice as is shown in Fig. 1.1 can be constructed by using sets of counter propagating laser beams that form a series of periodic potential wells. These lattices can be formed into one, two, or three dimensional objects that can take on many geometries. The potential wells that form can then be used to trap atoms (that have been properly cooled) within their minimums. The result is an arrangement of trapped atoms resembling a crystal lattice. One of the great characteristics of these optical lattice systems is their incredibly high tunability. Just by manipulating amplitudes and angles of the beams one is able to easily change the depth and spacing of the lattice [8]. The celebrated Bose-Hubbard model is used to explain the interactions that can be achieved between the particles on an optical lattice.

The standard Hubbard model was first proposed by John Hubbard in 1963 in order to describe transitions between conducting and insulating systems [9]. This

model is excellent for approximating fermions on an optical lattice. Later that same year, H. A. Gersch modified the model to describe bosons interacting on an optical lattice [10]. This is now called the Bose-Hubbard model and it can be derived from the following Hamiltonian:

$$\begin{aligned}
H &= \int d\mathbf{r} \psi^\dagger(\mathbf{r}) \left[ \frac{p^2}{2m} + V_{latt.}(\mathbf{r}) \right] \psi(\mathbf{r}) \\
&+ \int \int d\mathbf{r} d\mathbf{r}' \psi^\dagger(\mathbf{r}) \psi^\dagger(\mathbf{r}') V_{int}(\mathbf{r}, \mathbf{r}') \psi(\mathbf{r}) \psi(\mathbf{r}') \\
&- \mu \int d\mathbf{r} \psi^\dagger(\mathbf{r}) \psi(\mathbf{r})
\end{aligned} \tag{1.1}$$

where  $\psi(\mathbf{r})$  are the bosonic field operators,  $V_{latt.}$  is the potential of the optical lattice, and  $V_{int}$  is the two particle interaction energy. Now we transform the Hamiltonian to a polynomial of bosonic ladder operators. This can be done by writing the field operator  $\psi(\mathbf{r})$  as

$$\psi(\mathbf{r}) = \sum_i b_i w(\mathbf{r} - \mathbf{r}_i) \tag{1.2}$$

$$\psi^\dagger(\mathbf{r}) = \sum_i b_i^\dagger w^*(\mathbf{r} - \mathbf{r}_i) \tag{1.3}$$

where  $b_i$  and  $b_i^\dagger$  are the bosonic ladder operators acting on lattice site  $i$  and fulfilling

$$[b_i, b_j^\dagger] = \delta_{ij}, \quad [b_i^\dagger, b_j^\dagger] = 0, \quad [b_i, b_j] = 0 \tag{1.4}$$

and  $w(\mathbf{r} - \mathbf{r}_i)$  are the Wannier functions, which are defined as a complete orthonormal function basis

$$\int d\mathbf{r} w^*(\mathbf{r} - \mathbf{r}_i) w(\mathbf{r} - \mathbf{r}_j) = \delta_{ij} \tag{1.5}$$

$$\sum_i w^*(\mathbf{r} - \mathbf{r}_i) w(\mathbf{r}' - \mathbf{r}_i) = \delta(\mathbf{r} - \mathbf{r}') \tag{1.6}$$

and are localized at lattice sites.

In a spatially periodic system different energy bands exist, so there are Wannier functions for every band. In our systems the temperature is approximately zero

(or low enough to stay in the ground state), so we can consider all bosons to be in the lowest band. Otherwise we would have to distinguish between different bands.

Inserting the representation of the field operator (1.2) and (1.3) into the Hamiltonian (1.1) yields

$$H = - \sum_{i,j} J_{i,j} b_i^\dagger b_j + \sum_{i,j,k,l} V_{i,j,k,l} b_i^\dagger b_j^\dagger b_k b_l - \mu \sum_i n_i \quad (1.7)$$

where

$$J_{i,j} = - \int d\mathbf{r} w^*(\mathbf{r} - \mathbf{r}_i) \left( \frac{p^2}{2m} + V_{latt.}(\mathbf{r}) \right) w(\mathbf{r} - \mathbf{r}_j) \quad (1.8)$$

and

$$V_{i,j,k,l} = \int \int d\mathbf{r} d\mathbf{r}' w^*(\mathbf{r} - \mathbf{r}_i) w^*(\mathbf{r}' - \mathbf{r}_j) (V_{int}(\mathbf{r}, \mathbf{r}')) w(\mathbf{r}' - \mathbf{r}_l) w(\mathbf{r} - \mathbf{r}_k). \quad (1.9)$$

We restrict ourselves to the lowest Bloch bands however we allow for long-ranged interaction terms. From the above equation we are able to derive every parameter that we will take under consideration and that will appear in the extended Bose-Hubbard model that we are building. This term will give us everything, from the on-site repulsion to multi-site terms such as: dipole-dipole interactions, density dependent hopping, and pair hopping. By carefully choosing our indices all of the previously mentioned parameters can be calculated. They are described by a combination of dipolar and  $\delta$ -like contact interactions

$$V_{int}(\mathbf{r}, \mathbf{r}') = g \delta^{(3)}(\mathbf{r}) + \gamma \left( \frac{(\mathbf{e}_1 \cdot \mathbf{e}_2) r^2 - 3(\mathbf{e}_1 \cdot \mathbf{r})(\mathbf{e}_2 \cdot \mathbf{r})}{|\mathbf{r} - \mathbf{r}'|^5} \right), \quad (1.10)$$

where  $g$  is the strength of the contact interaction and  $\gamma$  is the strength of the dipolar term. It is important now to take a look at these parameters individually.

First we set all the indices equal to each other,  $i = j = k = l$ , and from this we get our on-site interaction. This term is the contact term from above, Eq. (1.10).

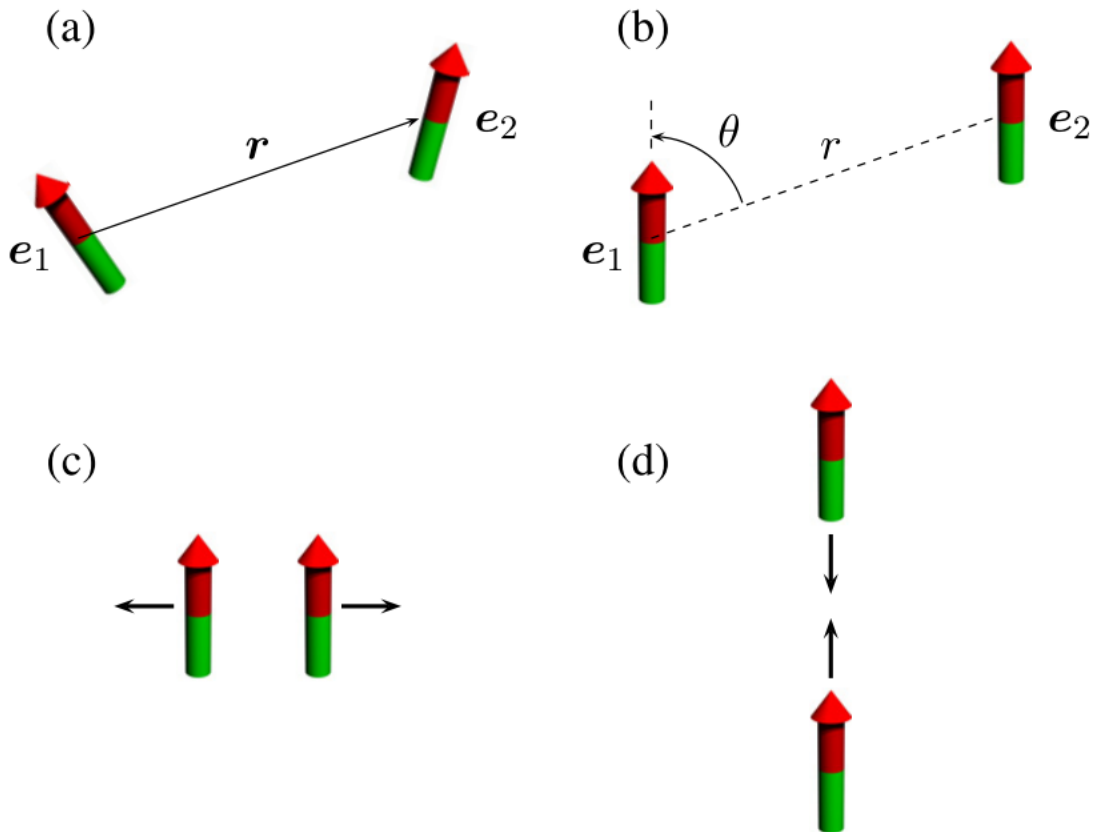


FIGURE 1.2: Here we show 4 different configurations of two dipolar particles. The top left panel, (a), shows two dipoles interacting with no polarization. The top right panel, (b), shows the behavior when the dipoles are polarized. The bottom two panels show two specific cases: (c) shows that dipole will repel each other when they are placed side-by-side and (d) shows that the dipoles will attract each other when placed head-to-tail. This diagram is taken from [11].

We can approximate the potential as

$$U = g\delta^{(3)}(\mathbf{r}) = \frac{4\pi\hbar^2 a}{m}\delta(\mathbf{r}) \quad (1.11)$$

where  $a$  is the  $s$ -wave scattering length and  $m$  is the mass of the particle. We can plug this back into Eq. (1.7) and get the single site interaction,

$$\frac{U}{2}(b_i^\dagger b_i^\dagger b_i b_i) = \frac{U}{2}(n_i(n_i - 1)) \quad (1.12)$$

where the factor of 2 comes from double counting.

Next if we let  $i = k$  and  $j = l$  we can get the dipolar term from the above potential (1.9). Let's define this term as

$$V_{ij} = \int \int d\mathbf{r} d\mathbf{r}' w^*(\mathbf{r} - \mathbf{r}_i) w^*(\mathbf{r}' - \mathbf{r}_j) (V_{dd}) w(\mathbf{r}' - \mathbf{r}_j) w(\mathbf{r} - \mathbf{r}_i), \quad (1.13)$$

where  $V_{dd}$  is the interaction created between two dipoles and is just the second part of Eq. (1.10).

The behavior of the dipolar interaction can be explained by looking at two particles, 1 and 2, with dipole moments along the unit vectors  $\mathbf{e}_1$  and  $\mathbf{e}_2$ , and whose relative position is  $\mathbf{r}$ . Now the energy due to the dipole-dipole interaction can be written as

$$V_{dd}(\mathbf{r}) = \gamma \left( \frac{(\mathbf{e}_1 \cdot \mathbf{e}_2)r^2 - 3(\mathbf{e}_1 \cdot \mathbf{r})(\mathbf{e}_2 \cdot \mathbf{r})}{|\mathbf{r} - \mathbf{r}'|^5} \right), \quad (1.14)$$

where  $\gamma = \frac{\mu_0 \mu^2}{4\pi}$ . This coefficient contains  $\mu_0$  which is the permeability of free space and  $\mu$  which is the permanent magnetic dipole moment (see Fig. 1.2 (a)). This formula is true only for particles that have a magnetic behavior however for particles that have an electric behavior the coefficient out front would be  $d^2/4\pi\epsilon_0$  where  $d$  is the electric dipole moment and  $\epsilon_0$  is the permittivity of free space. In this thesis we will keep our focus solely on magnetic interactions. Also we will be focusing only on systems where all the particles will be polarized in a specific direction, and so the above equation can be simplified to

$$V_{dd}(\mathbf{r}) = \frac{\mu_0 \mu^2}{4\pi} \frac{1 - 3\cos^2\theta}{|\mathbf{r} - \mathbf{r}'|^3}. \quad (1.15)$$

Here the angle  $\theta$  is calculated between the axis of polarization and the vector connecting the two dipoles. This vector is given by  $\mathbf{r} - \mathbf{r}'$  where the dipoles are positioned at  $\mathbf{r}$  and  $\mathbf{r}'$ , as is shown in Fig. 1.2 (b). From this equation we can see that the dipole-dipole interactions are anisotropic. This means that a couple of dipoles arranged side-by-side will be repulsive, Fig. 1.2 (c), while two dipoles placed head-to-tail will be attractive, Fig. 1.2 (d). There is also a magic angle such that when  $\cos^2\theta = 1/3$  the dipole-dipole interaction is completely canceled.

The true dipole-dipole interaction consists of both inter-site as well as on-site terms. For simplicity we will assume that the on-site part of the dipole-dipole interactions where  $i = j$ , is incorporated into the already defined on-site term,  $U$ . For the interactions between separate sites where  $i \neq j$ , we assume that the lattice is deep enough that we can measure the distances and angles from the center of each of the sites. This way we are able to take them out of the integral. We define  $a$  as the distance between nearest neighbor sites. So if  $a = |\mathbf{R}_i - \mathbf{R}_{i+1}|$ , then we can construct dimensionless positions of sites along the ring such that  $\tilde{\mathbf{R}}_i = \mathbf{R}_i/a$  and so, the dipole-dipole equation simplifies to

$$V_{ij} = V \frac{1 - 3 \cos^2 \theta_{ij}}{|\tilde{\mathbf{R}}_i - \tilde{\mathbf{R}}_j|^3} \quad (1.16)$$

where  $V$  is the value of the dipole-dipole interaction and  $\theta_{ij}$  is the angle between the orientation of the dipoles and the vector connecting them at sites  $i$  and  $j$ . Now we plug the above equation and the proper indices into (1.7) to get,

$$V_{ij}(b_i^\dagger b_j^\dagger b_i b_j) = V_{ij}(n_i n_j). \quad (1.17)$$

The final two parameters that will appear in the Hamiltonian are derived similarly to the dipolar term. We have the density dependent hopping which shows up when any three of the indices of Eq. (1.9) are equal. For example we set  $j = k = l$  and this will give us,

$$T_{ij} = \int \int d\mathbf{r} d\mathbf{r}' w^*(\mathbf{r} - \mathbf{r}_i) w^*(\mathbf{r}' - \mathbf{r}_j) (V_{dd}) w(\mathbf{r}' - \mathbf{r}_j) w(\mathbf{r} - \mathbf{r}_j). \quad (1.18)$$

which in turn gives,

$$T_{ij}(b_i^\dagger b_j^\dagger b_j b_j) = T_{ij}(b_i^\dagger n_j b_j) \quad (1.19)$$

from Eq. (1.7). This parameter causes a nearest neighbor hopping induced by the on-site interaction. In other words we have an additional term that causes a particle to tunnel only if an adjacent site is filled with more than one boson.

The final parameter arises when the creation operators have the one index and the annihilation operators have a different one.

$$P_{ij} = \int \int d\mathbf{r}d\mathbf{r}' w^*(\mathbf{r} - \mathbf{r}_i)w^*(\mathbf{r}' - \mathbf{r}_i)(V_{dd})w(\mathbf{r}' - \mathbf{r}_j)w(\mathbf{r} - \mathbf{r}_j). \quad (1.20)$$

The term in the Hamiltonian then takes the form,

$$P_{ij}(b_i^\dagger b_i^\dagger b_j b_j). \quad (1.21)$$

Now by combining all of these terms together we are able to write out the final form of an extended Bose-Hubbard model.

$$\begin{aligned} H = & -J \sum_{\langle i,j \rangle} (b_i^\dagger b_j + \text{h.c.}) + \frac{U}{2} \sum_i n_i(n_i - 1) - \mu \sum_i n_i + \sum_{i,j} V_{i,j} n_i n_j \\ & - \sum_{i,j} T_{i,j} (b_i^\dagger (n_i + n_j) b_j + \text{h.c.}) + \sum_{i,j} P_{i,j} (b_i^\dagger b_i^\dagger b_j b_j + \text{h.c.}), \end{aligned} \quad (1.22)$$

where all previously discussed terms now appear. The first three terms form the standard Bose-Hubbard model:  $J$  represents the tunneling term,  $U$  is the on-site interaction, and  $\mu$  is the chemical potential. The last three, more exotic terms make this an extended Bose-Hubbard model:  $V$  is the density-density interaction,  $T$  gives the density dependent tunneling, and  $P$  is the pair hopping. Most of these parameters will be kept to nearest neighbor interactions only (or not present at all) but for generality the coefficients are kept within the summations to allow for the possibility of long-ranged interactions.

The parameters can be modified using a multitude of different techniques. For example, the on-site repulsion can be manipulated by a process called Feshbach resonance [12, 13] which utilizes external magnetic fields in order to change the magnitude (and even sign) of the scattering length  $a$  that appears in 1.11. The hopping term is controlled by the shaking of the lattice. This process, like the Feshbach resonance for the on-site interactions, has the ability to scale and change the sign of the tunneling term [14–16]. The chemical potential shows the amount of energy needed in order to add another particle to the system. This is obviously

can be controlled if we restrict ourselves to a specific amount of particles.

Finally the dipolar interactions are mostly controlled by the choice of atoms that will populate the lattice. If we are interested in systems where the dipolar interactions are large we choose an atom with a high dipole moment. For example,  $^{52}\text{Cr}$  is a popular choice because it has a magnetic moment of  $6\mu_B$  where  $\mu_B$  is a Bohr magneton. However these interactions can also be scaled by the lattice depth. Just by increasing or decreasing the depth of the potential wells one can adjust the strength and range of the dipolar interactions [17]. In this way the final three parameters (which all come from the same source) can be manipulated.

### 1.3 Trapped ions

As we know many quantum systems are very difficult (if not impossible) to study due to the size and complexity of the interactions. We know, for example, that to fully describe a system of  $n$  spin-1/2 particles we need a Hilbert space of  $2^n$ . This number gets very large very quickly and therefore we are left with only the ability to study very small systems or we are forced to make approximations in order to calculate any observables. That is why we turn our attention to the concept of using trapped ions as the elements for quantum computing. This concept was first realized by Ignacio Cirac and Peter Zoller in 1995 [18]. The publication explains that ions are good candidates for quantum computing because they exhibit several attractive features. First of all it is possible to create  $n$ -bit quantum gates between any set of ions not only the nearest neighbors. Second, the decoherence times of ions is extremely (over 10 minutes) so there is plenty of time to complete calculations. Finally the readout or measurement can be performed with near 100% efficiency.

An extension of the previous work was done by Porras and Cirac when in 2004 they first proposed that trapped ions can be used as analogue quantum simulators for magnetic systems [19]. This idea was not based on quantum gates and so the requirements for its implementation were much less strict than for quantum

computers. Next we describe we can create a qubit and then how we can use it to simulate a spin system. First the ions can be held in a linear Paul trap, in microtraps in one or two dimensions, or in a Penning trap which can then be manipulated using either microwaves or photons. The basic idea is to use the internal hyperfine states of an atom like a two-state system. These two states would essentially create a qubit that would behave just like a spin-1/2 particle. The actual process utilizes a Raman transition controlled by two laser beams to "flip" the qubit. The first beam excites the atom from one hyperfine state into a virtual state while the second beam deexcites the atom into the second hyperfine state. The process is shown in Fig. 1.3.

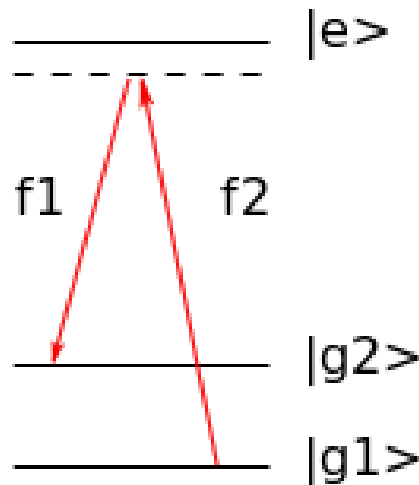


FIGURE 1.3: The process of generating a qubit using the hyperfine states of an atom. First a frequency  $f_2$  is used to create a virtual excitation from the original hyperfine state  $|g_1\rangle$ . Then a second frequency  $f_1$  is used to deexcite the atom into the other hyperfine state  $|g_2\rangle$ . The difference between the frequencies is exactly the energy difference between  $|g_1\rangle$  and  $|g_2\rangle$ .

In order to connect this to our work with dipolar interactions we can look at the typical spin Hamiltonian that the ions are actually simulating [19]

$$\begin{aligned}
 H &= \frac{1}{2} \sum_{i,j} J_{i,j}^z S_i^z S_j^z - \frac{1}{2} \sum_{i,j} J_{i,j}^x S_i^x S_j^x - \frac{1}{2} \sum_{i,j} J_{i,j}^y S_i^y S_j^y \\
 &- \sum_i (H_i^x S_i^x + H_i^y S_i^y + H_i^z S_i^z), \tag{1.23}
 \end{aligned}$$

where the interactions, which are mediated by phonons, have a long-ranged property to them. The fascinating thing about this long-ranged behavior is that it decays as one over the distance cubed,  $1/r^3$ , or just like a dipole-dipole interaction. In this Hamiltonian the phonons can control the overall sign and magnitude of  $J_{ij}^{x,y,z}$  and the spatial dependence is  $J_{ij}^{x,y,z} \propto 1/|r_i - r_j|^3$ . When  $J^x = J^y$  the behavior of this Hamiltonian closely resembles a hard-core Bose gas with dipole-dipole interactions acted upon by transverse and longitudinal magnetic fields. The big difference is that the tunneling term now also has a non-local behavior, and therefore also decays as  $1/r^3$  [20].

## 1.4 Methods

There are a multitude of ways to analyze any of the systems that we have discussed. Each method has its own set of pluses and minuses. It is important to try to choose the proper method for the proper problem. In this thesis we focus our attention on to specific methods. The first one that we employ is exact diagonalization. This technique is elegant in its simplicity and its exactness. The process uses no approximations and therefore always gives the most precise answers. Its limitations lie in its scalability. Because its behavior mirrors the behavior of the interactions, the Hilbert space grows exponentially with the size of the given system. However it is still an excellent method for studying small systems and we will utilize it in the next chapter to study a small one dimensional system of bosons. The other method that we will focus on will be quantum Monte Carlo (QMC) simulations. More specifically, we will use the open source QMC code of the ALPS project [21]. This technique will be used in Chapters 2 and 3 for studying larger two dimensional systems. The ability to study larger systems is one of the benefits of using the QMC code, but this method is not without its own limitations. As we will see, there will arise problems when we study systems with high frustration or with the sign problem. Sometimes these difficulties can be surpassed by certain means and other times they are just too troublesome to be able to find a solution to them. We will further address these issues as they come up in the later chapters.

## 1.5 Thesis outline

We have discussed several possibilities of what can be used as potential elements for creating quantum computers. Each of the models have the capability of having long-ranged dipolar interactions. Then we looked at multiple methods that can be used in studying those systems. Now let us present the structure of this thesis. Chapter 2 describes a very simple system of soft-core dipolar bosons on an optical lattice ring. The key element of this chapter will be to study the long-ranged behavior of the dipoles on a true ring topology and to examine the behavior of different polarizations. First we will look at dipoles that are polarized perpendicular to the plane of the ring (purely repulsive) and later we will study dipoles polarized parallel to the plane of the ring (anisotropic interactions). Using exact diagonalization we calculate the behavior of the system and see where the ground states crossover from one phase to another. In Chapter 3, we will look at trapped ions on a two dimensional triangular lattice and study the effects of these frustrated systems. Again we will be studying the long ranged nature of the dipolar interactions. In this chapter the hopping term will also decay like the dipolar interaction so we have a chance to study the long-ranged effect of both the dipoles as well as the tunneling. We will do this by using QMC simulations and will run into difficulties from several sources. The first will arise from the frustration effects that exist in this geometry and that are only made worse by the long-ranged nature of the system. The other will be the famous sign problem that will appear when the tunneling parameter becomes negative. Then Chapter 4, we continue to use QMC methods to examine a two dimensional system. This time however, will look at a square lattice filled with soft-core bosons. The unique characteristic of this chapter will be that the Hamiltonian will not only contain the dipole-dipole term but will also have a density dependent hopping parameter. This additional hopping term can be of like or opposite sign with the regular hopping which will influence the behavior of the entire phase diagram. In Chapter 5 we will discuss the influence that LR interactions have on systems in general. How they can enrich a phase diagram and also make calculations harder. Finally we will look at

---

experimental possibilities and what the future hold for LR dipolar interactions.

# Chapter 2

## Dipolar bosons on an optical lattice ring

### 2.1 Introduction

In this chapter we take a look at a small optical lattice ring filled with soft-core bosons with long-ranged dipolar interactions. Since we will be using exact diagonalization routines we will restrict ourselves to a small system of 8 bosons sitting on 8 sites (i.e. with unit mean density). We then study the behavior of the system for two separate cases. The first is when all the dipoles are polarized perpendicular to the plane of the ring and the second case is when the dipoles are polarized within the plane of the ring. The two situations lead to very interesting and qualitatively different behaviors. We analyze each one thoroughly and compare the results.

To begin let us consider the following one-dimensional Hamiltonian

$$H = \sum_i \left[ -J(b_i^\dagger b_{i+1} + \text{h.c.}) + \frac{U}{2} n_i (n_i - 1) \right] + \sum_{ij} V_{ij} n_i n_j. \quad (2.1)$$

This is a simplified version of the extended Bose-Hubbard model (EBHM) which was introduced in the first chapter, Eq. (4.1). Here the density dependent and

pair hopping terms are ignored. Also there is no chemical potential since we will be looking at systems where the number of particles is fixed. As we recall  $b_i^\dagger$  and  $b_i$  are the creation and annihilation operators respectively and  $n_i = b_i^\dagger b_i$  is the corresponding number operator. The coefficients represent the hopping parameter  $J$  and on-site repulsion  $U$ , while the final term,  $V_{ij}$ , gives the value of the dipolar interactions between all sites. It is at this point where the ring topology becomes important. If we were to consider this to be a one dimensional chain with periodic boundary conditions then all the interactions would be repulsive (or attractive). Quite impressive work has already been performed on polarized dipolar gases in one dimensional lattice systems [22–27]. However this study differs from the others because we consider an actual ring. This geometry allows the anisotropic nature of the dipole-dipole interactions to become evident. Also, most previous works stop at nearest neighbor or next-nearest neighbor interactions but here we look at interactions between every single possible pair of sites.

## 2.2 Exact diagonalization

We will study the problem using a technique called exact diagonalization. This method takes the extended Bose-Hubbard Hamiltonian and represents it as a matrix. This extremely sparse matrix is then diagonalized using the ARPACK package available for FORTRAN [28]. This package uses an iterative process called the Lanczos algorithm in order to find extremal eigenvalues [29]. We will use these tools to find several of the lowest lying eigenvalues and eigenvectors which will in turn be used to calculate some useful observables. The results of this method give precise (i.e. machine precision) answers for the eigenvalues and eigenvectors in a reasonable amount of time, unfortunately it is still extremely limited for large systems. The dimensionality of the Hilbert space is given by

$$D = \frac{(N + M - 1)!}{N!(M - 1)!}, \quad (2.2)$$

where  $N$  is the number of bosons and  $M$  is the number of sites. For our 8 site ring with 8 bosons the Hilbert space is  $D = 64,523$ . To get a good sense of how quickly this figure grows we look at a few more examples. For fixed filling  $N/M = 1$ , we get  $D = 6,435$  when  $M = 8$ ,  $D = 92,378$  when  $M = 10$ , and finally  $D = 1,352,078$  when  $M = 12$ . Now we take a more in-depth analysis into the workings of exact diagonalization.

As was mentioned earlier we only need the first few lowest eigenvalues and eigenvectors in order to fully understand the behavior of the system. Therefore we use the Lanczos methods to significantly reduce the time needed for performing the calculations. In order to solve the full matrix (i.e. get all eigenvalues and eigenvectors), the computational time required would be on the order of  $O(D^3)$  while the space needed to store the entire matrix would take up  $O(D^2)$  space. By using the Lanczos method we are able to get the same machine precision convergence much faster. Without going into any details, this method allows us to find extremal eigenvalues and their corresponding eigenvectors using an iterative process that reduces the computation time by a significant amount [29].

The solutions of this algorithm give eigenvalues  $E^{(\nu)}$  and eigenvectors  $C^{(\nu)}$  where each  $\nu$  corresponds to a specific energy level of the system. The ground state can be written as a superposition of all the Fock states with different weights given by elements of  $C^{(\nu)}$ . In the number basis we can write this as

$$|\Psi_\nu\rangle = \sum_{\alpha=1}^D C_\alpha^\nu |n_1, \dots, n_M\rangle_\alpha. \quad (2.3)$$

Now there are a few tricks that can be utilized in order to make the program more efficient. First of all we need to identify all of our basis vectors. Since we are working in the occupation number representation  $\{|n_1, n_2, \dots, n_M\rangle\}$  with a fixed number of particles  $\sum_{i=1}^M n_i = N$ , we need to have an effective way of calculating every Fock state that makes up the basis. In the occupation number basis we of course have

$$\hat{n}_i |n_1, n_2, \dots, n_M\rangle = n_i |n_1, n_2, \dots, n_M\rangle \quad (2.4)$$

where  $n_i \geq 0$ . We use a combinatorial algorithm that efficiently enumerates all the possible states.

Another trick that is used in order to reduce computation time is a technique called tagging. The process of creating tags for all the basis vectors of the Hamiltonian matrix will greatly reduce the space and time needed for evaluating our lowest energies. Let's take the Hamiltonian matrix

$$H_{uv} = \langle u | H | v \rangle \quad (2.5)$$

where  $u$  and  $v$  are all the basis vectors. Typically the entire basis vector would be stored in a matrix,  $A = D \times M$ , where the  $v^{\text{th}}$  row would correspond to the  $v^{\text{th}}$  vector. So we could define each vector as,

$$|v\rangle \equiv |A_{v_1}, A_{v_2}, \dots, A_{v_M}\rangle. \quad (2.6)$$

From this matrix let us pick out an arbitrary basis vector  $|v\rangle$  which is just one of the  $D$  possible Fock states and change it into a unique number. This unique number will be referred to as the tag of the vector and will be defined as,

$$T(v) = T(A_{v_1}, A_{v_2}, \dots, A_{v_M}). \quad (2.7)$$

This is accomplished by letting  $T(v) = \sum_{i=1}^M \sqrt{p_i A_{v_i}}$  where  $p_i = 100 * i + 3$ . This process guarantee that none of the tags will repeat.

Now in order to be able to find any arbitrary vector in our new list of tags it would take an average of  $D/2$  tries. To make this more efficient let's sort them in an ascending or descending order. Once the tags are all sorted we we can use Newton's binary method in order to locate the proper tag that we are looking for. This now reduces the search time from  $D/2$  to  $\log_2 D$ . Just to give an idea of how much better this method is let's compare how many tries it would take to find the right tag for our small system of 8 sites with 8 bosons. We will recall that the Hilbert space has the dimensions of  $D = 65,482$  so using the standard method of

just scanning down the unsorted list will require an average of 32,471 tries while the binary method takes only about 16 tries.

Still the most effective way that we can reduce the Hilbert space and make the computations even faster is by considering the symmetries found in the Bose-Hubbard model.

### 2.3 Symmetries of the EBHM

The first symmetry that we will look at has to do with the fact that our Hamiltonian has a conserved number of particles, in other words,  $\sum_{j=1}^M n_j = N$ . Due to  $U(1)$  symmetry we can show that the Hamiltonian is invariant under the transformation  $(b_i^\dagger, b_i) \rightarrow (b_i^\dagger e^{i\theta}, b_i e^{-i\theta}) = e^{iN\theta} (b_i^\dagger, b_i) e^{-iN\theta}$  for  $\forall \theta \in \mathbb{R}$ .

The next symmetry that exists in the Bose-Hubbard model is one that is invariant under the transformation  $(b_i^\dagger, b_i) \rightarrow (b_{i+1}^\dagger, b_{i+1})$  and only works if the Hamiltonian is assumed to have periodic boundary conditions. This is referred to as translational symmetry. This symmetry will exist for cases where the dipoles are polarized out of the plane of the ring however it is broken when the polarization is oriented along the plane of the ring due to the anisotropic nature of the interactions. When this is true we can no longer assume that each site exhibits the same behavior.

Next we have reflection symmetry. For this we can show that the Hamiltonian will be invariant under the transformation  $(b_i^\dagger, b_i) \rightarrow (b_{M+1-i}^\dagger, b_{M+1-i})$ . What this states is that if we split the ring into two halves then each half will behave the same. This symmetry remains unbroken for either of the polarization directions (however for systems with the polarization lying within the plane, the ring must be properly divided along the direction of polarization).

If we were to combine the last two symmetries we could show that the Bose-Hubbard model has a  $D_M$  symmetry. This symmetry is the symmetry of an equilateral polygon with  $M$  vertices. Combining the  $U(1)$  symmetry with the

$D_M$  symmetry, provides us with a block diagonal representation of our original Hamiltonian that greatly reduces the Hilbert space and computation time.

In this study we will only take advantage of the reflection symmetry. We start by splitting the ring into two halves (right and left) and defining operators in a new basis.

$$b_p^\dagger = \frac{b_R^\dagger + b_L^\dagger}{\sqrt{2}} \quad b_p = \frac{b_R + b_L}{\sqrt{2}} \quad (2.8)$$

$$b_n^\dagger = \frac{b_R^\dagger - b_L^\dagger}{\sqrt{2}} \quad b_n = \frac{b_R - b_L}{\sqrt{2}} \quad (2.9)$$

where we have defined parity and non-parity operators in terms of creation and annihilation operators of particles on either side of the ring lattice. Now we can plug these new operators into our Hamiltonian (2.1) in order to symmetrize it. We will do this term by term. The first term is the hopping term:

$$H_J = -J \sum_{\langle i,j \rangle} (b_i^\dagger b_j + b_j^\dagger b_i) \quad (2.10)$$

$$\begin{aligned} H_J = & -J \sum_{\langle i,j \rangle} (b_{R_i}^\dagger b_{R_j} + b_{L_i}^\dagger b_{L_j} + b_{R_j}^\dagger b_{R_i} + b_{L_j}^\dagger b_{L_i}) \\ & -J \sum_{\langle i,j \rangle} (b_{R_i}^\dagger b_{L_j} + b_{L_j}^\dagger b_{R_i}) \end{aligned} \quad (2.11)$$

$$H_J = -J \sum_i (n_{p_i} - n_{n_i}) + \sum_{\langle i,j \rangle} [(b_{p_i}^\dagger b_{p_j} + \text{h.c.}) + (b_{n_i}^\dagger b_{n_j} + \text{h.c.})] \quad (2.12)$$

Next we have the on-site term:

$$H_U = \frac{U}{2} \sum_i n_i(n_i - 1) \quad (2.13)$$

$$H_U = \frac{U}{2} \sum_i (b_i^\dagger b_i^\dagger b_i b_i) \quad (2.14)$$

$$H_U = \frac{U}{4} \sum_i (b_{R_i}^\dagger b_{R_i}^\dagger b_{R_i} b_{R_i} + b_{L_i}^\dagger b_{L_i}^\dagger b_{L_i} b_{L_i}) \quad (2.15)$$

$$\begin{aligned} H_U &= \frac{U}{4} \sum_i [n_{p_i}(n_{p_i} - 1) + n_{n_i}(n_{n_i} - 1)] \\ &+ \frac{U}{4} \sum_i [4n_{p_i}n_{n_i} + (b_{p_i}^\dagger b_{n_i})^2 + (b_{n_i}^\dagger b_{p_i})^2] \end{aligned} \quad (2.16)$$

Finally we have the dipole-dipole term:

$$H_V = \sum_{i,j} V_{i,j} n_i n_j \quad (2.17)$$

$$H_V = \sum_{i,j} V_{i,j} [n_{R_i} n_{R_j} + n_{L_i} n_{L_j} + n_{R_i} n_{L_j}] \quad (2.18)$$

$$\begin{aligned} H_V &= \sum_i \frac{V_i}{4} [(n_{p_i}(n_{p_i} - 1) + n_{n_i}(n_{n_i} - 1) - (b_{p_i}^\dagger b_{n_i})^2 - (b_{n_i}^\dagger b_{p_i})^2)] \\ &+ \sum_{ij} [V_{ij}(n_{p_i} n_{p_j} + n_{n_i} n_{n_j} + n_{p_i} n_{n_j})] \text{ where } i \neq j \end{aligned} \quad (2.19)$$

It is interesting to notice that while the on-site interaction remains solely on the diagonal, the hopping and dipolar terms now have both a diagonal as well as an off-diagonal part. This new Hamiltonian is now in a block diagonal form where one block defines all the parity states and the other block gives the non-parity states. Each of the blocks can be diagonalized separately, greatly reducing computation time.

## 2.4 Observables

First let's consider the condensate fraction. This observable comes from the one-body density matrix (OBDM) which is defined by

$$\rho_{ij}^{(1)} = \langle \Psi_0 | b_j^\dagger b_i | \Psi_0 \rangle, \quad (2.20)$$

where  $|\Psi_0\rangle$  is the ground state eigenvector of the system. The eigenvectors of the new matrix are called natural orbits while the eigenvalues are the occupation numbers of these orbits,  $N_c$ . In other words  $N_c$  is just the number of condensed particles in the system. The largest eigenvalue of the OBDM divided by the total number of particles corresponds to the condensate fraction,  $f_c = N_c/N$ . So when any one of these natural orbits is macroscopically occupied this is evidence that a BEC is present. If we neglect the presence of the dipole term,  $V$ , and the interactions are low,  $U/J \approx 0$ , then all the particles are in the condensate. As the ratio increases such that  $U/J > 0$  (but still  $V = 0$ ), the condensate depletes monotonically. In the thermodynamic limit ( $M \rightarrow \infty$  and  $N/M = 1$ ), at a critical value of  $U/J \approx 4.65$  the condensate is completely depleted and  $f_c = 0$  [30]. Of course here we are working in a finite system and therefore this is not completely true for our case. For finite systems there exists a lower bound for the condensate fraction which is  $1/M$ . This limit comes from the normalization of the OBDM which states that  $\text{Tr} \rho_{ij}^{(1)} = N$  and so there must exist an eigenvalue such that

$$\lambda_1 \geq \left( \sum_k \lambda_k \right) / M = N/M. \quad (2.21)$$

From this we can clearly see that the condensate fraction,  $f_c$  can never drop below  $1/M$  and so we can never really fully state that a condensate does not exist. Another aspect to focus on is that the presence of a condensate relates to the existence of off-diagonal long-range order. What this implies is that when a condensate is present then the matrix elements of the OBDM that are far off the

diagonal remain non-zero or to put this another way

$$\rho \not\rightarrow 0 \text{ for } |i - j| \rightarrow \infty. \quad (2.22)$$

So far we have solely focused on the macroscopic filling of the first natural orbit. However if there are multiple natural orbits macroscopically occupied then there exists what is called a fragmented condensate. This phenomenon corresponds to the existence of several individual condensates in a single system. In our case this will occur when two condensates appear on either side of the ring but stay separated [31].

Now we look at the superfluid fraction from two different points of view. First we will define it by its macroscopic properties and later we will look at its microscopic properties. This observable in both cases is connected to the flow of the particles in the system. Macroscopically we can treat the system as if it were made up of two different fluids. The first fluid is a normal fluid that reacts to the friction from the walls of the system. The other is the superfluid which can be thought of as having zero viscosity and therefore flowing without friction. By rotating the ring, we can calculate how much of the total fluid gets dragged along with the movement of the walls and how much is unaffected. The velocity of the moving fluid, from the reference frame of the moving system, will be able to provide us with the superfluid density.

We can also take a look at the microscopic behavior of the superfluid fraction. We add a phase to the condensate wave function which is connected to a velocity field by

$$\vec{v}_s = \frac{\hbar}{m} \vec{\nabla} \Theta(\vec{x}). \quad (2.23)$$

where the velocity of the fluid is proportional to the gradient of the phase. It is important to remember that this velocity field is both irrotational ( $\vec{\nabla} \times \vec{v}_s = 0$ ) and non-dissipative [32]. We assume a linear phase variation, so for a system of length  $L$  and can rewrite Eq. (2.23) with a spatially varying phase,  $\Theta(\vec{x}) = \Theta x/L$ .

Plugging it in we get

$$v_s = \frac{\hbar\Theta}{mL}. \quad (2.24)$$

The portion of the fluid that flows with this velocity,  $\vec{v}_s$ , is considered the portion that is in a superfluid state. The presence of this flow increases the kinetic energy of the system. It is important that the phase gradient be kept small so that no excitations appear and cause particles to jump into higher energy levels. But if  $\Theta \ll \pi$  then no unwanted excitations should present themselves. In this study we will set  $\Theta = 0.1$ . Now the difference of the ground state energies of a moving and stationary system can be written as

$$E_\Theta - E_0 = \frac{1}{2}M_s v_s^2, \quad (2.25)$$

where  $E_0$  is the ground state energy of the regular system while  $E_\Theta$  is the ground state energy of the system with the additional phase twist. The velocity of the flow is given by  $v_s$ . Finally the mass,  $M_s$ , is the mass of the superfluid part of the system. This value can be rewritten as  $M_s = mNf_s$ , where the term  $f_s$  is called the superfluid fraction (or superfluid density). Now by rearranging the last equation we can solve for the superfluid fraction and get

$$f_s = \frac{2mL^2}{\hbar^2 N} \frac{E_\Theta - E_0}{\Theta^2} \quad \text{for } \Theta \ll \pi \quad (2.26)$$

Up until now we have been working completely in a continuous system but this study focuses on a discrete lattice, so in order to progress from one picture to the other we have to employ a few changes. First of all the length of the system,  $L$ , will now become just the number of sites in the system,  $M$ . Next we have to replace the coefficient  $\hbar^2/(2m)$  by the tunneling strength,  $J$ . Finally we arrive at the proper formula that we will use to calculate the superfluid fraction

$$f_s = \frac{M^2}{JN} \frac{E_\Theta - E_0}{\Theta^2} \quad \text{for } \Theta \ll \pi. \quad (2.27)$$

As mentioned earlier, the two different energies that are present in the above

formula correspond to the ground state energies of two different Hamiltonians.  $E_0$ , of course, comes from the regular Hamiltonian (2.1) that was introduced at the beginning of this chapter, while the other energy,  $E_\Theta$  is the ground state energy of a Hamiltonian with twisted boundary conditions. We can write it as

$$H = \sum_i \left[ -J(e^{-i\Theta/M} b_i^\dagger b_{i+1} + \text{h.c.}) + \frac{U}{2} n_i (n_i - 1) \right] + \sum_{ij} V_{ij} n_i n_j. \quad (2.28)$$

where we can see that the hopping term has now picked up an extra phase. These additional terms are commonly called the Peierls phase factors and they simulate a slow motion of the system. In this system that will directly correspond to a slow spinning of the ring. A final important point to make is that the superfluidity and condensation are not the same thing. The presence of a superfluid does not immediately guarantee the existence of a condensate.

Lastly we will look at the occupation variance of the system

$$\Delta = \sqrt{\langle n_i^2 \rangle - \langle n_i \rangle^2}. \quad (2.29)$$

It is useful to calculate this observable because it does not show any strong finite size effects. Even small systems like ours, where  $M = 8$ , behave like an infinite system. This observable will give the fluctuation around the mean occupation number in a site. This observable provides us with more information than the mean value can provide. While the mean value very often will remain unchanged the variance can differ. The mean value is given by

$$\bar{n}_i = \langle \Psi_0 | n_i | \Psi_0 \rangle, \quad (2.30)$$

and for translationally invariant lattices this value equals  $N/M$  for all sites and for all values of  $U$  and  $J$ . This value will fluctuate when the polarization of the dipoles is in the plane of the ring because the lattice is no longer translationally invariant but when the polarization is out of the plane of the ring this observable gives very little information about the system and therefore we have to focus more on the variance. When the ground state  $|\Psi_0\rangle$  is a pure state made up of just a

single Fock state than this value will be zero. On the other hand if the ground state has a superposition of many Fock states than our variance will be large. This will allow us to determine the behavior of the system as interactions change and help determine where the system crosses over from one ground state to another.

## 2.5 Results

Hamiltonian (2.1) depends on three parameters:  $J$  the hopping,  $U$  the on-site repulsion, and  $V$  the dipole-dipole interaction. We set  $J = 1$  and therefore we are able to express  $U$ ,  $V$  and  $H$  in units of the tunneling. This Hamiltonian will describe an 8 site ring with 8 soft-core bosons (i.e. unit mean density). Here the bosons are completely soft-core by which we mean that there will be no restriction on the amount of bosons allowed on a single site. Now we can study the behavior of all the observables and see what interesting ground states arise from the analysis of the model.

### 2.5.1 Polarized out of plane

The first case to consider is one where all the dipoles are polarized perpendicular to the plane of the ring. In this configuration the angle between any two given sites is always  $\theta_{ij} = \pi/2$  therefore Eq. (1.16) simplifies to  $V_{ij} = V \frac{1}{|r_i - r_j|^3}$ . This situation creates dipoles that are purely repulsive. Our case is unique to previous studies such as [23, 24] since we have an actual ring topology and not just a linear chain with periodic boundary conditions. The major difference is that distances on a ring need to be calculated properly between each set of sites. They are not all set apart by the lattice constant  $a$  as they would be in a one-dimensional chain with periodic boundary conditions. Also, as mentioned earlier,  $V_{ij}$  will be calculated for every single pair of sites on the ring and not just for nearest neighbors.

In Fig(2.1) we show the results of the superfluid fraction,  $f_s$ , the condensate fraction  $f_c$  and the variance  $\Delta$  as a ratio of  $V$  and  $U$ . Each one of the plots corresponds

to a different value of  $U$ . The top two panels, (a) and (b), show the behavior of the system for relatively low on-site interactions,  $U = 1$  and  $U = 4$  respectively. While panels (c) and (d) correspond to  $U = 7$  and  $U = 10$  respectively.

A quick analytical explanation can be presented for the behaviors of  $f_s$  and  $f_c$  at small  $V/U$  if we assume that our tunneling amplitude is very small,  $J \approx 0$ . If there is no hopping term and no dipole-dipole interaction than all the particles would arrange evenly across the lattice and our ground state would be a Mott insulator giving an energy  $E_0 = 0$ . The first excited state differs only slightly from the Mott state. In this state all but two sites are filled with a single boson while one is empty and another has two bosons in it. A quick calculation of this state gives  $E_1 = U$ . So we can immediately see that the energy gap is given by  $\Delta E = U$ . In

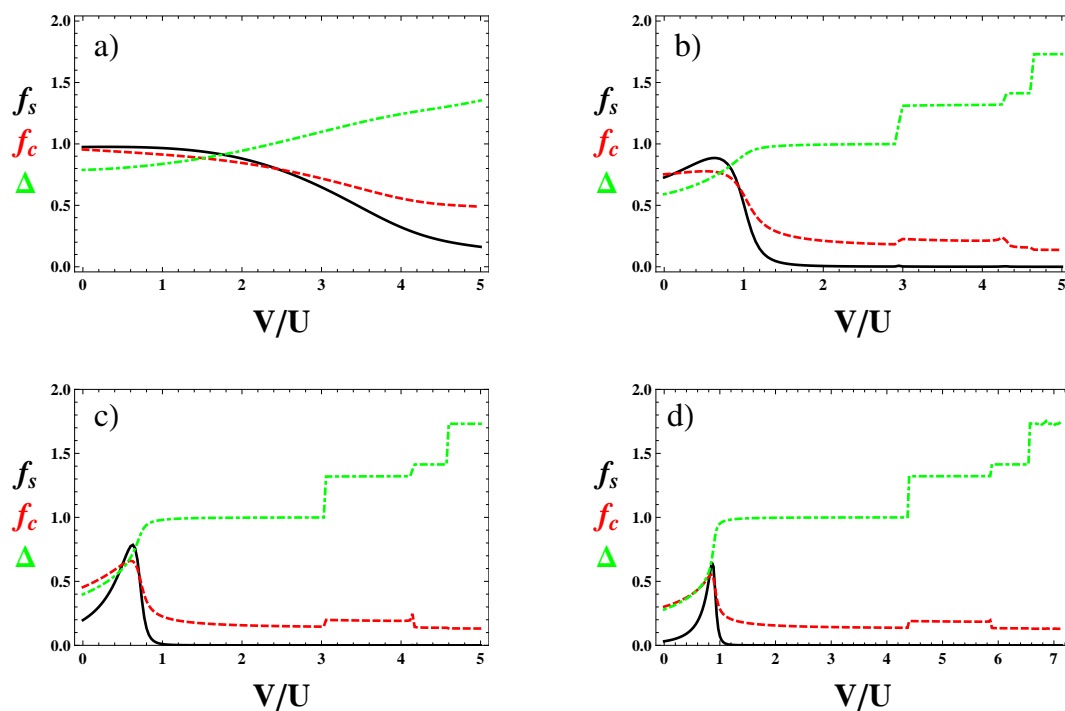


FIGURE 2.1: Superfluid fraction  $f_s$  (solid black lines), condensate fraction  $f_c$  (red dashed lines) and variance of occupation on different sites  $\Delta$  (green dot-dashed) as a function of  $V/U$  for  $U = 1, 4, 7, 10$  (panels (a) to (d), respectively). For small  $V/U$  we observe an increase of the superfluid (and condensate) fraction with  $V$  both in the SF phase (for  $U = 1$  panel (a) as well as for  $U = 10$  panel (d)) where the increase of  $V$  causes transition from MI to SF phase. Around  $V/U = 0.5$  a transition to a density wave state  $[2, 0]$  occurs, more sudden for larger  $U$ , as manifested by a rapid drop of  $f_s$  and  $f_c$ . For larger  $V/U$  sharp transitions between different density waves occur as manifested in  $f_c$  as well as in variance of occupation  $\Delta$ .

such a situation both the superfluid fraction and the condensate fraction would be equal to zero,  $f_s = f_c = 0$  and therefore the system would start off in a Mott insulating state. The fact that our results show none zero values has to do with the fact that we are working in a finite system and of course our hopping parameter is never zero. Now if we turn on a small dipole-dipole interaction but continue to disregard the tunneling the gap between the lowest states becomes  $\Delta E = U - V$ . From this we can see that as the ratio  $V/U$  increases slightly above zero than the energy gap between the first two states decreases and both the superfluid fraction and the condensate fraction should increase.

Let's take a look back at Fig. 2.1. In panel (a), we do not see any of the behavior that is described in the previous paragraph. Neither the superfluid fraction nor the condensate fraction increase as  $V/U$  gets larger, in fact they both decrease. For an infinite system without dipole-dipole interactions the ground state would be a superfluid which would give a maximum value for both the superfluid fraction as well as the condensate fraction. This is behavior can easily be explained by the fact that we are looking at a values of  $U$  and  $J$  that are equivalent to each other,  $U = J = 1$ . Therefore the assumption we made earlier does not apply. As  $V$  gets larger, it pushes all the particles apart so both the  $f_s$  and  $f_c$  decrease monotonically until, at high  $V$  values, the system settles into a Mott state. But this panel is unique in its behavior when compared to the others.

Now we increase the interaction to  $U/J = 4$  and we see a change in the behavior. Such a system would start slightly in the Mott regime for an infinite lattice at unitary filling and with no dipole-dipole interactions. This plot now is more closely related to the analytical explanation. Although  $f_s$  and  $f_c$  do not start at zero they do increase moderately for small  $V/U$  values before dropping down. For higher ratios of  $U/J$  this behavior is much more prominent as in panels (c) and (d) with a much sharper peaks for  $f_s$  and  $f_c$ . Another thing to notice is that the variance of the system is no longer a smoothly increasing function but rather has a step like behavior at higher  $V/U$  when the system crosses over to a density wave state.

Since all of these changes are more obvious in the bottom two panels of Fig. 2.1, let us focus on them. In both panels (c) and (d) the superfluid fraction as well as the condensate fraction begin at low values and at first increase as the dipole-dipole interactions get stronger, just as predicted by the analytical analysis for small  $V$  values. However, the figure clearly shows that these values are not completely zero. This is connected to the fact that we are working with a small system that experiences finite size effects. Now at  $V/U \approx 0.62$  for  $U/J = 7$  and  $V/U \approx 0.87$  for  $U/J = 10$  there is a sudden change and the observables quickly decrease. After this sudden drop the system changes to a density wave phase that is characterized by an alternation of empty sites and ones filled with 2 bosons. For simplicity we will refer to this as the  $[2, 0]$  state. At higher  $V/U$  ratios other such density wave phases appear with different occupation numbers on different sites. Each new density wave phase is characterized by a sharp hop in the variance, as can clearly be seen in panels (b)-(d) of Fig. 2.1. We can also observe that these changes between different density wave phases are quite independent of the parameter  $U$  since they show up in every plot except where the tunneling term is negligible and only the  $V/U$  parameter is relevant.

As was mentioned earlier, this system possesses certain symmetries. When the polarization is out of the plane of the ring then we know that system is invariant under a rotation by  $2\pi/M$  where  $M = 8$  is the number of sites in our lattice. Because of this the ground state will also possess a symmetry that will cause two near degenerate energy states to appear. There are two lowest lying states that are even and odd combinations of the  $[2, 0]$  and  $[0, 2]$  density wave phase that satisfy  $\langle n_i \rangle = 1$  at every site. In order to see which density wave configuration we have we will use the one body density matrix 2.20 and trace out all sites except one.

From the partial trace of the OBDM we get the probability distribution  $P(n)$  of the bosons at a single site. Table 2.1 shows this distribution for several different ratios of  $V/U$  and up to 4 bosons per site. Higher fillings per site have been omitted since their values are extremely small. The second column, where  $V/U = 2.5$ , corresponds to the density wave phase with  $[2, 0]$  modulation. We can clearly see this because the values corresponding to  $n = 0$  and  $n = 2$  have a probability

n	$V/U = 2.5$	$V/U = 3$	$V/U = 4.5$	$V/U = 5$
0	0.4950	0.6139	0.6225	0.7491
1	0.0124	0.0181	0.0057	$8.6 \cdot 10^{-4}$
2	0.4902	0.1229	0.2456	$3.6 \cdot 10^{-6}$
3	0.0024	0.2453	0.0018	$8.6 \cdot 10^{-4}$
4	$2.3 \cdot 10^{-6}$	0.0049	0.1244	0.2491

TABLE 2.1: Probability distributions at a given site for an 8 site lattice for different ratios of dipolar to on-site coupling,  $V/U$  for  $U = 4$  revealing different density wave arrangements.

distribution of approximately  $1/2$ . The rest of the  $n$  values are nearly zero but due to finite tunneling the occupation will never completely vanish. In the next column over, where  $V/U = 3$ , we see that the occupations of the different filling has changed. At this ratio we now have one site filled by 2 bosons, two sites filled with 3 bosons, and the rest remain unoccupied. If we look back at Fig. 2.1 we can see that in panel (b) there is a sharp jump just below  $V/U = 3$  in both the condensate fraction and the variance. (There is actually also a peak in the SF but it is quite small.) These jumps corresponds to the system transitioning from the  $[2, 0]$  density wave state to the one just described. The next ground state configuration has five empty sites, two sites filled with 2 bosons and one site with 4 bosons. This is verified by the fourth column of Table 2.1 and corresponds to the next jump in the occupation variance in Fig. 2.1 panel (b). There is also a decrease in  $f_c$  and again a small peak in  $f_s$  (which is too small to see without zooming in). The small peaks in the superfluid fraction can be explained by the fact that in order for the ground states to change for one density wave state to the next, the particles have to be able to rearrange. This quick movement from one ground state to the next causes a slight jump in the superfluid density to allow the bosons to change sites. In fact we can assume that there are peaks in  $f_s$  at each of the transition points but are too small to be noticed. Returning to the main topic, we see that another density wave state exists above  $V/U \approx 4.5$ . This state is again characterized by a clear jump in  $\Delta$  and a very small jump that decreases  $f_c$ . Now looking at the final column in Table 2.1 we observe that this density wave has two sites filled by 4 bosons while the rest remain empty. If continue to increase the ratio  $V/U$  eventually there will exist a state (not shown) that contains

all of the bosons in one site while 7 sites remain empty. This happens when the dipole-dipole interactions between sites becomes so strong (when compared to the on-site interaction) that it is energetically favorable to just place them all in a single site.

This behavior however is in contrast with the findings of S. Zöllner et. al. in [33]. In this chapter it is shown that a crystal like structure appears at high values of  $V$ . However there are a few differences that could explain this discrepancy. In our study we are working with optical lattices while in [33] there is a quasi-one-dimensional ring trap. A second difference is that, as we mentioned earlier, we have incorporated the on-site dipolar interaction right into our  $U$  parameter. This gives us the freedom to increase  $V$  until the parameter  $U$  is negligible and no extra energy is required to add bosons to the site. In [33] the contact term of  $V$  is always calculated and so as the inter-site repulsion increases so does the on-site repulsion and therefore can never truly be neglected. Finally the dipolar interactions do not extend out to all sites then it is impossible for all the particles to collect in one spot.

The types of density waves that are allowable for any system are dependent on the geometry of that system. This is especially pertinent since we are dealing with only 8 sites. Obviously as the system size increases these differences disappear. But since we are focusing on very small systems let's look at a 9 site ring again with unit filling. This geometry provides us with a completely different set of density waves than we had for the 8 site system. In this case we would start with one site filled with 3 bosons, three sites containing 2 bosons and the rest remaining empty. This crosses over to a density wave that has a modulation of  $[3, 0, 0]$ . As the  $V/U$  ratio increases the system jumps a state where one site has 4 bosons and another has 5. These results are all shown in Table 2.2 through the probability distributions on the given sites of this 9 site ring. A final phase, at very high  $V/U$  contains all the bosons in a single site similarly to the 8 site lattice.

A key point of these results is that such phases only appear due to the long-ranged nature of the dipole-dipole interactions. If we had limited the interaction to just

n	$V/U = 2.25$	$V/U = 7.75$	$V/U = 10$
0	0.5359	0.6661	0.7777
1	0.0368	$5.510^{-4}$	$1.3 \cdot 10^{-4}$
2	0.3186	$5.510^{-4}$	$9.2 \cdot 10^{-8}$
3	0.1085	0.3328	$7.4 \cdot 10^{-5}$
4	$9.5 \cdot 10^{-5}$	$6.710^{-8}$	0.1111
5	$6.2 \cdot 10^{-9}$	$1.610^{-15}$	0.1111

TABLE 2.2: Probability distributions at a given site of a 9 site lattice for different ratios of dipolar to on-site coupling,  $V/U$  for  $U = 4$  revealing different density wave arrangements.

nearest or next-nearest neighbors we would not be able to find this behavior. If, for example, we truncated the interactions to next nearest neighbors than no matter how high the dipole-dipole interaction would be it could never create a state where all particles would gather in a single site. As a final note we should observe that the crossovers between the different density waves resemble phase transitions of the first kind (both  $f_c$  and  $\Delta$  feature sharp jumps on the plots).

## 2.5.2 Polarized in plane

Now we change the axis of polarization, by making the magnetic field lie in the plane of the ring and we see how the behavior of the system differs. We can no longer use the simplified version of Eq. 1.16. Now we must take into account not only the distances between individual sites but also the different angles between them as well. In this scenario the anisotropic nature of the dipole-dipole interaction comes to light and provides a completely different picture than the one discussed previously. Again we will work with the 8 site ring containing 8 bosons. This very important because for the this finite system even the orientation in the plane will change the results of the ground states. Therefore we chose the most symmetric possibility where the polarization axis is parallel to the two sides of the octagon as shown in Fig. 2.2. This orientation will now require us to treat separate sites differently, but we are able to group them together. Due to some symmetry considerations, the lattice can now be broken down into two types of sites. The 4 sites located at the end of the edges that are parallel to the polarization axis

(points 2, 3, 6 and 7 in Fig. 2.2) will be referred to as type-I. The 4 sites located at the end of the edges that are perpendicular to the polarization axis (points 1, 4, 5 and 8 in Fig. 2.2) will be referred to as type-II. From Eq. 1.16 we see that the angle  $\theta_{ij}$  can make the dipole-dipole interactions either repulsive or attractive depending on the relative orientations of sites  $i$  and  $j$ . We will now show that the attractive interactions due to sites of type-I will be the dominating factor that decides the ground state configuration.

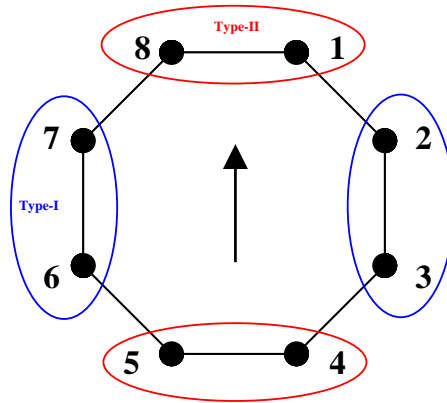


FIGURE 2.2: A ring shaped lattice, the arrow indicates polarization of dipoles. Due to symmetry sites 2,3,6,7 are equivalent (type-I), similarly 1,4,5,8 (type-II).

Fig. 2.3 gives the behavior of our different observables at sites of different types for a shallow lattice with  $U/J = 1$ . As we can see in panel (a) of Fig. 2.3 the superfluid fraction represented by the black line starts out at unity and drops down to zero where a clear transition can be seen at  $V/U \approx 0.5$ . We also see a decrease of the condensate fraction (or the first eigenvalue of the OBDM) while at the same time there is an increase of the second eigenvalue of the OBDM. As we have stated at the beginning of the chapter this can happen when we have a fragmented condensate [31]. What this means is that after  $V/U$  rises above 0.5 than all the particles in sites of type-II transfer into sites of type-I and so the system has now broken into two coherent halves each localized at a pair of neighboring sites of type-I. This is verified by the variance shown in panel (b) of Fig. 2.3. While the blue curve, which represents of the occupation number for sites of type- I ( $n_I$ ), steadily increases, the variance of the particle number for sites of

type-I ( $\Delta_I$ ) sharply increases around  $V/U = 0.5$ . So this again confirms that we have all of our bosons sitting in type-I sites. This superposition of “macroscopic” states can easily be compared to a double well system where an effective attractive interaction dominates, like in Ref. [34, 35].

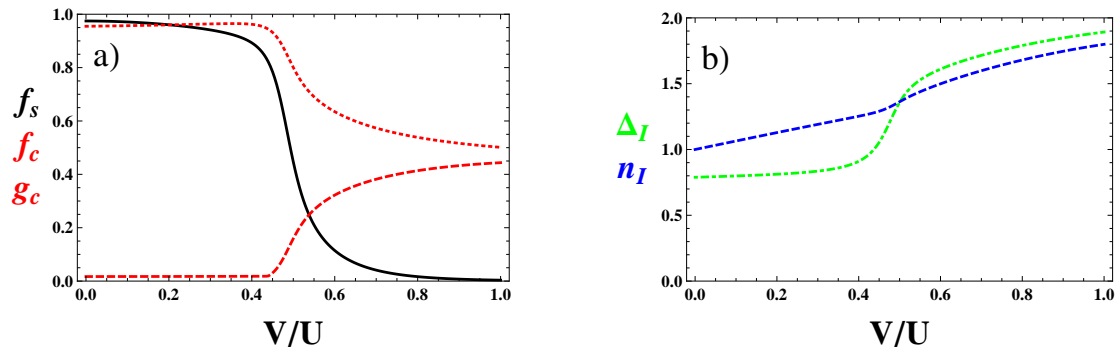


FIGURE 2.3: The graphs show results for a shallow lattice,  $U/J = 1$ . In panel (a) the solid black line shows a SF fraction with a drop around  $U/J = 0.5$ . This drop is accompanied by similarly rapid increase of the number variance  $\Delta_I$  (green dash-dotted line in panel (b)) as well as changes of condensate fraction,  $f_c$  (dashed red line) and the second eigenvalue of OBDM,  $g_c$  (dotted red line). On the other hand the mean occupation  $n_I$  of I-sites (blue dashed line in panel (b)) increases slowly and smoothly in the whole studied range of  $V/U$ . For the discussion see text.

A very similar study exists, Ref. [36] where instead of an optical lattice a toroidal trap is used to study the behavior of dipolar particles. In this paper a Gross-Pitaevski mean-field approach is used in order analyze the system. The study confirmed our results by showing that at higher values of the dipole-dipole interaction the condensate splits and all the bosons gather on each side of the torus. As the dipolar interactions continue to increase the a symmetry breaking phenomenon occurs that is typical of attractive nonlinear systems and all the particles group together on a single side of the toroidal trap. This symmetry breaking is the mean-field counterpart of the macroscopic superposition occurring at the quantum level. If now look at Table 2.3, we can confirm that the situation is identical in our system as well. In this Table we show the occupation probability distributions,  $P(n)$ , for each type of site at both below and above the transition point of  $V/U = 0.5$ . For type-II sites  $P(n)$  changes smoothly while type-I sites show a behavior that at  $V/U > 0.5$  the ground state becomes a superposition of a vacuum state with a state centered around large  $n$ . If we were to continue to

increase the dipole-dipole interaction, say  $V/U > 30$ , we would eventually arrive at a symmetry broken state that would just be a superposition of two Fock states,  $\frac{1}{\sqrt{2}}|0, 4, 4, 0, 0, 0, 0, 0\rangle + \frac{1}{\sqrt{2}}|0, 0, 0, 0, 0, 4, 4, 0\rangle$ , and whose condensate fraction is significantly less than  $1/2$ .

n	Type-I		Type-II	
	$V/U = 0.4$	$V/U = 0.6$	$V/U = 0.4$	$V/U = 0.6$
0	0.2098	0.4839	0.4146	0.6072
1	0.4260	0.0397	0.4391	0.2955
2	0.2771	0.1279	0.1313	0.0867
3	0.0766	0.2132	0.0144	0.0100
4	0.0099	0.1140	0.0006	0.0005

TABLE 2.3: Probability distributions at sites of type I and II on either side of the  $V/U = 0.5$  transition for  $U/J = 1$ , revealing ground state character change.

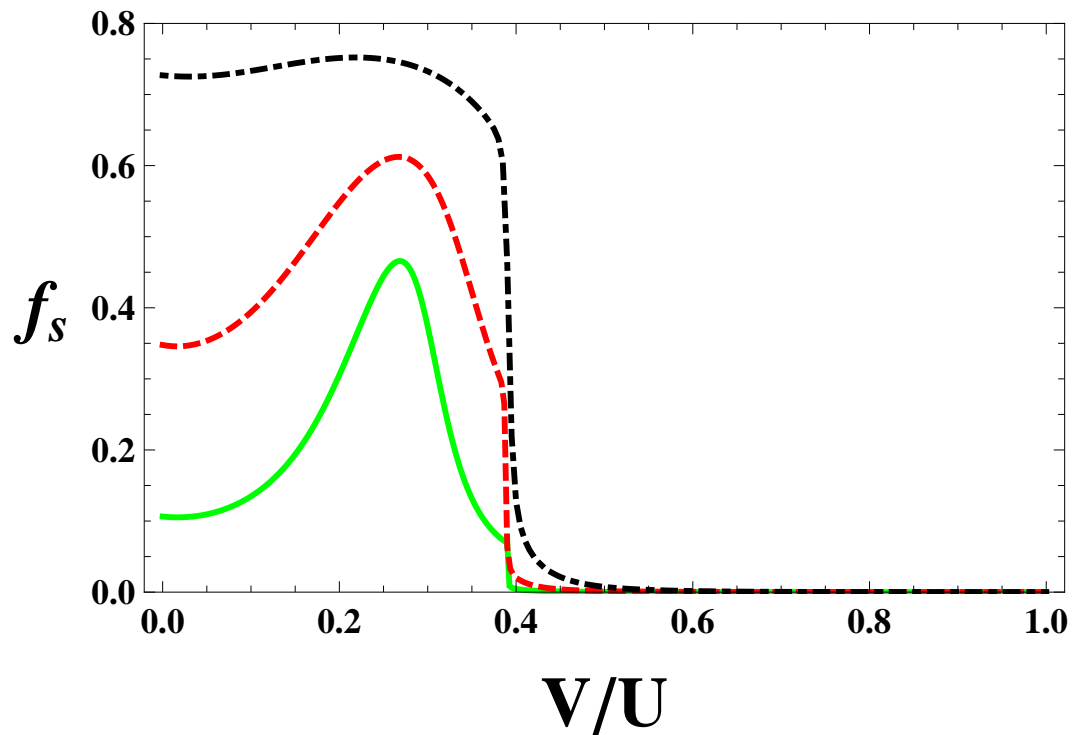


FIGURE 2.4: Intermediate  $U/J$  behavior. SF fraction is shown in for  $U/J = 4$  (black dotted line),  $U/J = 6$  (red dashed line) and  $U/J = 8$  (solid green line).

At greater values of the on-site repulsion the "double-well-like" behavior is even more prominent as can be seen in Fig. 2.4. The plot show values for  $U/J = 4$ ,  $U/J = 6$  and  $U/J = 8$  and it is very evident that there is a sharp transition at  $V/U \approx 0.4$  for all three parameters. This sudden drop in the superfluid fraction

corresponds to the separation of a single condensate into a fragmented condensate. So just like before a single coherent state breaks into a superposition of two coherent halves, and we get two separate condensates sitting at either end of the ring in the type-I sites. The sharpness of the crossover may be linked to an extremely narrow avoided level crossing involving the ground state of the system. Fig. 2.5 shows an example of such a situation. The plot gives the first 5 energy levels for  $U/J = 6$  with changing  $V/U$ . As we can see from the large graph in Fig. 2.5 it seems that 4 of the energy levels come very close together at the point of the crossover. The inset, which zooms in on the area where the avoided crossing occurs, definitively shows that although the energy levels come close together they never actually cross. As the ratio of  $U/J$  increases, this behavior becomes more prominent and the energy levels get increasingly nearer to each other.

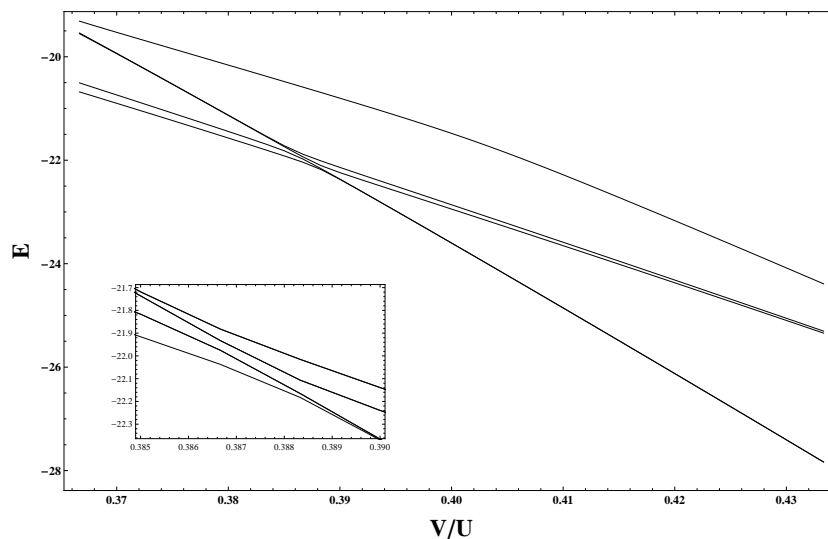


FIGURE 2.5: The first 5 energy levels for  $U/J = 6$  of an 8 site ring with 8 bosons that are polarized within the plane of the ring. We can see in the large graph that 4 of the energy levels are come very close together at the point of the crossover from one ground state to another. The inset zooms in on this avoided crossing in order to show that the energy levels really are separated and never really cross paths.

Continuing to focus on  $U/J = 6$  we can watch how it evolves with changing  $V/U$ . From the panel (a) of Fig. 2.6 we can clearly see the break of the condensate into two parts. We begin with the first eigenvalue of the OBDM ( $f_c$ ) having a macroscopic value with the second eigenvalue ( $g_c$ ) being close to zero. After the crossover both of the eigenvalues have macroscopic values. In fact it appears as

if the two eigenvalues become nearly degenerate,  $f_c \approx g_c$ , which is an outcome of the superposition of the two Fock states discussed earlier. A final confirmation of this action is seen in Fig. 2.6 (b). As the  $V/U$  increases, type-II sites gradually depopulate as type-I sites gradually fill. The transition is mostly smooth except for a small kink that appears at the crossover point for the occupation of type-I sites and a "reversed kink" (not shown) for the depopulation of type-II sites. This occurs when the bosons redistribute themselves in the lattice because of a competition between tunneling and interactions. Also in Fig. 2.6 panel (b) we can see the variance of occupation for type-I sites. The sharp drop in the superfluid fraction leads to a sharp rise in the variance of occupation.

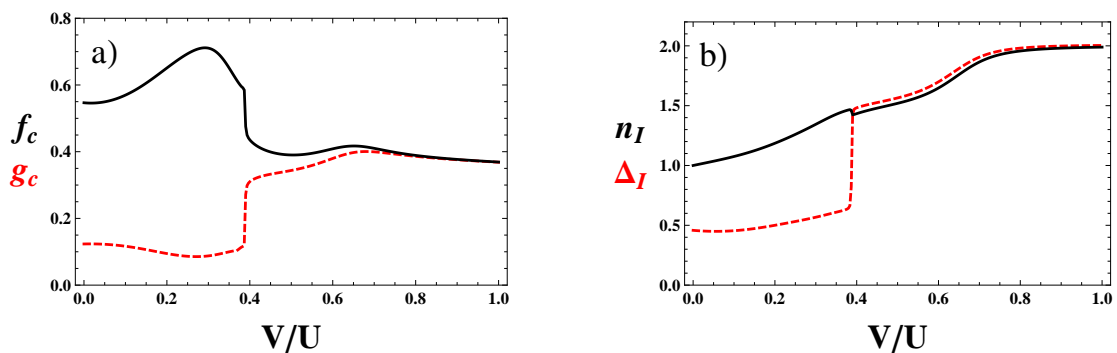


FIGURE 2.6: Panel (a) presents the mean occupation and the variance of type-I states for  $U/J = 6$  while panel (b) shows the  $V/U$  dependence (again for  $U/J = 6$ ) of the condensate fraction,  $f_c$ , i.e. the largest eigenvalue of the OBDM, and the second largest eigenvalue, denoted by  $g_c$ . The sudden drop of SF fraction occurring at  $V/U = 0.4$  in Fig. 2.4 is accompanied by a sharp increase of the occupation variance in type-I sites  $\Delta_I$  [red dashed line in (a)]. The occupation  $n_I$  (black line) shows there is a small kink too. At the same  $V/U = 0.4$  the sharp drop in  $f_c$  is observed, while  $g_c$  shows an increase.

If we were to continue to increase the the on-site repulsion an interesting phenomenon occurs. At high values of  $U/J$  the ground state of the system remains in an insulating state across the entire range of  $V/U$ . This means that the superfluid fraction is zero the entire time. However the states change from one insulating phase to another which is seen in Fig. 2.7. Also the kinks in  $\Delta_I$  decrease and finally disappear. Looking at Fig. 2.7 we graph  $n_I$  and  $\Delta_I$  for  $U/J = 10$  and  $U/J = 20$  we can see the step-like behavior of the variance of type-I sites accompanied by the smooth increase of the occupation of type-I sites. What this is showing is that in these parameters solely the on-site repulsion and the long-ranged dipole-dipole

terms compete against each other and the tunneling term is nearly negligible. The entire regime is essentially described by several Fock states. In the  $U/J = 20$  case, where these effects are more extreme, we can describe each plateau with a different superposition of Fock states. The first plateau shows the system in a Mott insulating state easily described by a single Fock state,  $|1, 1, 1, 1, 1, 1, 1, 1\rangle$ . The next plateau at around  $V/U = 0.3$  replaces the Mott state by a superposition of  $\frac{1}{\sqrt{2}}|0, 1, 1, 0, 1, 2, 2, 1\rangle + \frac{1}{\sqrt{2}}|1, 2, 2, 1, 0, 1, 1, 0\rangle$ . Next, around  $V/U = 0.4$  the state  $\frac{1}{\sqrt{2}}|0, 0, 0, 0, 1, 3, 3, 1\rangle + \frac{1}{\sqrt{2}}|1, 3, 3, 1, 0, 0, 0, 0\rangle$  takes over, which is finally replaced by  $\frac{1}{\sqrt{2}}|0, 0, 0, 0, 0, 4, 4, 0\rangle + \frac{1}{\sqrt{2}}|0, 4, 4, 0, 0, 0, 0, 0\rangle$  around  $V/U = 0.65$ . Just to be clear the behavior described here is not due to the long-ranged nature of the dipolar interactions but rather due to their anisotropic nature. The existence of the attractive interactions caused by the head-to-tail alignment in type-I sites causes the condensate to have the symmetry breaking behavior seen here. Had we truncated the dipole-dipole interaction this behavior would continue to exist.

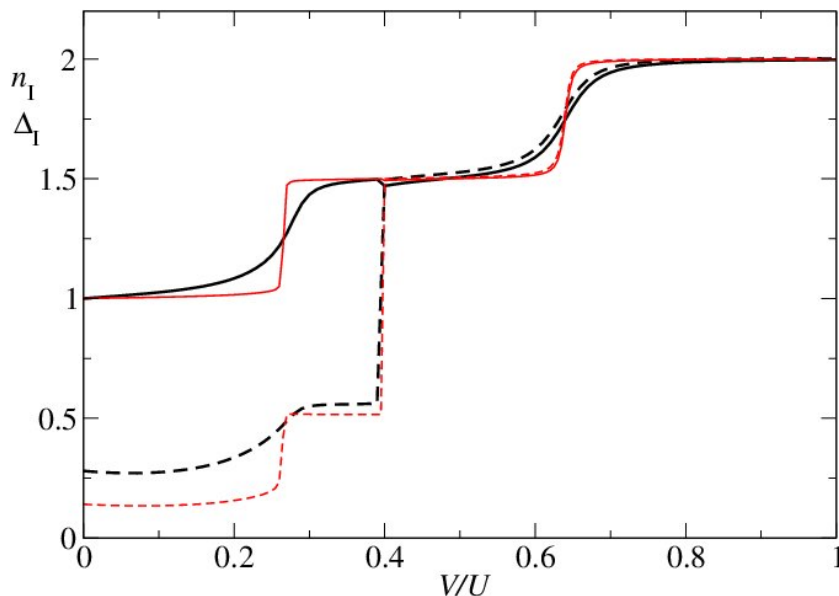


FIGURE 2.7: Occupation of type-I sites,  $n_I$  for  $U/J = 10$  (solid black line) and  $U/J = 20$  (solid red line). The corresponding variance  $\Delta_I$  is plotted for  $U/J = 10$  (black dashed line) and  $U/J = 20$  (red dashed line). For a discussion see text.

To summarize we have looked at the affect two different polarizations on a small lattice ring filled with dipolar bosons. We have shown that this model although quite simple still displays very rich phenomena. We showed analytically as well

as numerically that at small  $V/U$  the dipolar interactions increase the superfluid character of the system. For a polarization out of the plane of the ring sharp crossovers have been noted between a variety of density wave phases as we scanned over  $V/U$ . For polarization in the plane of the ring a splitting of the condensate was observed and was later followed by a complete symmetry breaking (similar to the results for a toroidal trap without the lattice [36]). The existence of the small optical lattice caused sharp transitions due to rearrangement of dipoles on opposite sides of the ring where an attractive head-to-tail orientation of the dipoles occurred.

# Chapter 3

## Hard-core dipolar bosons on a triangular lattice

### 3.1 Introduction

In Chapter 1 we mentioned that one of the more promising ways of creating a quantum simulator is by using trapped ions. As we recall, the idea was first introduced by Porras and Cirac in 2004 [19]. From there we established that the behavior of the ions could accurately be interpreted by the typical spin Hamiltonian given by Eq. (1.23). From this work we can derive an effective spin Hamiltonian in order to simulate different lattice spin models. Here we use a model called the XXZ model and is described by the Hamiltonian,

$$H = J \sum_{i,j} \frac{1}{|i-j|^3} [\cos \theta (S_i^z S_j^z) + \sin \theta (S_i^x S_j^x + S_i^y S_j^y)] - \mu \sum_i S_i^z \quad (3.1)$$

where  $\mu$ , which is the chemical potential, acts like an external magnetic field,  $J$  scales the interactions, and  $S_i^\alpha$  are the spin operators at site  $i$ . In this case we will be working with  $S = 1/2$  particles. As we can see all of the interactions are governed by a dipolar decay ( $1/r^3$ ) behavior. This is because the lattice vibrations, which are created by the Coulomb force, are the main mechanism that controls all the interactions and therefore all the interactions will have the same decay rate.

In the Hamiltonian (3.1) we can see that the ratio of the tunneling to dipolar repulsion is scale by the coefficient  $\theta$  [37, 38]. There is however a way to simulate quantum magnetism where the hopping term is short-ranged while the dipole term continues to be long-ranged. This method uses the rotational structure of ultra cold molecules and was first proposed in Ref. [39, 40]. As we can see the XY or tunneling term is now restricted solely to its nearest neighbors while the ZZ or interaction term decays like the dipole-dipole interaction.

It is the long-ranged behaviors of the system that will be the most fascinating and challenging since these are the interactions that are usually neglected. The dipolar effects introduce new physics into the conventional short-ranged systems and therefore can host a multitude of other phases besides the well known Mott insulating, superfluid, and crystal phases. One of the more interesting phases that can arise for soft-core bosons with long-ranged interactions is the Haldane phase as identified in [23]. This phase is characterized by antiferromagnetic (AFM) order between empty sites and sites with double occupancy, with an arbitrary long string of sites with unit occupancy in between. In usual insulating phases, the length of the string is fixed by a filling factor rather than having a random length. Another unusual phase that can occur due to the presence of dipolar interactions is the celebrated supersolid phase. In an extended Bose-Hubbard model of soft-core bosons (with nearest neighbor interactions only), for both one and two dimensions, a stable supersolid phase appears. In the one dimensional case a smooth continuous transition can be seen [41] while for the two dimensional case there is a sharp first-order transition [42]. Now if the dipole-dipole interactions are extended beyond the typical nearest neighbor interactions then a stable supersolid can be achieved even for the case of hard-core bosons [43, 44]. However in this situation there arise a large number of metastable states [45, 46] (for a review see [11]). By tuning the direction of the dipoles, incompressible regions like devil's staircase structures have been predicted in Ref. [47]. While being interesting, long-range interactions make computer simulations of such systems quite difficult. On the other hand, since ions in optical lattices may be extremely well controlled, they form an ideal medium for a quantum simulator.

In an earlier study [48], we considered both the mean-field phase diagram for the system (3.1) as well as a 1D chain using different quasi-exact techniques, such as density matrix renormalization group (DMRG), and exact diagonalization for small systems. Here, we would like to concentrate on frustration effects on a 2D triangular lattice using a quantum Monte Carlo (QMC) approach.

In this chapter we will be looking at spin-1/2 particles or in the case of trapped ions, two internal ion states as was proposed by Porras and Cirac in [20]. These spin-1/2 particles can be mapped onto a system of hard-core bosons by applying spin-wave theory. We employ the Holstein-Primakoff transformation in order to map the angular momentum operators into the boson creation and annihilation operators. The transformation can be written as

$$S^- = (\sqrt{2S - n})b \quad (3.2)$$

$$S^+ = b^\dagger(\sqrt{2S - n}) \quad (3.3)$$

$$S^z = n - S \quad (3.4)$$

where  $S$  is the total spin and the spin operators continue to obey their commutation relationships,  $[S^\alpha, S^\beta] = i\epsilon^{\alpha\beta\gamma}S^\gamma$ . While  $n = b^\dagger b$  and  $[b, b^\dagger] = 1$  are the usual bosonic operators that obey the bosonic commutation relationships. Now let's take a look at one of the square root terms in the above equations and rewrite it slightly

$$\sqrt{2S - n} = \sqrt{2S} \left(1 - \frac{n}{2S}\right)^{1/2}. \quad (3.5)$$

Now we can expand it using a Taylor series expansion

$$\sqrt{1 - x} = \sum_{n=0}^{\infty} \frac{(-1)^n (2n)!}{(1 - 2n)(n!)^2 (4^n)} x^n = 1 + \frac{x}{2} - \frac{x^2}{8} + \dots \quad (3.6)$$

Applying this expansion to our equation we get

$$\sqrt{2S - n} = \sqrt{2S} \left(1 - \frac{n}{4S} - \frac{n^2}{32S^2} - \dots\right). \quad (3.7)$$

The reason that we are able to approximate our spins in this fashion is because  $\langle n_i \rangle \ll 1$ . In other words, we are able to neglect interactions between excitations,  $n_i n_j \approx 0$ . We will only keep the first term of the expansion and this way we are able to simplify our transformations into

$$S^- = b \quad (3.8)$$

$$S^+ = b^\dagger \quad (3.9)$$

$$S^z = n - 1/2. \quad (3.10)$$

If we now plug these new operators into our Hamiltonian 3.1 and we can rewrite it in its bosonic form as

$$\begin{aligned} H &= J \sum_{i,j} \frac{1}{|i-j|^3} \left[ \cos \theta \left( n_i n_j - \frac{n_i}{2} - \frac{n_j}{2} + \frac{1}{4} \right) \right] \\ &+ J \sum_{i,j} \frac{1}{|i-j|^3} \left[ \frac{\sin \theta}{2} \left( b_i^\dagger b_j + b_j^\dagger b_i \right) \right] \\ &- \mu \sum_i \left( n_i - \frac{1}{2} \right). \end{aligned} \quad (3.11)$$

We must keep in mind that these are hard-core bosons which implies that only a single one will be allowed per site or  $b^2 = (b^\dagger)^2 = 0$ . This limit corresponds to the case where the on-site repulsion  $U$  goes to infinity in the standard Bose-Hubbard model. In this version of the Hamiltonian a spin up particle is represented by a filled site while a spin down particle is represented by an empty site. From this point on, the text will mostly use the language of hard-core bosons.

## 3.2 1D review and results

In order to form some intuition about possible physical effects due to the LR interaction and tunneling, we now discuss briefly the ground-state phase diagram of the Hamiltonian in 1D. For hard-core bosons, which is the topic of this chapter, the one-dimensional version of the Hamiltonian has been thoroughly investigated in the past [48] (see also [49, 50] for the special cases  $\theta = 0$  and  $\theta = \pi/2$ ). For

reference, we reproduce in Fig. 3.1 the phase diagrams for the system with dipolar interaction and NN tunneling, as well as the system with both the interaction and the tunneling terms dipolar.

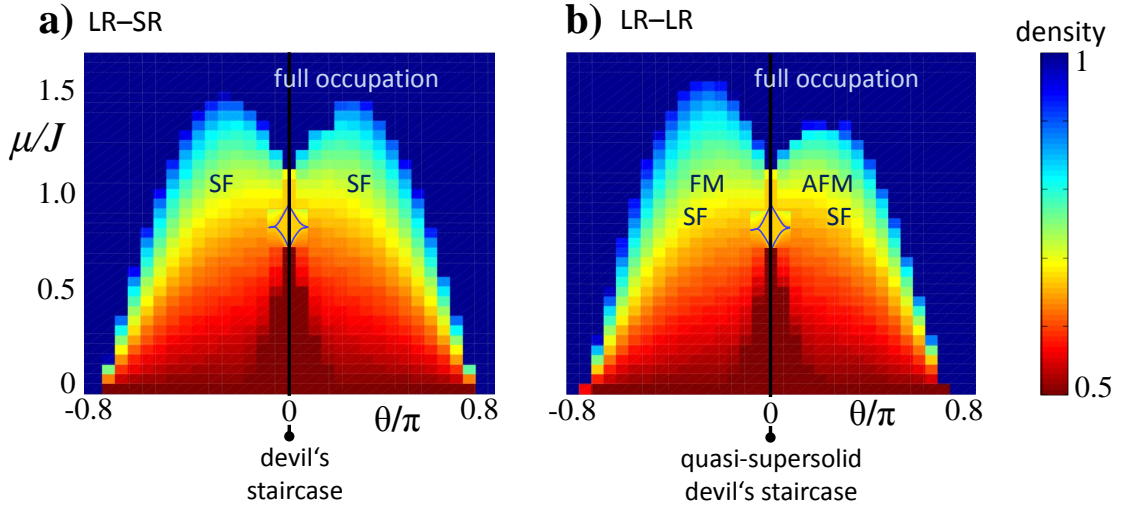


FIGURE 3.1: Phase diagram of the 1D system with dipolar interactions and (a) nearest-neighbor tunneling, (b) dipolar tunneling. The phases are labeled according to density matrix renormalization results, while the actual data shown comes from the infinite time evolving block decimation method (with interactions truncated at next-to-nearest-neighbors), both from Ref. [48]. Along the black line, there exists a devil's staircase of crystal states. At finite tunneling, for (a), these spread into conventional insulating states, while for (b), they form quasi-supersolids. The dark blue lines sketch the crystal lobes at  $2/3$ -filling. Their cusp-like structure is typical for 1D systems. In 2D, they are expected to be rounded off, similar to Mott-lobes of the Bose-Hubbard model [51]. For nearest-neighbor tunneling, (a), the superfluid (SF) phases can be mapped into one another, while for nearest-neighbor dipolar tunneling, (b), they are distinct on the ferromagnetic (FM,  $\theta < 0$ ) and the antiferromagnetic side (AFM,  $\theta > 0$ ). Note also that in (b) frustration leads to an asymmetry between  $\theta < 0$  and  $\theta > 0$ .

At zero tunneling, the ground states are periodic crystals where — to minimize the dipolar interaction energy — occupied sites are as far apart as possible for a given filling factor [49]. For finite 1D systems and very small tunneling such a situation persists as exemplified in [52]. For infinite chains in 1D, every fractional filling factor  $n = p/q$  is a stable ground state for a portion of  $\mu$  parameter space. The extent in  $\mu$  decreases with  $q$ , since at large distances the dipolar repulsion is weak and thus cannot efficiently stabilize crystals with a large period. This succession of crystal states is termed the devil's staircase. This name derives from its surprising mathematical properties, challenging naive intuitions about

continuity and measure: since all rational fillings are present, it is a continuous function; moreover, its derivative vanishes almost everywhere (i.e., it is non-zero only on a set of measure zero) — and still it is not a constant, but covers a finite range.

At finite tunneling, the crystals spread into lobes similar to the Mott lobes of the Bose-Hubbard model. If the tunneling is only over NNs, these Mott lobes are not sensitive to the sign of the tunneling and they form standard insulating states with diagonal long-range order (LRO) and off-diagonal short-range order, Fig. 3.1 (a). For long-range dipolar tunneling, the extent of the lobes is asymmetric under sign change  $\theta \rightarrow -\theta$ : frustration effects stabilize the crystal states for  $\theta < 0$ , while the ferromagnetic (FM) tunneling for  $\theta > 0$  destabilizes them, Fig. 3.1 (b). Moreover, the crystal states acquire off-diagonal correlations which follow the algebraic decay of the dipolar interactions [48]. This coexistence of diagonal and off-diagonal (quasi-)LRO turns the crystal states into (quasi-)supersolids. The occurrence of such phases for hard-core bosons in 1D is truly exceptional, since the systems where it appears consist typically of soft-core bosons [41, 42], or two-dimensional lattices [43]. Furthermore, this 1D quasi-supersolid defies Luttinger-liquid theory, which typically describes 1D systems very well, even in the presence of dipolar interactions [53–55]. Where Luttinger-liquid theory applies, diagonal and off-diagonal correlations decay algebraically with exponents which are the inverse of one another. Therefore, if the diagonal correlations show LRO, the corresponding exponent is effectively 0, and the exponent for the off-diagonal correlations is infinite, describing an exponential decay. In our case, this exponent remains finite in the quasi-supersolid phase and the above relationship clearly does not hold.

At even stronger tunneling strengths, the crystal melts and the system is in a SF phase. The LR tunneling and interactions influence the correlation functions at large distances and therefore also modify the character of this phase [48, 50].

These results show that in this system the dipolar interactions considerably modify the quantum-mechanical phase diagram. In higher dimensions, we can expect

the influence of long-range interactions to be even stronger, which makes extending these studies to a two-dimensional lattice highly relevant. For example, one can expect that — if quasi-supersolids appear already in 1D — the long-range tunneling has a profound effect on the stability of two-dimensional supersolids, which appear in triangular lattices at the transition between crystal and superfluid phases [41, 56–58]. Also, the frustration effects already observed in the 1D system should be much more pronounced in the triangular lattice, simply due to the increased number of interactions.

Further, such an analysis is especially relevant at finite temperature. In fact, a recent work scanned the phase diagram of Hamiltonian 3.1 along the line  $\mu = 0$  in a square lattice [38]. There, the authors found that above the superfluid on the FM side (i.e.,  $\theta < 0$ ), the continuous U(1) symmetry of the off-diagonal correlations remains broken even at finite temperatures.

For these reasons, we can expect intriguing effects of the long-range tunneling for the two dimensional triangular lattice, to which we turn now.

### 3.3 2D results

Let us now extend the study to a two dimensional triangular lattice filled with hard-core bosons. For this case we will be using a quantum Monte Carlo (QMC) method at a finite temperature in order to calculate the needed observables. The temperature needs to be kept low in order to guarantee that the solutions will give the ground state properties of the system. The lattice sizes are kept relatively small to be able to keep the calculation times reasonable. Specifically we will look at a triangular lattice with  $N = L \times L$  sites where  $L$  will vary from 6 to 12. It is important to note that as we change the size of the system we will also be changing the extent to which the long-ranged interactions work. This means that at larger lattices sizes the dipolar interactions will have a farther reaching effect. In the chapter we focus mainly on the Wigner crystals that form at  $2/3$  filling. In

a Wigner crystal the particles are evenly dispersed across the entire lattice in such a way that a maximum amount of space is kept between the particles.

The type of model that we are studying has a property that is known as frustration. It can be defined as the inability to find the true ground state due to the fact that there does not exist an optimal configuration that minimizes the energy of the system. In the case of a triangular lattice, where the spins would like to align in an anti-ferromagnetic order, there arises a problem when we look at all three points of the triangle. When one site has a spin oriented in the "up" direction and a second site has a spin oriented in the "down" direction then the third site does not know how to orient itself. In order to minimize the energy on one bond the spin wants to align itself in the "down" direction while to minimize the energy on the other bond it wants to be in the "up" direction. This means that there exist two equivalent states where one bond is optimized while the other is not. A graphical representation of the situation is presented in Fig. 3.2 (a). If we look at a square lattice we do not have this problem as long as the interactions are only to the nearest neighbor. It is quite easy to set up an anti-ferromagnetic order on such 2D lattice where each site the spins are arranged in the opposite direction. If we extend the range of interactions out to the next nearest neighbor then again we are faced with the effects of this geometric frustration. While the bonds along the sides of each square create no conflicts, in aligning the spins into an anti-ferromagnet, the interactions along the diagonals counteract this behavior. So if the different hopping terms, say  $J_1$  and  $J_2$ , are chosen correctly this will again result in degenerate states where there exists no optimal ground state configuration. Again this is shown graphically, this time in Fig. 3.2 (b).

A second stumbling block of this model is related to the sign problem that exists in the QMC code. If we keep  $\theta < 0$  this problem does not arise but once  $\theta$  becomes non-negative the code (in certain parameters) breaks down. The reason is that certain calculations of the probability come out negative because now the tunneling term is of the opposite sign. Since negative probabilities have no physical meaning the solutions to the code are nonsensical. There are however methods that can be used to minimize (if not totally avoid) the sign problem. For example, the sign

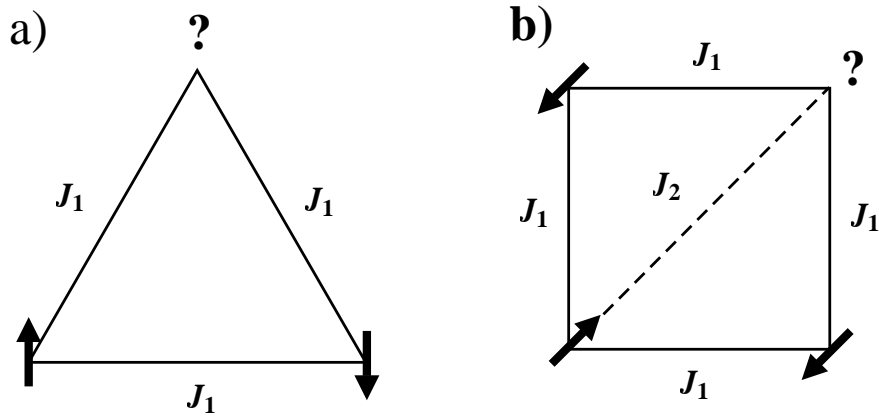


FIGURE 3.2: Panel (a) shows the effect of frustration caused by the geometry of a triangular lattice. When two corners have spins that want to arrange in an anti-ferromagnetic way then the third corner cannot minimize its energy on both bonds at the same time. Panel (b) shows a square lattice where the long-ranged interactions are now the cause of the frustration effects. If only nearest neighbor interactions exist then there is no problem however when we take into account the next nearest neighbors the ratios of the different tunneling terms,  $J_1$  and  $J_2$ , can again create a situation where the final dipole does not have a way to minimize its energy.

problem only appears for long-ranged XY interactions, while the ZZ (Ising-like) interactions are not affected by it. Later we will study some results where  $\theta > 0$  and we will see where exactly the simulation breaks down but for the majority of this chapter we will focus our attention on values of  $\theta$  that are less than zero.

Let's now take some time in order to understand exactly what is the sign problem. Without too many details, we'll try to explain where this issue comes from. Basically in the QMC code we try to map the quantum partition function onto a classical problem.

$$Z = \text{Tr} e^{-\beta H} = \sum_i p_i \quad (3.12)$$

A problem can arise when the probability amplitudes are not positive definite,  $p_i < 0$ . This, in our case, occurs if the tunneling parameters have a negative sign, which happens when  $\theta > 0$ . These bond terms cause negative probabilities for the world line configurations that cause numerical instabilities when summing over paths. In other words, large amplitudes of one phase can completely negate other

large contributions but with the reverse phase. There are a few ways to try to handle the sign problem but there is no real solution to it since it is an NP-hard problem and a solution to this would solve all NP-hard problems. One attempt is to look at the absolute values of the probabilities. In this way when we look at the thermal average it can be written as such,

$$\langle A \rangle = \frac{\sum_i A_i p_i}{\sum_i p_i} = \frac{A_i \sum_i \text{sgn } p_i |p_i| / \sum_i |p_i|}{\sum_i \text{sgn } p_i |p_i| / \sum_i |p_i|} = \frac{\langle A \cdot \text{sign} \rangle_{|p|}}{\langle \text{sign} \rangle_{|p|}} \quad (3.13)$$

where obviously the partition function is now defined as

$$Z = \sum_i |p_i| \quad (3.14)$$

Now the average sign becomes very small

$$\langle \text{Sign} \rangle_{|p|} = \frac{1}{Z_{|p|}} \sum_i \text{sgn } p_i |p_i| = \frac{Z}{Z_{|p|}} = e^{-\beta V \Delta f}. \quad (3.15)$$

However the error of the sign grows quite quickly. It is defined by

$$\frac{\Delta \text{Sign}}{\langle \text{Sign} \rangle_{|p|}} = \frac{\sqrt{\langle \text{Sign}^2 \rangle_{|p|}} - \langle \text{Sign} \rangle_{|p|}^2}{\sqrt{N} \langle \text{Sign} \rangle_{|p|}} \approx \frac{\sqrt{\langle 1 \rangle_{|p|}}}{\sqrt{N} \langle \text{Sign} \rangle_{|p|}} = \frac{e^{\beta V \Delta f}}{\sqrt{N}} \quad (3.16)$$

and so we would need an order of  $N = \exp(2\beta V \Delta f)$  measurements for sufficient accuracy.

The sign problem is basis dependent and so there are also possibilities of avoiding it simply by just switching bases. This can cause all the probabilities to be greater than or equal to zero. This, however, does not always solve the problem of having the algorithm exhibit exponential scaling.

In this chapter we will look at several variations that our model. We will study the system when all the interactions, both tunneling and dipolar, are long-ranged (LR-LR), when only the dipole-dipole interactions are long-ranged while the tunneling is only nearest neighbor (LR-SR), and finally when both the interactions are short ranged (SR-SR). The case where both interactions are short-ranged, corresponds to the nearest neighbor XXZ model and is relevant for magnetic materials with

planar anisotropy in their couplings. The LR-SR model works well to describe polar molecules like in the case of [59]. Finally the LR-LR model will be studied here where the far reaching interactions will extend out to the maximum possible value (i.e. the distance before there is any overlap). For example a system where  $L = 6$  can have interactions extend out to 5 nearest neighbors. This means that each site will feel the interaction of 36 other sites. For the short-ranged interactions each site only interacts with its 6 nearest neighbors. Each one of these instances will have its own behavior and display different crystal, superfluid, and supersolid regions. By comparing all the cases we will be able to truly see what effects the long-ranged interactions will have on the system.

### 3.3.1 Vanishing tunneling

The first calculation, which creates the motivation for the rest of the chapter, is to look at the case of vanishing tunneling and temperature for each system (LR-LR, LR-SR, and SR-SR). Here, similar to the 1D devil's staircase, at vanishing temperature a series of insulating crystal states is expected to cover the entire range of  $\mu/J$ . Since we are interested in finite temperature results, we set  $T = 0.1$  — which should still be low enough to reflect the characteristics of the ground-state phase diagram — and look for plateaus in the density. We distinguish short- and long-ranged ZZ interactions. From Fig. 3.3, left panel, we can see that the only plateau (besides the completely filled system) that appears is at  $\rho = 2/3$  (corresponding either to  $2/3$  boson filling or in spin terms, a lattice with  $2/3$  of the spins oriented up and  $1/3$  oriented down) for both short- and long-ranged interactions. Scaling the system size from  $L = 6$  to  $L = 12$  causes no change for the short-ranged interactions, and minimal change for the long-ranged ones. The key difference is in the size and position of the short-ranged and the long-ranged plateaus. For short-ranged interactions this plateau is larger and centered around  $\mu/J \simeq 1.5$ , while the long-ranged interactions have a smaller plateau centered around  $\mu/J \simeq 1.85$ . The finite width of these plateaus suggests that a  $2/3$ -filling Wigner crystal persists also for some finite  $\theta$ . The right panels of Fig. 3.3 show

how the plateau shrinks with increasing temperature, as well for SR interactions (top right panel) as for LR interactions (bottom right panel). In the latter case, in fact, by  $T = 0.25$  the plateau has completely disappeared. We can also notice that at  $T = 0.05$  there are signs of some of the other plateaus, most noticeably the 3/4-filling plateau. The rest of the paper will focus on the 2/3-filling crystal lobes and their properties.

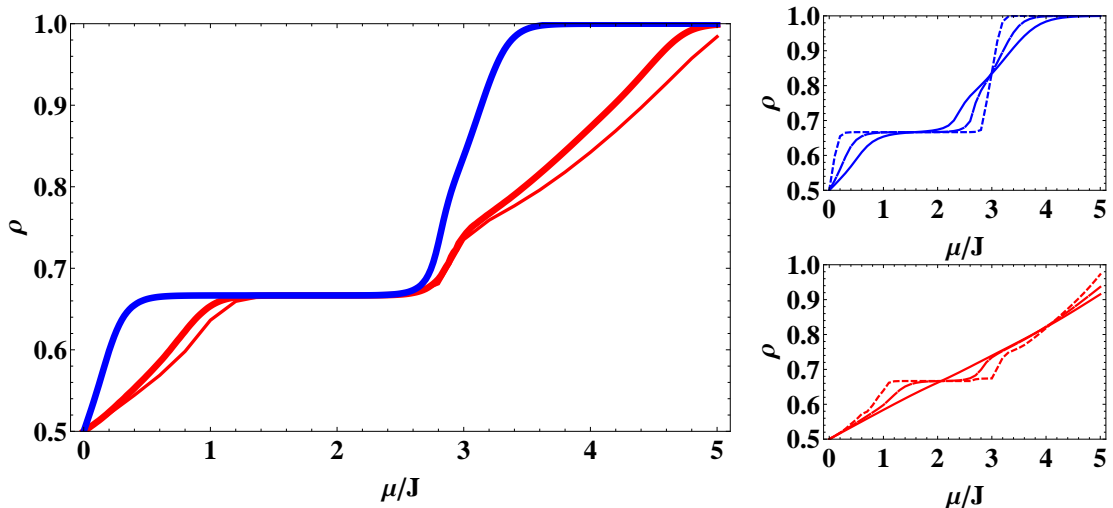


FIGURE 3.3: The graph on the left displays  $\theta = 0$  and  $T = 0.1$ , where the density shows a single plateau for 2/3-filling. For SR interactions (solid blue line), different curves for  $L = 6, 9, 12$  coincide, and for LR interactions (solid red:  $L = 6$ , dashed red:  $L = 9$  and  $12$ ) the size dependence is small. The panels on the right are at fixed  $L = 12$  and  $\theta = 0$  for different temperatures  $T = 0.05, 0.15, 0.25$  (from dotted to dashed to solid). Both for SR (top right) and LR interactions (bottom right), the 2/3-filling plateau shrinks as  $T$  increases.

### 3.3.2 Low-temperature phase diagram at finite tunneling

We now introduce a finite tunneling by choosing  $\theta < 0$  in our Hamiltonian, and study the properties around the 2/3-filling crystal. We calculate the density and the superfluid fraction. The superfluidity is measured using the winding numbers calculated from the movement of the worms in the QMC code. In order to get this value the system must have periodic boundary conditions so that the world lines can properly “wind” around the system. The superfluid fraction is

$$\rho_s = \frac{\langle W^2 \rangle}{4\beta}, \quad (3.17)$$

where  $W$  is the winding number fluctuation of the world lines and  $\beta$  is the inverse temperature.

Figure 3.4 shows the results for the boson density of a  $L = 6$  triangular lattice at  $T = 0.1$ . For all types of interactions we see that as  $\theta$  increases in absolute value the  $\rho = \frac{2}{3}$  plateau shrinks, because larger  $|\theta|$  increases the ratio of hopping to dipolar interactions. This introduces more kinetic energy and the crystal melts into a superfluid. It can be seen for the SR-SR system that the boson density lobe extends to  $\theta \simeq -0.36$ , while for the LR-SR interactions it ends at  $\theta \simeq -0.3$ , and finally for LR-LR interactions the lobe is smaller still, only going out to  $\theta \simeq -0.2$ . The behavior is explained by the fact that the increased amount of interactions cause a quicker melting of the lobe.

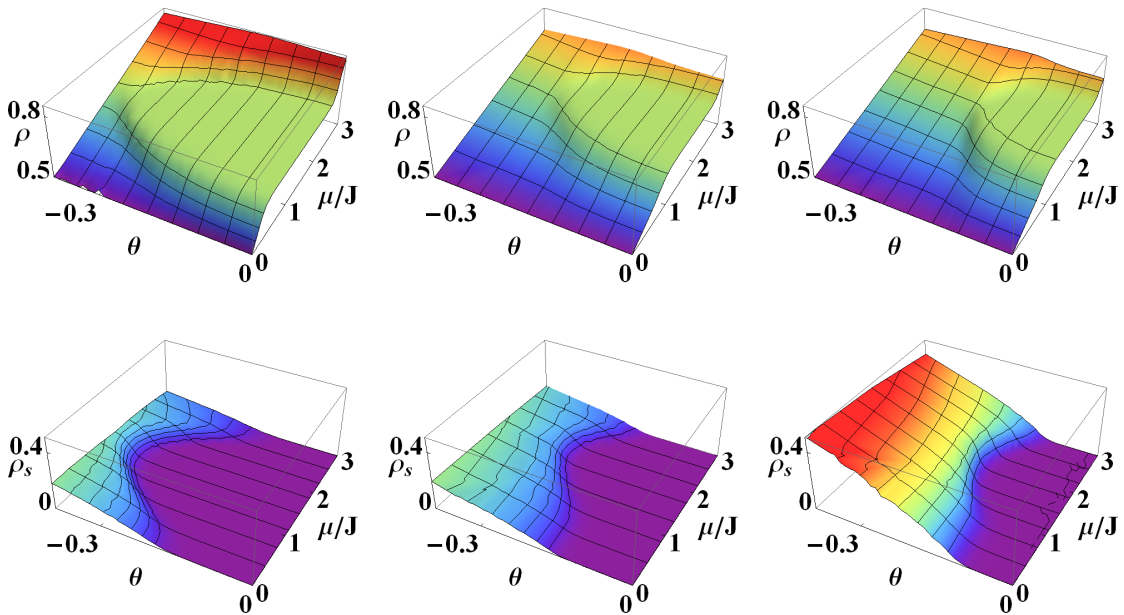


FIGURE 3.4: The columns show the  $\rho = 2/3$  lobes, evidenced by particle density (top row) and the superfluid fraction (bottom row) that arise under varying the ratio,  $\theta$ , and the chemical potential,  $\mu/J$  (data for  $L = 6$ ). The left column corresponds to the SR-SR system, the middle one shows the LR-SR system and the right column depicts the lobes for the LR-LR system. Long-ranged dipolar interactions decrease the lobes in  $\mu/J$  due to the appearance of devil's staircase like features, and long-range tunneling decreases the extent of the lobe in  $\theta$ .

A second major observation is the shift in the position of the lobes. While the short-ranged lobe exists approximately for  $0.3 < \mu/J < 2.7$ , the long-ranged lobes lie generally on the interval  $1.0 < \mu/J < 2.8$ . For a system like this at  $T = 0$ , one expects the  $\rho = \frac{2}{3}$  lobe to exist on the range  $0 < \mu/J < 3$  with a mirrored image

of the  $\rho = \frac{1}{3}$  lobe at  $-3 < \mu/J < 0$ . The existence of the two identical lobes is explained by particle-hole symmetry [56–58]. The lobes are separated with a kind of mixed solid in between (with coexistence of 1/3- and 2/3-filling regions) The existence of this region may be caused by several phenomena. It could either be an effect of the finite temperature as in Ref. [60], or due to the existence of many metastable states caused by a devil’s staircase like behavior, similar to what was observed in Ref. [47].

Again referring to the  $T = 0$  phase diagram, we expect that there is a region of supersolidity that extends in between the lobes and goes all the way to their base at  $\theta = \mu = 0$  [56]. In our system this region should exist near the tip of the lobe but not extend all the way to the base due to the finite temperature and the resulting mixed solid. Looking at Fig. 3.4, it is obvious indeed that, if a supersolid region exists, it can only be near the tip of the lobe because the superfluidity is zero a significant way up the lobe. Judging by the increased separation of the long-ranged lobes, we can assume that the supersolid region for these systems should increase in size to fill the region in between. To search for the supersolid phase, we now compare the superfluidity with the static structure factor. The structure factor is defined as the Fourier transform of the density-density correlations,

$$S(\mathbf{Q}) = \left\langle \left| \sum_{i=1}^N n_i e^{i\mathbf{Q}\mathbf{r}_i} \right|^2 \right\rangle / N^2. \quad (3.18)$$

Here, we focus on the wave vector  $\mathbf{Q} = (4\pi/3, 0)$ , which corresponds to the  $\sqrt{3} \times \sqrt{3}$  order parameter that is associated with 1/3- and 2/3-filling crystals on the triangular lattice. For the case of the 2/3-filling lobe that we are interested in, it will show plateaus over the same range of  $\mu$  as the density, but additionally gives insight into the arrangement of the bosons on the lattice. This makes it a useful quantity in searching for supersolid regions. In fact, a supersolid exists when both the structure factor and the superfluid fraction have non-zero values. The physical mechanism behind the supersolid phenomenon is based upon the appearance of extra holes (particles). The underlying crystal structure has  $\sqrt{3} \times \sqrt{3}$  order on

a triangular sublattice of the physical lattice. The extra holes (particles) are free to move around on the rest of the lattice as superfluid objects. In this way, the system retains a crystal structure, while it acquires at the same time the long-range coherence of a superfluid. Due to the hole (particle) doping, it forms in sections away from commensurate filling, in this case in between the 1/3- and 2/3-filling lobes.

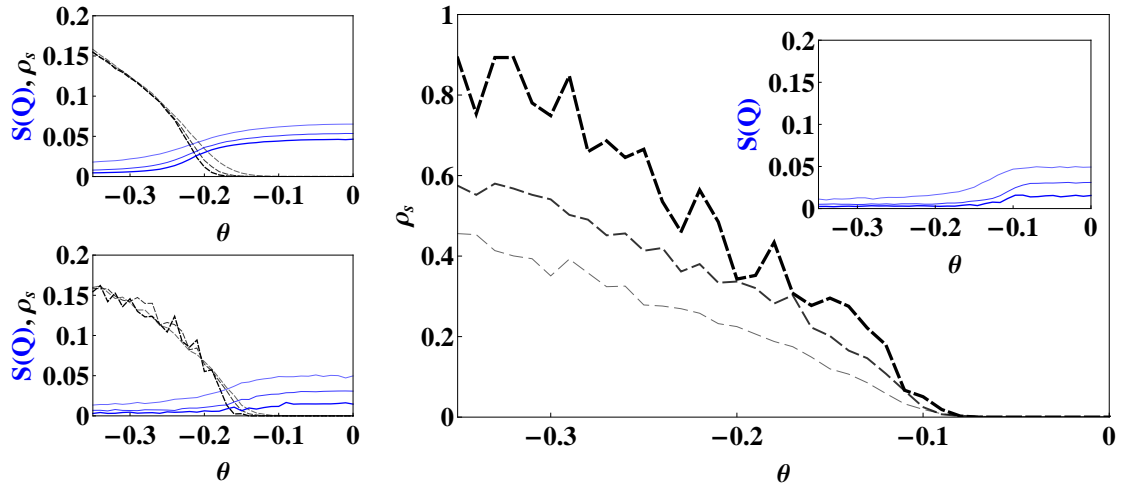


FIGURE 3.5: Cuts at  $\mu/J = 0$  for SR-SR (left top), LR-SR (left bottom) and LR-LR (right) for a  $L = 6, 9$ , and  $12$  lattice (lines become thicker and darker with increasing system size). For all cases, the structure factor (solid blue) is finite at small  $\theta$  and the superfluid fraction (dashed black) at large  $\theta$ . At the system sizes studied, there appears a supersolid region at intermediate  $\theta$  where both structure factor and superfluid fraction are finite. In the LR-LR system there is a reversal of finite size effects. In this case the superfluid fraction for larger systems becomes higher instead of lower.

Taking “slices” out of the crystal lobes we now check where there is a supersolid region and where the system transitions directly from crystal to superfluid. Also we study the nature of these transitions to see if they are of first or second order.

The most logical region to look for supersolids is directly in between the 1/3- and 2/3-filling lobes, at  $\mu/J = 0$ . Figure 3.5 shows the behavior of the SR-SR, the LR-SR, and the LR-LR system at this cut for several system sizes. Structure factor and superfluidity reveal, for all the systems, three different regions. In each case, the system starts at  $\theta = 0$  in a solid phase where the superfluid fraction is zero but the structure factor is finite. It transitions smoothly into a supersolid region

where both superfluidity and structure factor are non-zero. Finally, the structure factor smoothly drops away and leaves just a non-zero superfluid fraction, making the final phase a superfluid. In each system, the size of the supersolid region is different. In the SR-SR case, the supersolid region begins to appear at  $\theta \simeq -0.15$  for a  $L = 6$  lattice. As the size grows to  $L = 12$ , the region has shifted to  $\theta \simeq -0.19$  with the superfluid curves becoming sharper. The increased system size also reduces the value of the structure factor a little. From [57], we know that at even larger sizes (but  $T = 0$ ) the supersolid will continue to exist in this type of system. For the LR-SR system the supersolid region appears at a similar point and also shifts with system-size increase. The structure factor on the other hand has a significant decrease for larger system sizes. It is difficult to tell if at greater sizes the existence of the supersolid will persist. The final graph shows the LR-LR system. In this system, superfluidity appears even before  $\mu/J$  reaches  $-0.1$ . In this system, the superfluid fraction is much greater than in the previous two because of the long-ranged tunneling. This means that at small system sizes the supersolid region is much more prominent relative to the crystal lobe. The structure factor diminishes with system size almost exactly as in the LR-SR case except that the transition is at a different value of  $\theta$ , and near  $\mu/J = 0$  it drops to slightly lower values. Due to this strong decrease, for any situation with long-range interactions we cannot clearly state whether the supersolid region survives at larger system sizes.

Next we take vertical cuts at a value of  $\theta = -0.15$ , since this is a reasonable place for a supersolid to exist for the LR-LR system ( $\simeq 80\%$  of the tip of the lobe). We compare all the systems at this cut, and study the behavior of the superfluid fraction and the structure factor, plotted in Fig. 3.6. For SR-SR interactions, no supersolid region appears. On one side of the lobe there is a sharp phase transition directly from the crystal to the superfluid phase, while on the other side there is a slower change from one solid form to another ( $\rho = 1/3 \rightarrow 2/3$ ). The finite-size scaling in the figure shows that as the size increases the transitions of the structure factor become even sharper, although they stay continuous due to the finite temperature. The values of the superfluid fraction decrease as the system

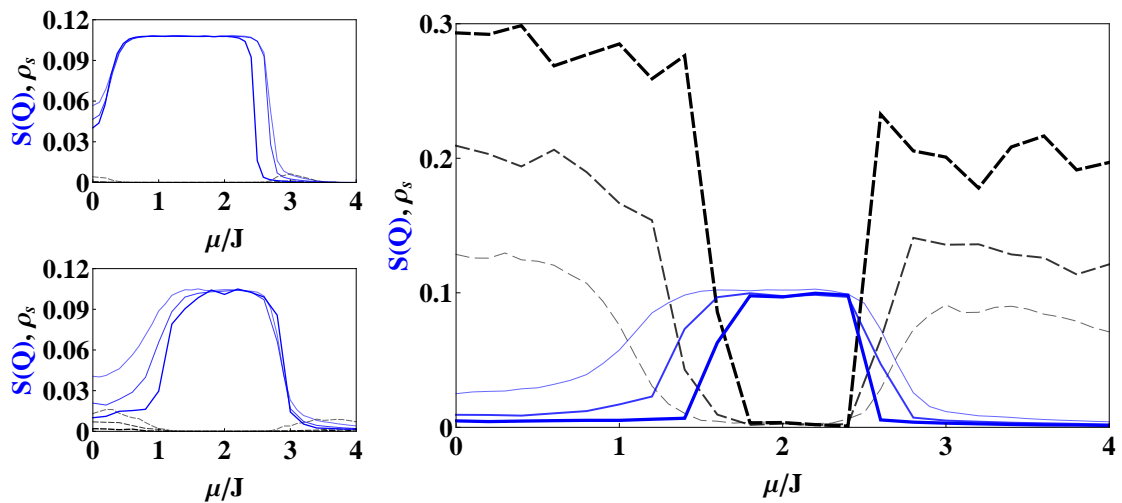


FIGURE 3.6: Cuts at  $\theta = -0.15$  for SR-SR (left top), LR-SR (left bottom), LR-LR (right) for a  $L = 6, 9,$  and  $12$  lattice (lines become thicker and darker with increasing system size). Solid blue: Structure Factor. Dashed black: Superfluid fraction. At this value of  $\theta$ , for short-range tunneling, the superfluid fraction disappears rapidly with increasing system size, while for long-range tunneling it even increases. At  $\mu/J \approx 1.75$ , possibly a supersolid may survive in large lattices. Again in the LR-LR system there is a reversal of finite size effects. The superfluid fraction for larger systems becomes higher instead of lower.

sizes increases and essentially disappear at  $L = 12$ . In the LR-SR system, a hint of the supersolid phase begins to appear on either side of the lobe. It is a bit more evident on the side where  $\mu/J$  is small (as is to be expected from references such as [56]), but it also arises on the opposite side. This is contrary to a system of only short-ranged interactions where this supersolid region appears only on one side of the lobe and not both. At larger sizes, also in the LR-SR system the transitions become sharper and the superfluidity gets smaller. The final and most interesting cut is taken out of the LR-LR lobe. In this system, we see a smooth transition from crystal to supersolid at  $\mu/J \simeq 2.4$  and at  $\mu/J \simeq 1.4$  for  $L = 6$ . For larger systems the transition at  $\mu/J \simeq 2.4$  occurs at the same spot but becomes sharper, making the supersolid region disappear. At  $\mu/J \simeq 1.4$  the transition shifts to a higher value of  $\mu/J$ , making the  $2/3$ -filling plateau smaller. It also becomes less smooth but the supersolid region remains longer than for the SR-SR case. In the LR-LR system, the superfluid fraction for larger systems has the opposite effect than for the previous cases, it becomes higher instead of lower.

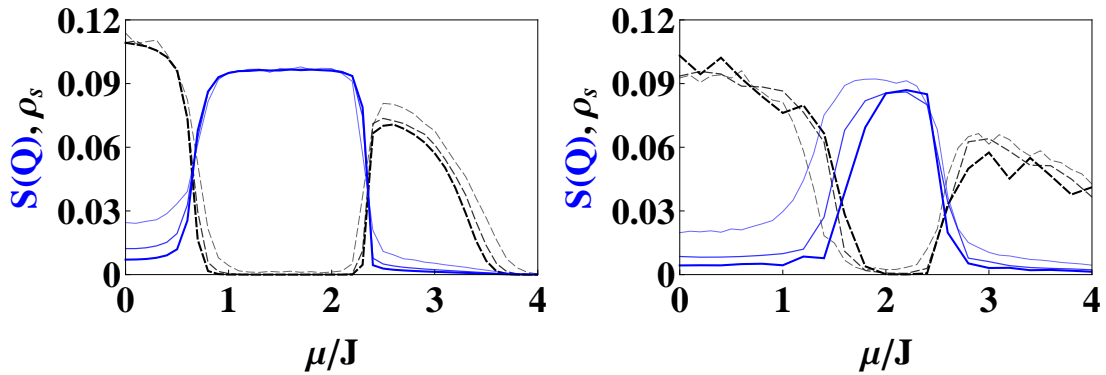


FIGURE 3.7: SR-SR (left) at  $\theta = -0.28$  and LR-SR (right) at  $\theta = -0.23$ . Solid blue: Structure Factor. Dashed black: Superfluid fraction. Lines become thicker and darker as system size goes up. In the SR-SR system, a supersolid at small  $\mu/J$  persists at large systems, while at  $\mu/J \approx 2.4$  the transition from crystal to superfluid becomes a direct first-order transition. For the LR-SR system, the curves change slowly at both sides of the crystal lobe, leading to persisting supersolids.

A perhaps fairer comparison is to look at a cut through a region where we are sure the supersolid exists for all three systems. Therefore, in Fig. 3.7 we look at two more cuts that are now taken closer to the tips of the SR-SR and LR-SR lobes. As with the LR-LR system (last panel of Fig. 3.6), these lie at around 80% of the tip of the lobe. In the SR-SR lobe, the cut is taken at  $\theta = -0.28$ . Here we see a similar behavior for the structure factor as we did in the  $\theta = -0.15$  cut of the lobe, but this time the superfluid fraction plays a much more important role. On the one side,  $\mu/J \simeq 2.4$ , both the superfluid fraction as well as the structure factor have sharp transitions that become even sharper at larger sizes. In fact, at  $T = 0$  these transitions have been shown to be of first order, and the system goes directly from crystal to superfluid. Due to the finite temperature, they are continuous in our case. On the other side, where  $\mu/J \simeq 0.8$ , there appears a second order phase transition into a supersolid region that spans all the way to  $\mu/J = 0$ . Finally, we take a cut at  $\theta = -0.23$  of the LR-SR lobe. The behavior of this system seems to be quite different. The first thing to notice is that the transitions on either side of the lobe are of second order. The other, and more important, observation is that now it appears that this system has supersolid behavior on both sides of the lobe: in addition to the expected supersolid at smaller  $\mu/J$ , a region at  $\mu/J$  above the crystal lobe appears where both structure factor and superfluid fraction are finite.

If we recall Fig. 3.6, right panel, the LR-LR system showed that at  $\theta = -0.15$  as  $L$  increased the supersolid region disappeared from the upper side of the lobe. In the case of the LR-SR system for  $\theta = -0.23$  the increase in the system size does not get rid of this supersolid phase.

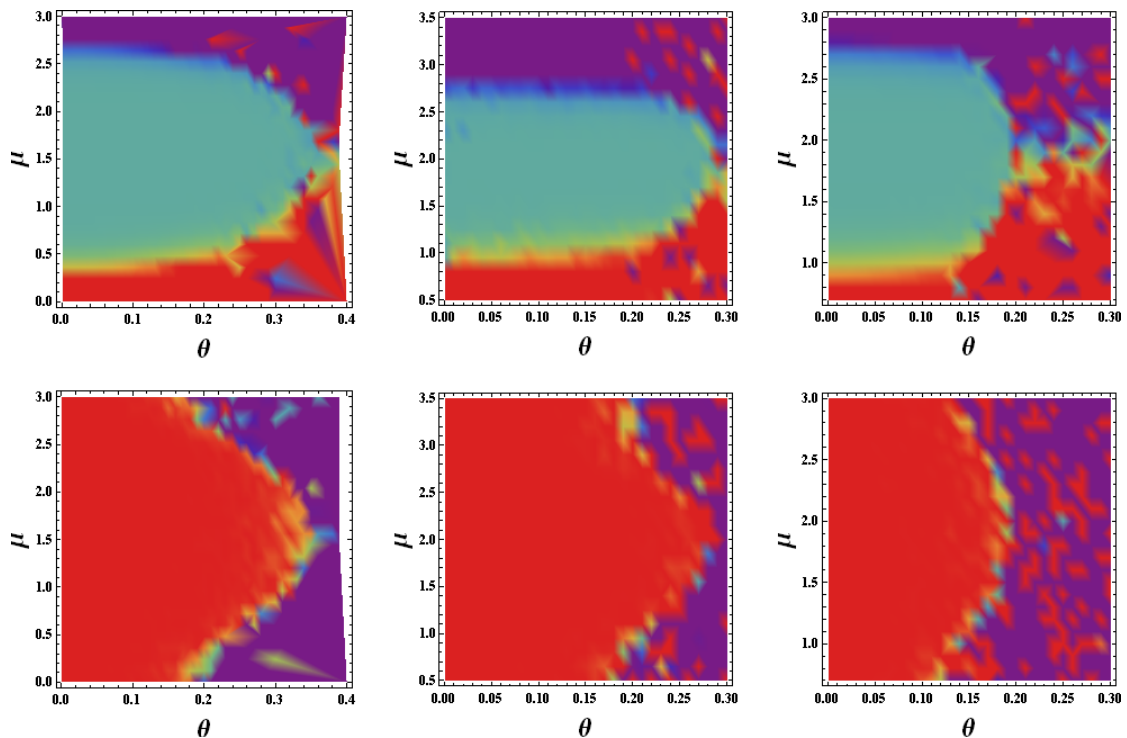


FIGURE 3.8: The columns show the  $\rho = 2/3$  lobes for simulation that had the sign problem ( $\theta > 0$ ), evidenced by particle density (top row) and the superfluid fraction (bottom row) that arise under varying the ratio,  $\theta$ , and the chemical potential,  $\mu/J$  (data for  $L = 6$ ). The left column corresponds to the SR-SR system, the middle one shows the LR-SR system and the right column depicts the lobes for the LR-LR system.

Now we turn our attention shortly to the parameters where the sign problem exists or where  $\theta > 0$ . As we have discussed earlier, the sign problem comes from the appearance of negative probabilities in the partition function. This causes certain parameters to give non-physical results and huge errors. Here we will examine the region where the sign problem exists and determine where the QMC code is reliable and where it fails. So again examine the  $2/3$  filling lobes with the all the same interactions. Fig. 3.8 shows the results in a similar manner as were presented in Fig. 3.4 however this time the sign of  $\theta$  is positive. (The figure is shown as a 2D plot instead of a 3D plot due to the fact that there are many unreliable points that fluctuate drastically and a three dimensional representation of it is almost

completely unintelligible.) We can see that the lobes are now facing in the opposite direction similarly to the areas encompassed by the dark blue lines of Fig. 3.1 when the one dimensional case was studied. If we compare the two situation,  $\theta < 0$  and  $\theta > 0$ , we see that the general shapes of the lobes are quite similar. It is however very difficult to tell precisely how the lobes differ. The instability and error caused by the sign problem becomes more and more noticeable as the parameters reach the areas where the phase transitions occur. Since this is the section that is supposed to be the most interesting and give us the most information, these graphs provided no definitive evidence that could help in determining the behaviors of the lobes. The best we can say is that the behavior is similar the the lobes where  $\theta$  is negative but we cannot make any accurate conclusions about which phases appear in which areas for the  $\theta > 0$  regime.

### 3.3.3 Finite temperature results

As a final calculation, we take a look at the important role that the temperature plays in both the melting of the crystal as well as the supersolid region. In this section, we will use the same cuts as in the previous section ( $\theta = -0.28$  for SR-SR,  $\theta = -0.23$  for LR-SR and  $\theta = -0.15$  for LR-LR) so that each system will posses all the possible phases: crystal, superfluid, and supersolid. Each cut is investigated for  $0.05 < T < 0.3$  at a system size of  $L = 6$ . First, we analyze the structure factor to study how the  $\rho = 2/3$  crystal melts with an increase in temperature (second row of Fig. 3.9). For the SR-SR interactions, even at a temperature of 0.3 there still exists a bump in the structure factor which indicates that the crystal has not completely melted yet, while for both of the long-ranged lobes the crystal melts by  $T \simeq 0.3$ . Interestingly, the SR-SR crystal and the LR-LR crystal are approximately the same size at  $T = 0.05$ , but by  $T = 0.3$  one has melted while the other still exists. That means that the system with short-ranged interactions holds its crystal structure better at higher temperatures than does our system with all long-ranged interactions. Looking at the LR-SR lobe, we see that its crystal at this cut starts off smaller, yet it melts at about the same temperature as the

one for LR-LR interactions. It seems that the dipolar repulsion helps stabilize the crystal structure over a larger temperature range, while the long-ranged hopping destroys the crystal more quickly because of the extra kinetic energy.

Maybe more importantly, we now study the melting of the supersolid for these same cuts. Figure 3.9 shows the structure factor, superfluidity, and supersolidity as a function of temperature for each of the different systems. Since the supersolid is defined by having both non-zero structure factor and non-zero superfluid fraction, by combining the graphs we are able to see where these regions exist and also how they melt with increased temperature (the bottom row of Fig. 3.9 shows a product of structure factor and superfluid fraction, which remains finite only where the two coexist). A common feature of all the graphs are the spikes on either

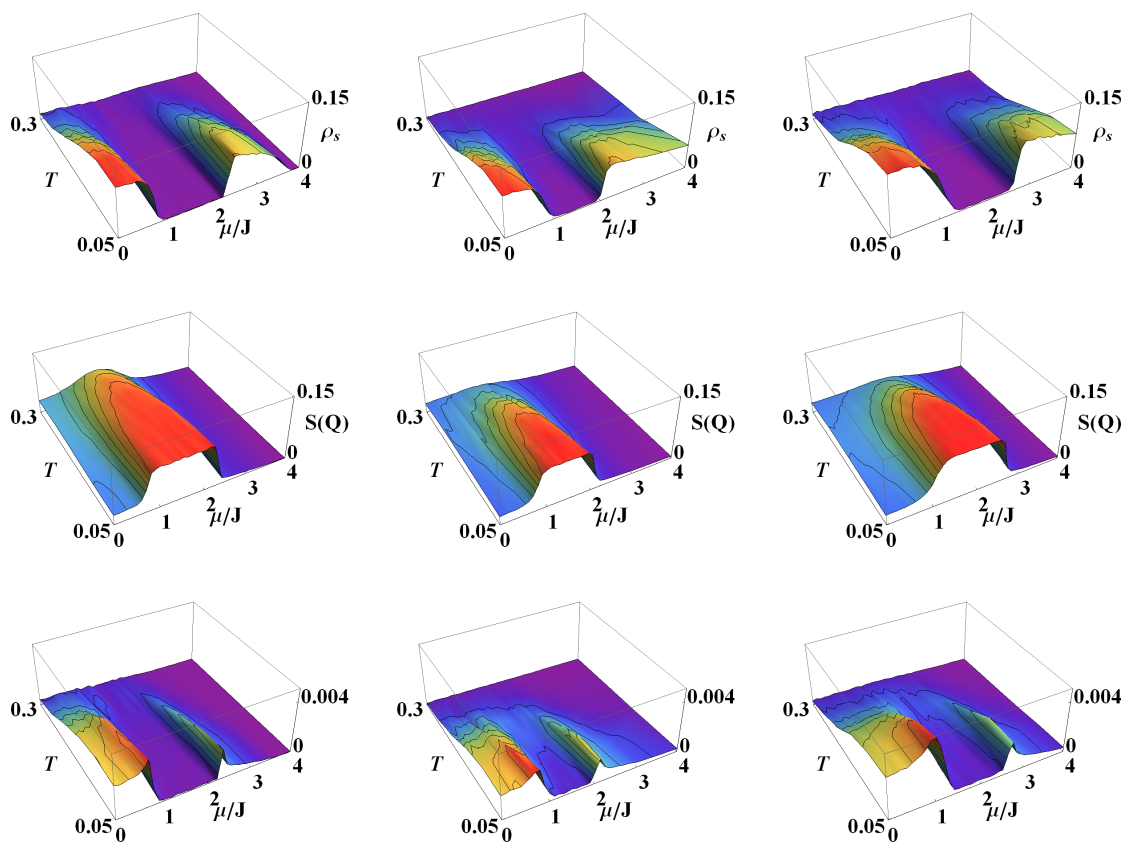


FIGURE 3.9: Each row shows a different object : the top row - the stiffness, the middle row — the structure factor while the bottom row represents a product of the first two rows. Columns corresponds to different systems: Left column is for SR-SR at  $\theta = -0.28$ , middle column yields LR-SR at  $\theta = -0.23$ , right column is for LR-LR at  $\theta = -0.15$ . For all three systems, the three distinct quantum phases — crystal, supersolid, and superfluid - survive over some temperature range before they melt.

side of the plateaus. These are regions where a phase transition occurs but does not necessarily imply that a supersolid region exists. Most likely, these features appear due to the finite size of the system and the resulting smooth transitions of superfluid fraction and structure factor. At larger sizes, the transitions would be much sharper at these points, the regions where a finite structure factor and superfluid fraction coexist would shrink, and the spikes would diminish. From the previous section, we can assume that for the SR-SR system they would disappear completely at the upper transition from the crystal lobe while for the other two systems there would still exist a small supersolid region.

Returning to the main focus, the small- $\mu$  region, we see that in each case a supersolid region appears that extends from the left side of the plateau all the way to  $\mu/J = 0$ . In every system, this supersolid region also exists for a finite range of temperatures. For SR-SR interactions, it gradually decreases but still extends all the way out past  $T = 0.3$ . For the LR-SR interactions, the supersolid region again slowly melts but now disappears at  $T \simeq 0.23$ , just below the spot where the crystal melted. The supersolid region for the LR-LR system appears to have the largest magnitude of the three systems, but then rapidly melts at  $T \simeq 0.3$ .

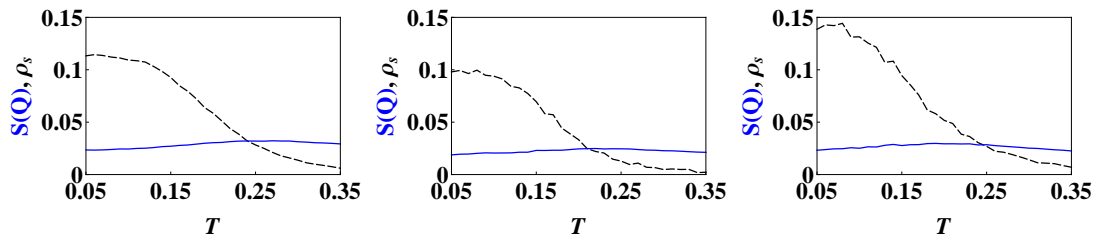


FIGURE 3.10: SR-SR at  $\theta = -0.28$ , LR-SR at  $\theta = -0.23$  and LR-LR at  $\theta = -0.15$  (left to right). All cuts are taken at  $\mu/J = 0$ . The structure factor (solid blue) attains similar values for all three systems. The superfluid fraction (dashed black) is largest in the LR-LR system and melts fastest in the LR-SR one.

In order to compare these transitions more quantitatively, we take a cut along  $\mu/J = 0$  for each system, shown in Fig. 3.10. All three systems show a relatively similar and steady value for the structure factor. Hence, the values of the superfluid fraction are going to determine the existence of the supersolid regions. The first plot shows the SR-SR system at the  $\theta = -0.28$  cut, and we can see that the

superfluid fraction stays non-zero all the way out to  $T = 0.35$ . The LR-SR system has a very similar behavior at the  $\theta = -0.23$  cut, but in this case the supersolid is nearly completely melted by  $T = 0.35$ . The final plot is the LR-LR system at  $\theta = -0.15$ , which behaves slightly differently. The most important difference is that the starting value of the superfluid fraction is higher than in the first two plots. This should therefore make the supersolid region more pronounced. But even though the superfluid fraction has the highest value for this system, it decays more quickly and reaches values similar to the SR-SR system at  $T \approx 0.35$ .

### 3.4 Conclusion

In this chapter, we have presented a quantum Monte Carlo study of dipolar spin models that describe various systems of ultra-cold atoms, molecules, and ions. We have presented predictions concerning the phase diagram of the considered systems at zero and finite temperatures, and described the appearance and some properties of the superfluid, supersolid, and crystalline phases. While the results are not surprising and resemble earlier obtained results for similar systems in 1D and 2D, the main advantage of our study is that it is directly relevant to the current experiments. We also studied the effects of the sign problem that arose for certain sets of parameters. The only thing that could be determined was that deep within the Mott state the solutions were acceptable but near the edges the code broke down and provided unusable answers.

# Chapter 4

## Density dependent tunneling in the extended Bose-Hubbard model

### 4.1 Introduction

In the last decade, the physics of ultra-cold atoms in optical lattice potentials has undergone extensive developments due to the extreme Controllability and versatility of the realizable many-body systems (for recent reviews see [61, 62]). The tight-binding description predicted in 1998 [8], termed Bose-Hubbard model (BHM) for bosonic atoms with contact  $s$ -wave interactions, was soon after verified via the experimental observation of the superfluid (SF) - Mott insulator (MI) transition [7]. For particles interacting via a long-range (e.g., dipole-dipole) potential, the original model has to be modified, typically including a density-density interaction between different sites. The simplest approximation, taking into account only the interaction between nearest neighbors, is termed the extended Bose-Hubbard model (EBHM). As compared to the BHM, the extended model allows for the existence of novel quantum phases such as checkerboard solids, supersolid phases [41–43, 56–58], exotic Haldane insulators [23] and more.

Recently, however, it has been realized that even in the simpler case of contact  $s$ -wave interactions, in certain parameter regimes, carefully performed tight-binding approximations lead to an additional correlated tunneling term in the resulting microscopic description. This term, known in the case of fermions as bond-charge contribution [63], is even more important for bosons [64–67]. It is found that such tunneling terms along with the effect of higher bands can provide an explanation [65, 68] of the unexpected shift in the MI-SF transition point for Bose-Fermi [69, 70] and Bose-Bose mixtures [71] as well as shifts in absorption spectra for bosons in optical lattices [66].

One may expect that similar bond-charge (or density-dependent tunneling) effects may also play an important role in the presence of dipolar interactions. This assumption has been verified in [17] in a recent study, where it has been shown that the additional terms in the Hamiltonian may destroy some insulating phases and can create novel pair-superfluid states. That study [17] has been restricted to a one-dimensional (1D) model due to the numerical methods used. Here, we use Quantum Monte Carlo (QMC) methods to study soft-core dipolar gases trapped in two-dimensional square optical lattices, where we assume a tight confinement in the remaining  $z$  direction (which is also the polarization direction of the dipoles). A similar two-dimensional model without density-dependent tunneling terms was analyzed before [42], providing us with a benchmark against which we may test the importance of density-dependent tunneling. In Ref. [42], a supersolid phase was observed in the EBHM just above half filling. Such a supersolid is characterized by the coexistence of superfluid and crystal-like density-density diagonal long-range order [41–43, 56–58]. Experimental evidence of this counter-intuitive quantum phase is still missing, since the claim of an experimental realization of supersolidity in  $^4\text{He}$  [72, 73] could not be reproduced in later experiments [74, 75]. As we shall see, in the present model, the sign of the additional tunneling (or, more precisely, the relative sign between the standard tunneling and the density-dependent one) can stabilize or destabilize the supersolid phase.

## 4.2 The model

The appropriate tight-binding model to study interacting dipolar bosons occupying the lowest band in a lattice reads [17]

$$\begin{aligned}
 H = & -J \sum_{\langle i,j \rangle} (b_i^\dagger b_j + \text{h.c.}) + \frac{U}{2} \sum_i n_i(n_i - 1) - \mu \sum_i n_i + \sum_{i,j} V_{i,j} n_i n_j \\
 & - \sum_{i,j} T_{i,j} (b_i^\dagger (n_i + n_j) b_j + \text{h.c.}) + \sum_{i,j} P_{i,j} (b_i^\dagger b_i^\dagger b_j b_j + \text{h.c.}), \quad (4.1)
 \end{aligned}$$

where  $b_i^\dagger$  ( $b_i$ ) is the creation (annihilation) operator of a boson at site  $i$  and  $n_i$  is the number operator;  $J$  is the regular hopping term,  $U$  the on-site repulsion and  $\mu$  the chemical potential. We assume a system of dipolar bosons in a 2D square lattice with dipolar moments polarized perpendicularly to the lattice, thus leading to dipole-dipole repulsion. Then, the present model contains three terms that come from the dipolar interactions, the nearest-neighbor repulsion  $V$ , the density-dependent hopping  $T$  and the correlated pair tunneling  $P$ . We restrict here the range of  $V$  to the nearest neighbors to allow for a direct comparison with the results of Ref. [42] and [17]. Within the standard EBHM, both the  $T$  and  $P$  terms are neglected. However, the analysis presented in Ref. [17] has shown that, although  $V$  is typically an order of magnitude larger than both  $T$  and  $P$ , the latter terms cannot be neglected in the presence of strong dipolar interactions.

The four parameters  $U$ ,  $V$ ,  $T$  and  $P$  have the same physical origin, namely interactions and are therefore correlated. However, in the two-dimensional model, changing the trapping frequency in the direction perpendicular to the plane affects quite strongly only the on-site  $U$  term (for dipolar as well as for the contact part of the interactions). Thus, we shall consider  $U$  as an independent parameter. To facilitate a comparison with earlier works (e.g., [42]) that did not take  $T$  tunneling into account we span a similar parameter range for  $U$ ,  $V$  and filling fractions. The values of  $T$ ,  $V$  and  $P$  are strongly correlated as they originate from nearest-neighbor scattering due to long-range interactions. For a broad range of optical lattice depths, the parameters  $T$  and  $V$  are typically related as  $V \approx |10T|$ .

The absolute value of  $P$  is almost another magnitude smaller than  $T$  (compare Fig. 1 of [17]). Thus, for simplicity, we will set  $V = |10T|$  in the following and neglect the  $P$  term altogether. This will allow us to study in depth the effects due to density-dependent tunnelings. The previous study [17] has shown that there is a broad tunability regarding the relationship of the two tunneling parameters  $T$  and  $J$ , allowing a regime where the two hopping terms have opposite signs and even the exotic situation that  $T$  dominates over  $J$ . For example, for weak trapping frequency along the polarization direction,  $J$  and  $T$  have opposite sign and for strong trapping frequency  $J$  and  $T$  have same sign. Thus, for possible experimental realizations of polar bosons [76, 77], one can reach the two limits of bond-charge tunneling by tuning the trapping potential along the polarization direction [17].

Whether both hopping terms are of the same or of opposite sign has a major influence on the phases that will appear in the system. Generally speaking, when both hopping terms have the same sign, one can expect an increase of the influence of the overall hopping. Otherwise, if the signs are opposite, there will be a competition between the two terms. Therefore, the influence of the additional density-dependent hopping can be expected to strongly affect the phase diagram.

To form an intuition about our system, let us give a brief summary of the results from the previous study [17] of a similar 1D system with both a density-dependent and a pair-hopping term. In that study, exact diagonalization (system sizes between  $L = 8$  and  $L = 16$ ) and the Multiscale Entanglement Renormalization Ansatz (MERA) (system sizes up to  $L = 128$ ) were used to study the phase diagram at zero temperature. The results, when both  $T$  and  $P$  are set to zero, show the existence of three phases. At weak interaction, there is a superfluid phase (SF), while at stronger dipolar strength, two charge density wave (CDW) phases appear. The CDW phases are characterized by a periodic, crystal-like structure where occupied and empty sites alternate in a checkerboard pattern. In the following, we denote cases where the populated sites are occupied by a single atom (two atoms) as CDW I (II). In the one-dimensional case of Ref. [17], the two observed CDW phases are a CDW I phase at half filling with a modulation of  $|\dots 010101\dots\rangle$

and a CDW II phase at unit filling with a modulation of  $|\dots 020202\dots\rangle$ . Now, when the extra terms  $T$  and  $P$  are incorporated into the Hamiltonian, besides an overall deformation of the phase diagram, there appears also a novel pair-superfluid phase (PSF). This more exotic phase is characterized by a finite two-particle NN correlation function  $\Phi_i = \sum_{\{j\}} \langle b_j^\dagger b_j^\dagger b_i b_i \rangle$  and a smaller non-vanishing one-particle correlation function  $\phi_i = \sum_{\{j\}} \langle b_j^\dagger b_i \rangle$ . On the other hand, no supersolid phase has been observed in [17]. In the present study of a 2D lattice, on the contrary, we do observe a supersolid behavior, but we do not find any indications for the existence of a PSF phase.

### 4.2.1 Considered observables

In the analysis of Hamiltonian (4.1), we employ the Stochastic Series Expansion (SSE) code, a QMC algorithm from the ALPS (Algorithms and Libraries for Physics Simulations) project [21]. We mainly rely on three observables. First, we study the density,  $\rho = \langle n_i \rangle$ , as a function of the chemical potential. Plateaus in the corresponding graphs indicate insulating phases, such as MI or CDW phases. The employed variant of QMC works in the grand-canonical ensemble, i.e., at fixed chemical potential. Discontinuous jumps in the density as a function of chemical potential signify regions of phase separation (PS) in the canonical phase diagrams. Namely, when the filling is fixed to a value which is not stable at any chemical potential, the system acquires the required filling only in the mean, by forming domain walls between two phases that are thermodynamically stable.

To distinguish not only different insulating phases (MI, CDW I and CDW II), but also the superfluid (SF) and the supersolid phase (SS), we consider two other observables. These are the structure factor and the superfluid stiffness, which we analyze both as a function of density. The structure factor is defined as

$$S(\mathbf{Q}) = \left\langle \left| \sum_{i=1}^N n_i e^{i\mathbf{Q}\mathbf{r}_i} \right|^2 \right\rangle / N^2. \quad (4.2)$$

Here,  $N$  denotes the number of lattice sites and we focus on the wave vector  $\mathbf{Q} = (\pi, \pi)$ , which corresponds to a checkerboard modulation pattern. This observable has a peak when the particles are arranged in either of the CDW phases. This will help to distinguish the MI phase from the CDW phase, which cannot be done from the density graphs alone. For example, when a system is at unit filling, the structure factor is finite in the CDW II state, whereas it vanishes in the usual MI state.

The other observable is the superfluid stiffness, which can be calculated from the winding numbers of the QMC code. It is defined as

$$\rho_s = \frac{\langle W^2 \rangle}{4\beta}, \quad (4.3)$$

where as we recall  $W$  is the winding-number fluctuation of the world lines and  $\beta$  is the inverse temperature (in this study  $\beta = 20$ ). This value shows what percent of the system is in a superfluid state. Taking superfluid stiffness and structure factor together, we can also identify the SS phase. The SS phase occurs when both superfluid stiffness and structure factor are non-zero. Note that, since PS regions do not correspond to stable grand-canonical phases as computed in the SSE QMC code, we cannot assign any values of observables for them. This is not necessary, however, since PS regions are already unambiguously identified by jumps in plots of density against chemical potential.

From these three observables (density, structure factor and superfluid stiffness) we are now able to distinguish the most prominent phases that we are looking for. These observables cannot, however, identify PSF phases, the signature of which is, as mentioned previously, a non-vanishing two-particle NN correlation function  $\Phi_i$ . In its current version, the QMC code provided in the ALPS library is not able to calculate these correlation functions. In order to extract this observable, the code would have to be written with a two-headed worm, which could then be analyzed in a similar way as the superfluid stiffness, but with the difference that the winding numbers would represent the flowing of pairs instead of single particles [78]. Fortunately, one can identify a dominant PSF order parameter

using a different technique, namely by studying the density histograms of the QMC code. If these histograms show only even values of particles instead of a uniform distribution, this means that the bosons always pair up, indicating PSF behavior [78].

### 4.3 Ground-state phase diagrams

In this section, we present our QMC results for the ground-state phase diagram of Hamiltonian (4.1). We focus on a two-dimensional square lattice with linear system sizes ranging from  $L = 8$  to  $L = 16$  (where  $N = L \times L$ ). We observe a fast convergence of the results with  $L$ , similarly to [42]. Therefore, the considered system sizes suffice, especially since we are interested not in the precise determination of phase boundaries, but in the global qualitative changes in the phase diagrams, which — as we will see — can be quite drastic. We present phase diagrams at two different values of the on-site repulsion ( $U = 20$  and  $U = 5$ ) for varying density and  $T$  (and therefore for varying  $V$ , since  $V = 10|T|$ ). The two  $U$  values are chosen in such a way that we can compare nearly hard-core like behavior, achieved at  $U = 20$ , with soft-core behavior, for  $U = 5$ . Up to 4 bosons are allowed per site for both cases, which seems sufficient for densities below unit filling (we tested in some instances against maximal occupation of 6 bosons per site). Further, at  $U = 20$  we can compare our data to known results of the usual EBHM, which was studied thoroughly in [42]. We compare phase diagrams obtained with and without density-dependent tunnelings. For simplicity and ease of comparison to [42], we restrict our study to unit filling or less. Furthermore, for a more detailed evaluation of these phase diagrams, we study a few cuts at representative parameter values.

### 4.3.1 Phase diagrams at vanishing density-dependent tunneling

We begin our analysis with phase diagrams of the regular EBHM, illustrated in Fig. 4.1. This provides an overview of the behavior of the considered systems under a more common Hamiltonian, which does not have a density-dependent term  $T$ . We consider the case of strong repulsion  $U = 20$ , discussed previously in [42], as well as softer interacting bosons with  $U = 5$ .

#### 4.3.1.1 Phase diagram at strong on-site repulsion ( $U = 20$ )

For ease of comparison and for later reference, Fig. 4.1a reproduces the phase diagram of  $U = 20$  that has been thoroughly investigated in [42]. It is well known that for  $\rho < \frac{1}{2}$  there exist only two distinct regions, the SF phase and a PS region. For sufficiently low values of  $V$ , the system stays superfluid across the entire density range until unit filling, where it becomes a MI state. At half

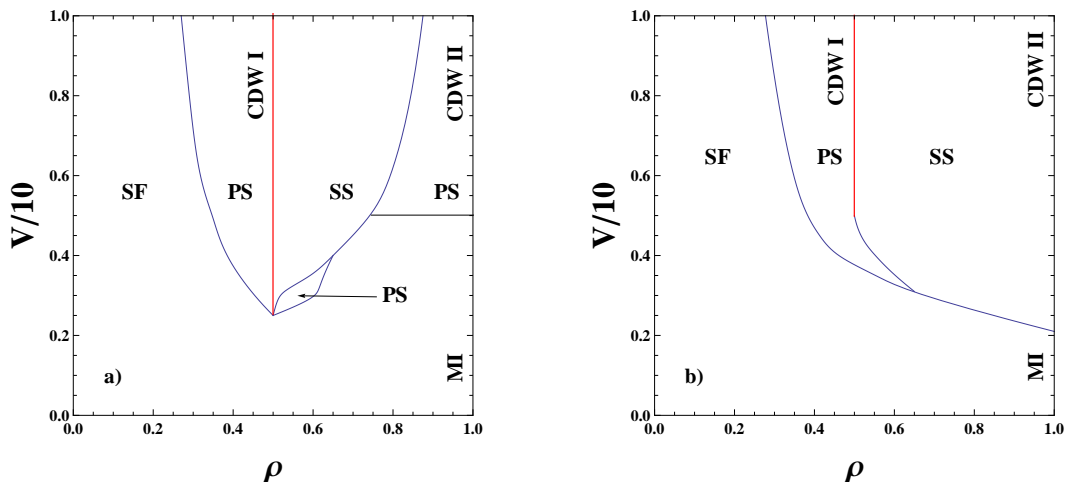


FIGURE 4.1: The phase diagram in the  $\rho - V$  parameter space without density-dependent tunneling term,  $T = 0$ , for (a)  $U = 20$  and (b)  $U = 5$ . The energy unit is  $t = 1$ . Panel a) reproduces the results of [42]. The model contains various phases. The red solid line indicates the charge density wave (CDW I) at half filling; other phases present are the superfluid (SF), supersolid (SS) and at unit filling either Mott insulator (MI) or another charge density wave (CDW II); PS denotes phase separated regions. When the on-site interaction becomes weaker, as shown in panel b), the SS phase becomes larger and PS regions disappear at filling larger than  $1/2$ .

filling, a CDW I phase appears at a critical value of  $V$ , which in the present case lies around  $V = 2.5$ . A system in a checkerboard phase (CDW I) can be doped by holes or particles. When it is doped with holes, these create domain walls and cause the system to phase separate, preventing the appearance of a SS phase. In the case of hardcore bosons, this behavior would be mirrored for  $\rho > \frac{1}{2}$ , due to particle-hole symmetry. In the case of soft-core bosons, such particle-hole symmetry can break down. At sufficiently low  $V$ , a region of PS appears and the system does present a hardcore-like behavior, but as the NN repulsion is increased this PS region disappears. Since now the particles can occupy either an empty or occupied site, it is no longer necessary for the domain walls to form and the system can move into a SS state. Moreover, at a certain value of  $V$ , upon increasing  $\rho$  the SS phase is followed by a region of PS, instead of going into a SF phase and then becoming a MI. At unit filling, this PS region then changes to the CDW II phase, which is characterized by a checkerboard pattern consisting of an alternation of doubly-filled sites and empty ones.

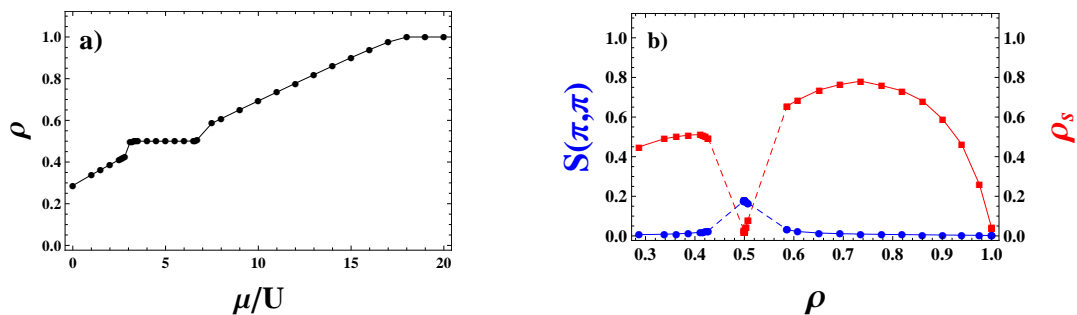


FIGURE 4.2: Identification of different phases as exemplified for  $U = 20$  and  $V = 3.0$  based on the density in (a) as well as the structure factor (blue circles) and the superfluid stiffness (red squares) shown versus density in (b). Plateaus in  $\rho$  as a function of  $\mu$  indicate incompressible crystal phases. Jumps denote phase separation (the densities that are jumped over do not correspond to thermodynamically stable phases). Moreover, a finite superfluid stiffness characterizes a SF phase and a finite structure factor a CDW order. When both are finite, the system is SS.

Figure 4.2 shows, for a fixed  $V = 3$ , the observables described in Section 4.2.1 that we used to determine the various phases. The boson density as a function of the chemical potential displays clear plateaus, corresponding to gapped insulating phases, Fig. 4.2 (a). As mentioned above, jumps in Fig. 4.2 (a) correspond to PS regions in Fig. 4.1. The structure factor and the superfluid stiffness are shown

in Fig. 4.2 (b). For low chemical potential (density) the system is in a SF state with non-zero superfluid stiffness and vanishing structure factor. At  $\rho \approx 0.43$ , the system phase separates and there are no values for these observables. At half filling, when the system moves to CDW I phase, the structure factor becomes finite. There is a small region, roughly around  $0.5 < \rho < 0.51$ , where the system is in a SS phase — here both the superfluid stiffness and the structure factor are non-zero. This phase is followed by a second region of PS that extends up to  $\rho \approx 0.61$ . At higher densities, a SF phase is observed up to unit filling, where a MI state follows, as revealed by vanishing superfluid density and structure factor.

#### 4.3.1.2 Phase diagram at moderate on-site repulsion ( $U = 5$ )

We now consider  $U = 5$ , a case of weaker repulsion that has not been studied earlier. For the moment, we still retain  $T = 0$ . The phase diagram Fig. 4.1b seems a bit simpler than for  $U = 20$ . Importantly, the particle-doped side now has to deal with much "softer" bosons allowing for multiple occupancy on any given site (in the numerical calculations we allow for up to 4 bosons per site which is sufficient for lattice fillings below unity) The hole-doped side is much less affected since the on-site repulsion has a lesser influence on lower densities. For weak NN repulsion  $V$ , the system stays SF across the entire range of densities from empty to unit filling and then goes into the MI state. At  $V \approx 2.3$  up to  $V \approx 3.1$ , the system goes directly from a SF phase into a SS phase, which ends at a CDW II phase at unit filling. At larger  $V$ , a PS region appears. The biggest difference between  $U = 20$  and  $U = 5$  cases appears for higher values of  $V$ , where the PS region at the particle-doped side disappears and the SS phase occupies the entire region between the CDW I at half filling and the CDW II at unit filling.

The different transitions are revealed by slices through the phase diagram at fixed  $V$  (exemplified for a few values in Fig. 4.3). At  $V = 3.0$ , the density is strictly increasing across the entire range of  $\mu$ , Fig. 4.3 (a). Notice, however, a change of the slope around  $\mu/U = 4$ , corresponding to  $\rho = 0.6$ . As seen in Fig. 4.3 (d), the structure factor starts to rise in a similar parameter range, namely around

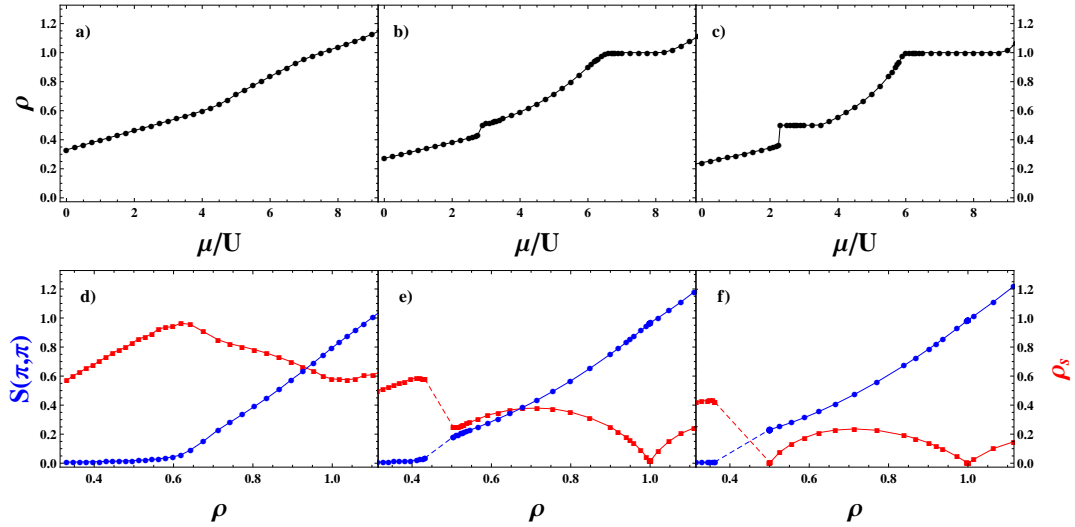


FIGURE 4.3: Top row: density versus chemical potential for  $U = 5$  and different values of  $V$ :  $V = 3.0$ ,  $V = 4.5$  and  $V = 6.0$  (left to right). The bottom row shows the corresponding structure factor (blue circles) and the superfluid stiffness (red squares).

$\rho = 0.65$ . At the same time, the superfluid stiffness only has a peak at  $\rho = 0.65$ , but remains finite for all values of  $\mu$  considered. Therefore, the increase of the structure factor is a clear sign of a second-order transition from a SF to a SS. Also, since the structure factor does not drop back to zero at  $\rho = 1$ , the unit filling phase will be a CDW II and not a MI.

The next slice is taken at  $V = 4.5$ , where the state changes from SF to PS to SS without ever settling into the CDW I phase at half filling. In the density graph, Fig. 4.3 (b), we can see a small jump that bypasses  $\rho = \frac{1}{2}$ . This explains why the CDW I phase does not appear at this value of  $V$ . The SF at small  $\rho$  is identified by a non-zero superfluid fraction and vanishing structure factor, Fig. 4.3 (e). This phase is followed by the PS region from  $\rho \approx 0.435$  to  $\rho \approx 0.51$ . At higher densities, a SS state appears as characterized by non-zero structure factor and superfluid stiffness. Finally, the system settles into the CDW II state at unit filling.

The last slice at  $V = 6.0$  is similar to the previous one at  $V = 4.5$  with one major difference, the appearance of the CDW I phase at half filling. As before, we can see a jump (this time slightly larger) in the density, Fig. 4.3c, but now it is followed by a plateau that signifies the CDW I phase. In Fig. 4.3f, we see again the three

distinct phases, SF up to  $\rho \approx 0.35$ , then a region of PS up to  $\rho = 0.5$  and from half filling to unit filling there is the SS phase, once again ending in the CDW II state.

### 4.3.2 Phase diagrams at finite density-dependent tunneling

As we have seen in the previous section, the phase diagram of the EBHM at vanishing  $T$  displays a large variety of phases: MI, CDW, SF and SS. Additionally, there are various regions of phase separation, some of which (the ones at filling larger than  $1/2$ ) disappear with decreasing on-site repulsion of the bosons. In this section, we study how this phase diagram of the usual EBHM is changed by the density-dependent hopping.

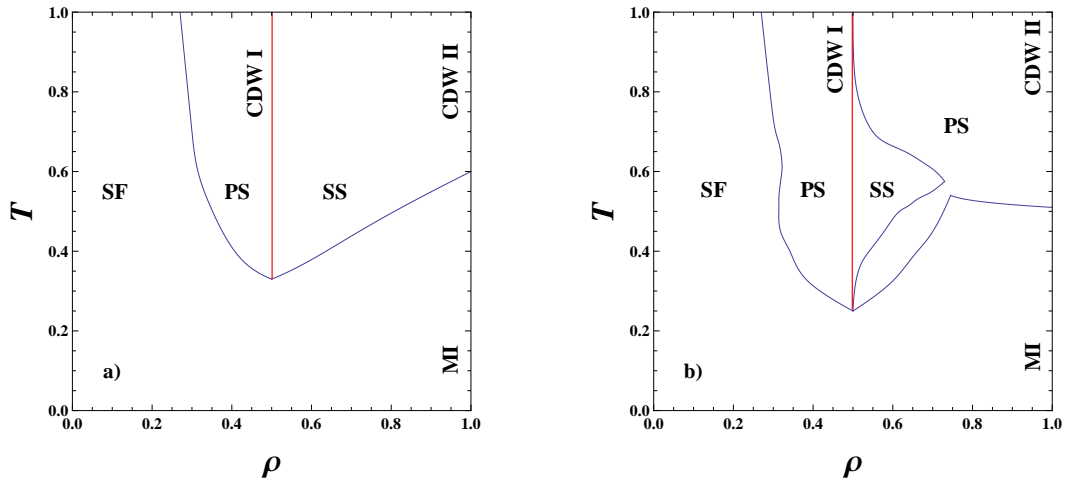


FIGURE 4.4: The phase diagrams for  $U = 20$  at finite  $T$  (with  $V = 10|T|$  and  $t = 1$  the unit of energy). (a) If  $J$  and  $T$  are of the same sign, the relative importance of interactions decreases, leading to the disappearance of PS phases at greater than half filling. Compared to the  $T = 0$  cases presented in Fig. 4.1, this phase diagram resembles more the case  $U = 5$  than  $U = 20$ . (b) If  $T$  and  $J$  compete due to opposite signs, the relative importance of interactions is enhanced, increasing the PS regions. In fact the two separate regions of PS in Fig. 4.1b increase to the point of overlapping.

### 4.3.2.1 Phase diagram at strong on-site repulsion

The first case we study is  $U = 20$  when the two tunneling amplitudes  $J$  and  $T$  have the same sign. Comparison of Fig. 4.4 with Fig. 4.2 shows that in the presence of density-dependent tunneling the PS region at low  $V$  values has disappeared and there is no PS region between the SS and CDW II phases. One can explain this behavior by the increase in the total hopping due to the additional tunneling term  $T$ . Thus, the on-site repulsion  $U$  behaves as if it were effectively rescaled to a smaller value. Similar arguments explain the shift of the point where the  $\rho = \frac{1}{2}$  plateau first appears and, therefore, the CDW I phase moves from  $V \approx 2.5$  (with  $T = 0$ , Fig. 4.2) to  $V \approx 3.5$  (Fig. 4.4). As a consequence, the phase diagram at  $U = 20$  with  $J$  and  $T$  of the same sign looks very similar to the one at  $U = 5$  with vanishing  $T$ .

The behavior in the  $U = 20$  phase diagram becomes more interesting when the two tunneling terms compete due to opposite signs,  $T < 0$ . The phase diagram is presented in Fig. 4.4 (b). The CDW I phase now starts at a lower value of  $|T|$  than in the previously discussed case. Similarly, the region of PS at the lower values of  $|T|$  (and thus  $V$ ) now becomes much larger. This shows that the system has a hardcore behavior for a larger range of parameters. Additionally, the SS region diminishes and finally disappears as  $V$  gets larger. These findings can be explained through the competition between  $J$  and  $T$ , which decreases the effective, overall tunneling strength. This decrease can alternatively be seen as an effective relative increase of the interaction parameters  $U$  and  $V$ . As a result, the hard-core behavior of the system becomes more pronounced and the PS regions become more important.

The observed phases may again be analyzed in detail via the cuts at fixed  $T$  (and therefore  $V$ ), presented in Fig. 4.5. The first slice we present is for  $T = -0.3$  ( $V = 3.0$ ). As seen in Fig. 4.5a, the plateau at half filling — a CDW I, as indicated by the finite structure factor, Fig. 4.5d — is surrounded by discontinuities in the density, thus implying regions of PS. These are surrounded by SF phases, with a MI appearing at unit filling.

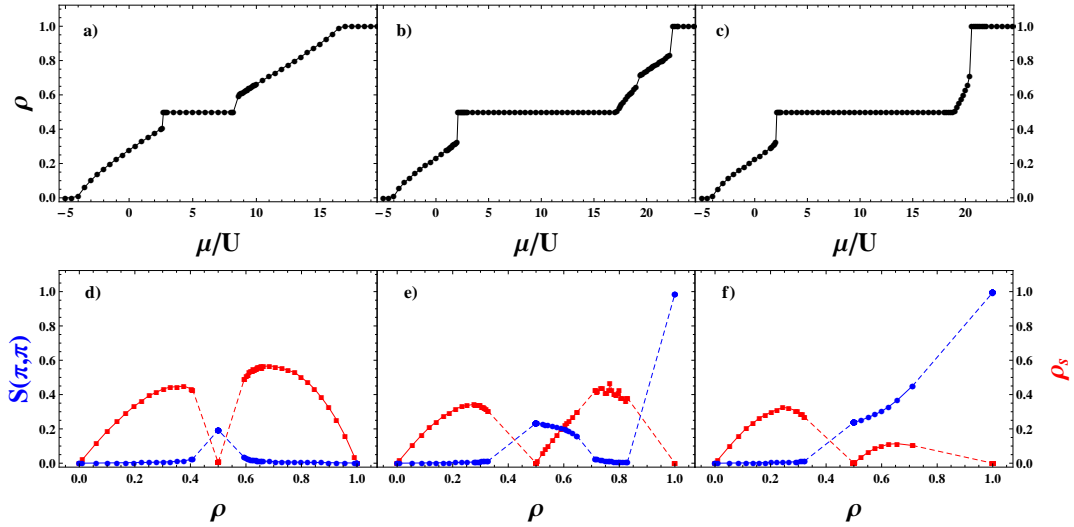


FIGURE 4.5: Density graphs of  $U = 20$  for  $T = -0.3$ ,  $T = -0.5$  and  $T = -0.6$  (left to right). Structure factor (blue circles) and superfluid stiffness (red squares) graphs for  $U = 20$  at  $T = 0.3$ ,  $T = 0.5$  and  $T = 0.6$  (left to right).

The next slice cuts through the phase diagram at  $T = -0.52$  ( $V = 5.2$ ) and this time shows also a region of the SS phase for densities just above half filling, Fig. 4.5 (e). This SS may also be observed in the density plot, Fig. 4.5 (b): Above half filling, there is a small interval of steady increase before a discontinuity occurs around  $\rho = 0.65$ . After this PS region, there is a small region where the system becomes superfluid before once again phase separating. At unit filling, the system finally transitions into a CDW II phase. Below half filling, another jump in the density indicates yet another PS.

The final cut is taken at  $T = -0.6$  ( $V = 6.0$ ). Again, at low densities the system starts in a SF phase and then jumps through a region of PS to reach the CDW I phase at half filling. For higher densities, the system first enters a SS phase and around  $\rho = 0.72$  a transition to PS occurs. This time, the system ends in the CDW II phase when unit filling is reached.

So far we have only looked at the short-ranged interactions, but we would also like to study the effects of the long-ranged ones so we extend the dipole-dipole interactions out to 3 nearest neighbors. By increasing the interactions beyond the just the nearest neighbors, we have introduced some frustration into the lattice. If we recall from the previous chapter, frustration effects make it difficult for a

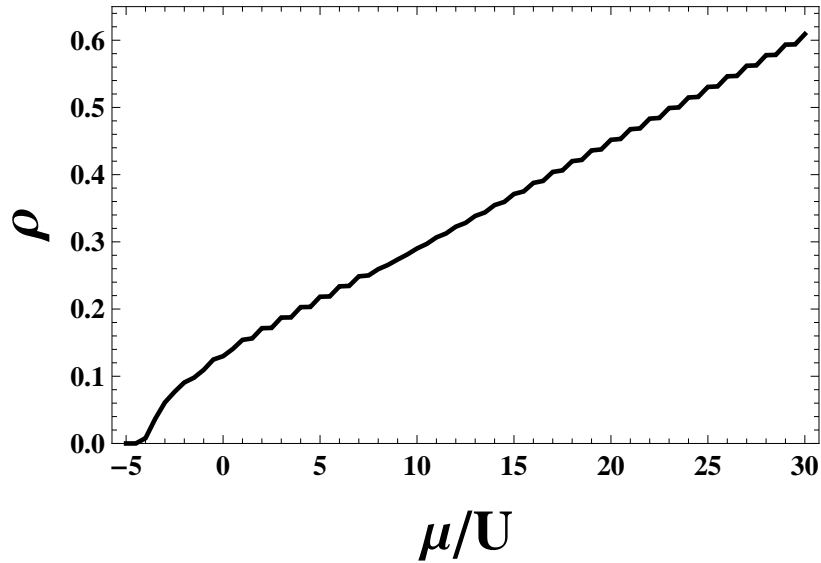


FIGURE 4.6: Density graph for  $U = 20$  and  $T = 1.0$  with long-ranged interactions.

system to settle in the true ground state and many metastable states introduce fluctuations can lead to poor results. For  $U = 20$  with the hopping parameters both having the same sign the entire phase diagram is in the superfluid state which, at full filling, transitions into a Mott insulating state. If we look at a cut out of any part of this system we see a steadily increasing density and a steadily increasing superfluid fraction while the structure factor remains nearly zero. Although the graphs of superfluid density and structure factor (not shown) have rather high fluctuations it is possible to guess how the phase diagram will look. The only interesting behavior that comes out of the long-ranged interactions can be seen at the higher values of  $T$ . Because of the increased repulsion across the lattice we begin to see a staircase like structure form in the graphs of the density. In Fig. 4.6 we have graphed the density at  $U = 20$  and  $T = 1.0$ . The increasing density seems to change in “jumps” for the range  $\mu \approx 0$  to  $\mu \approx 7$  and again for values of  $\mu > 12$ . There is only a small section in between where the density increases without exhibiting this behavior.

Next we can look at the same long-range interactions when the signs of the hopping parameters are opposite. Again, there is a large area that is completely dominated by superfluidity which then transitions to the Mott insulator phase. This time however a plateau at half filling does begin to appear just below  $T = 0.7$  and

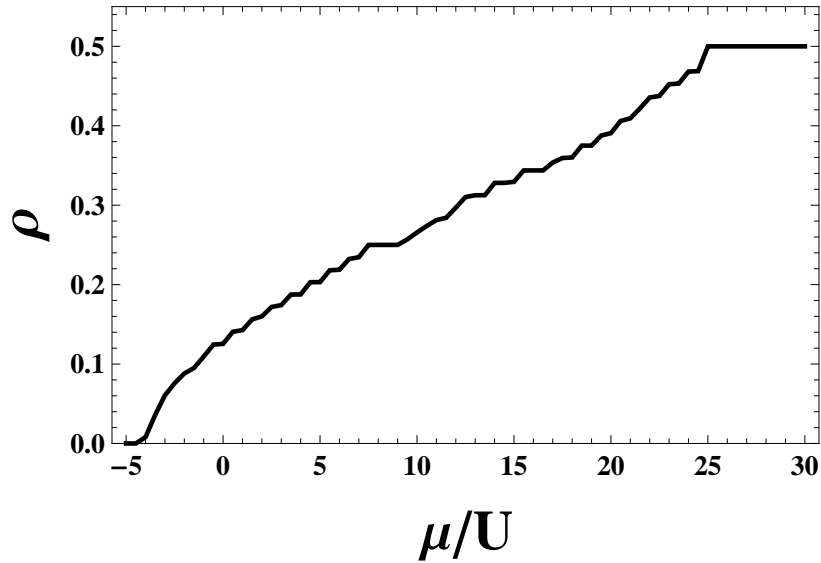


FIGURE 4.7: Density graph for  $U = 20$  and  $T = -1.0$  with long-ranged interactions.

persists as  $T$  increases (not shown). Likewise to the simulation where the signs were the same, the density graph shows a series of jumps instead of a smooth increase as we can see in Fig. 4.7. The figure shows  $U = 20$  and  $T = 1.0$  this time of course with opposite signs for the hopping parameters. This complicates the process of trying to determine any definitive states. The problem comes from the fact that each plateau is essentially an insulating state at a different filling factor. This corresponds to extreme fluctuations in the superfluidity because for any insulating section the superfluid density should be zero but in between the plateaus it should be non-zero. So the step-like density causes the superfluid fraction to have large fluctuations while the structure factor remains zero until the plateau at half filling appears. Looking once more at Fig. 4.7, we see a more prominent plateau appear at  $\rho = 0.25$ . It is difficult to say exactly what type of structure is forming there since, due to the choice of wave vectors, the structure factor does not show a peak there. A good guess is that the particles form a checkerboard-like structure where each particle is separated from the other particles by the maximum distance allowed, just like a Wigner crystal. Unfortunately due to this behavior it is quite difficult to create an accurate phase diagram so we will not attempt it.

### 4.3.2.2 Moderate on-site repulsion ( $U = 5$ )

In the previous section, we saw that the additional density-dependent tunneling term  $T$  can increase or decrease the effective importance of the interactions  $U$  and  $V$ , depending whether it competes with or supports the single-particle tunneling  $J$ . In this section, we study this effect for weaker on-site interaction  $U = 5$ . The corresponding phase diagrams are presented in Fig. 4.8.

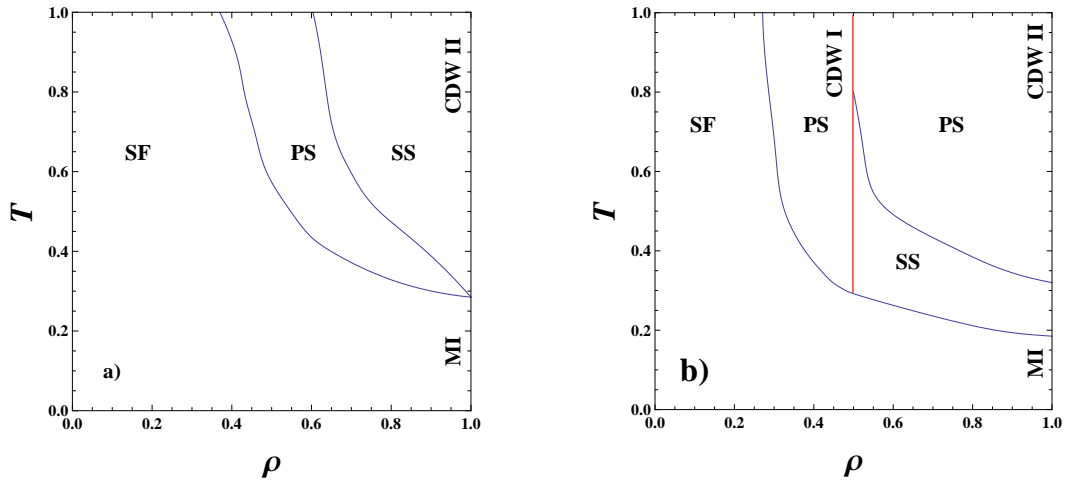


FIGURE 4.8: Phase diagrams for  $U = 5$  and finite  $T$ . (a) If  $T$  and  $J$  have the same sign, the relative strength of tunneling is strongly increased with respect to the interactions. As a consequence, the CDW I phase has disappeared completely from this phase diagram. (b) When  $T$  and  $J$  are of opposite sign, the role of interactions is enhanced, leading to increased PS regions and again the CDW I phase is present.

The positive  $T$  diagram reveals that the CDW I phase, present for  $T = 0$ , disappears completely, Fig.4.8 (a). This means that at no point does there exist a plateau in the density graphs at  $\rho = \frac{1}{2}$ . Instead, a discontinuity bypasses half filling altogether. The rest of the behavior is rather similar to the system without the density-dependent term. There are still only three phases below unit filling, i.e., the SF phase at low densities and low  $T$  (and therefore at low  $V$ ), the PS region near half filling for larger  $T$  and finally the SS phase for still higher  $T$  and larger densities. As can be expected, when the SF phase persists through the entire range of densities, the system ends in a MI state at unit filling. Instead, when the system at fixed  $T$  passes through the SS state, the final phase at unit filling is, as before, the CDW II phase.

Consider now the phase diagram of a system with  $U = 5$  when the tunneling terms have opposite signs, Fig. 4.8 (b). Here, contrary to the case of positive  $T$ , the CDW I exists at half filling. This indicates that the relative importance of the effective total tunneling is suppressed for  $T < 0$ . Moreover, now a second region of PS appears above half filling. As a result, for  $T \lesssim -0.8$  there is no stable phase with a density between the CDW I and the CDW II.

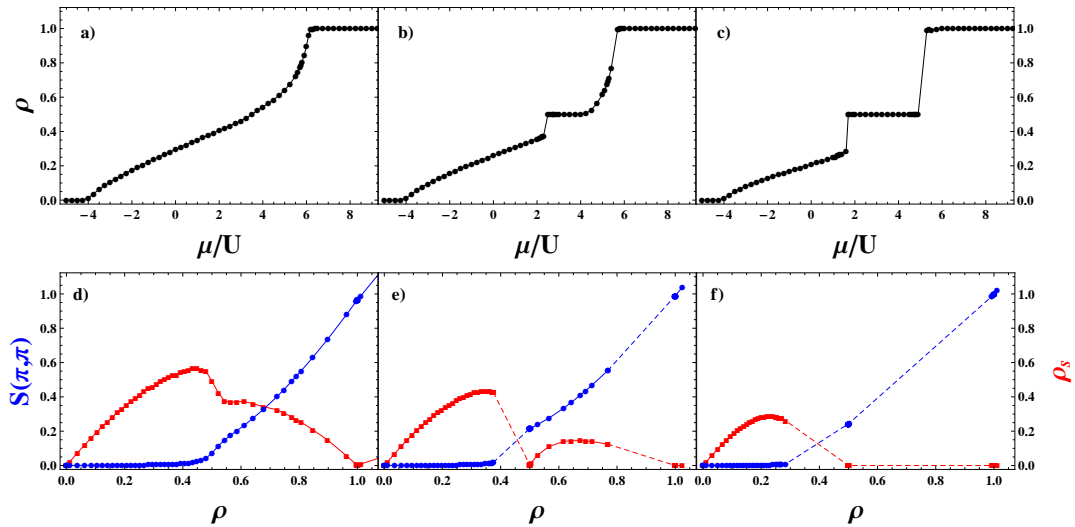


FIGURE 4.9: Top row: Density graphs for  $U = 5$  and  $T = -0.3$ ,  $T = -0.4$  and  $T = -0.8$  (left to right). The bottom row shows the structure factor (blue circles) and the superfluid stiffness (red squares) for the same parameters

These observations about the phase diagram are supported by an analysis of cuts at a few chosen values of  $T$  (and thus  $V$ ), see Fig. 4.9. At  $T = -0.3$  ( $V = 3.0$ ), one observes a smooth density increase all the way until unit filling, where a plateau appears, Fig. 4.9 (a). The structure factor starts increasing near half filling, indicating the transition from the SF to the SS phase, Fig. 4.9 (d); at unit filling, the system lands in the CDW II phase.

A cut at the slightly higher absolute value  $T = -0.4$  ( $V = 4.0$ ) reveals a plateau at half filling (CDW I) and a second one at unit filling (CDW II). Comparing the density plot, Fig. 4.9 (b), with those of superfluid stiffness and structure factor, Fig. 4.9 (e), we see that upon increasing the chemical potential the SF phase appears at low densities, followed by the PS which transitions into the CDW I at half filling. For higher densities, there is a region of SS, where both structure

factor and superfluid stiffness are non-zero. Finally, there is the jump caused by the PS region directly to the CDW II phase at unit filling.

Let us finally consider stronger density-dependent tunneling  $T$  and inter-site repulsion  $V$ , namely  $T = -0.8$  ( $V = 8.0$ ). Below half filling, the density gradually increases up to the value of  $\rho \approx 0.27$  and then jumps to the CDW I phase, Fig. 4.9 (c). After this phase, the density behaves step-like, jumping directly into the CDW II phase at  $\rho = 1$ . This behavior is seen clearly in the data presented in Fig. 4.9 (f), where the SF phase for low densities is followed by two distinct regions of PS. These regions are only interrupted by the CDW I phase at half filling and the CDW II phase at full filling.

As these results show, for the lower on-site interaction  $U = 5$ , the density-dependent term  $T$  does not change much the overall behavior of the phase diagram if it has the same sign as the single-particle tunneling  $J$ . Instead, if the two tunneling terms have opposite sign, a large part of the SS phase disappears into a phase separated region, due to the increased relative importance of the interaction terms.

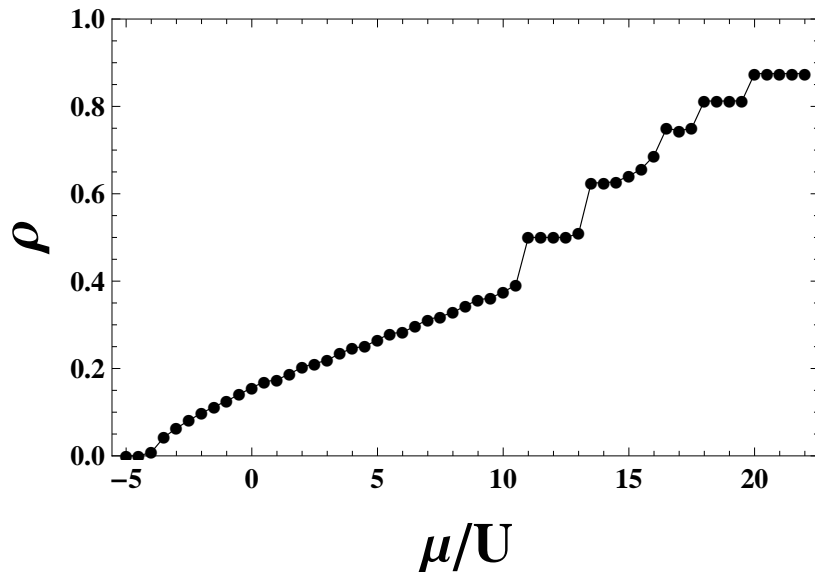


FIGURE 4.10: Density graph for  $U = 5$  and  $T = -0.6$  with long-ranged interactions.

Turning on long-ranged dipole-dipole interactions (again to 3 nearest neighbors) causes some problems for a system with such low on-site repulsion. The frustration

effects in this system are quite high and make getting any sort of phase diagram near impossible. Even with the large uncertainty of the observables we can say that for  $U = 5$  with both hopping terms having the same sign causes the entire range of parameters to be dominated by superfluidity.

When the signs are opposite the inaccuracies of the graphs, especially the superfluid density and the structure factor, become so prominent that there is no logical way to try to analyze them (not shown). Trying to create any sort of phase diagram from the data becomes completely futile. One graph of the density, for  $U = 5$  and  $T = 0.6$  with opposite tunneling, gave relatively reasonable results and is presented in Fig. 4.10. The graph shows a steady increase of the density up to approximately  $\mu = 11$  and afterwards shows the staircase-like behavior that we noticed earlier for the long-ranged  $U = 20$  systems. Here however the steps are much wider and occur less frequently.

## 4.4 Conclusions

In summary, we have studied the extended Bose-Hubbard model on a square lattice with additional terms coming from density-dependent tunneling. Taking these terms into account is relevant for experiments on ultra-cold dipolar molecules in optical lattices. The competition between the density-dependent tunneling, a standard single-particle hopping, finite on-site repulsion and nearest-neighbor repulsion gives rise to a rich phase diagram of the system.

Specifically, as has been found previously [42], at large on-site repulsion and without density-dependent tunneling, there are Mott-insulator, charge density wave, superfluid and supersolid phases, as well as phase separated regions. Depending on the parameter strengths, this phase diagram undergoes considerable deformations. If either we reduce on-site repulsion or introduce density-dependent tunnelings that have the same sign as the single-particle hopping, some of the phase separated regions disappear. Remarkably, if we introduce both of these effects simultaneously,

additionally the charge density wave at half filling disappears. In this case of same-sign tunnelings, both hopping processes act constructively producing an effective larger tunneling, or respectively, weaker interactions.

We have also studied the phase diagram when the density-dependent tunneling and single-particle hopping compete due to their signs being opposite. Due to this competition, the relative importance of interaction terms is enhanced. In this case, the most striking effect is the disappearance of the supersolid into a phase separated region. This occurs on the particle-doped side of the half filling charge density wave and at strong  $V$ .

Besides a theoretical interest in understanding how density-dependent tunneling terms change phase diagrams of extended Bose-Hubbard models, our findings will help to determine where one may expect exotic phases in experiments with ultra-cold dipolar molecules in optical lattices.

# Chapter 5

## Conclusion

In this thesis we have looked at many different interesting systems which all shared the common trait of having long-ranged interactions. Mostly these interactions were dipolar (like in Ch. 2) but we also examined the effects of long-ranged hopping (in Ch. 3) and then studied the effects of having addition parameters, like density dependent hopping, added to the Hamiltonian (in Ch. 4). In each case we focused our attention on interactions that are typically neglected in simulations. We have shown repeatedly throughout this thesis that the extension of interactions beyond just the nearest neighbors or the addition of uncommon terms can have major influences on the outcomes of the phase diagrams. The Hamiltonians with the usual short-ranged interactions differed significantly from the Hamiltonians that had long-ranged interactions or extra, exotic terms. Sometimes the changes would be nothing more than the shifting of the phase transitions to a parameters yet other times there could appear entirely new phases in the systems.

In the second chapter we looked at a system of polarized bosons on an optical lattice ring. This simple system which possessed long-ranged dipolar interactions (that spanned all pairs of sites), gave a multitude of phases that had not been seen in the typical systems without dipolar interactions. Even systems with dipolar interactions usually did not extend out beyond the nearest neighbors and could not exhibit all the possible phases that can were present in our model. The first simulation was done with the dipoles being polarized perpendicular to the plane

of the ring. Besides the expected superfluid and Mott insulating phases we also saw several types of density wave phases. Many of these phase would not have been able to exist without the dipolar interactions extending to every pair of sites. In fact at the highest values of dipole-dipole repulsion all the particles retreated to a single site.

Then with the polarization lying in the plane of the ring, we were able to study the anisotropic nature of the dipolar interactions and we saw many interesting phenomena appear. The most fascinating of which showed up at high dipolar values. As the the dipole-dipole interactions increased, first we saw a splitting of the condensate into two separate sections localized in the attractive regions of the ring and later a complete symmetry breaking occurrence happened where all the bosons collapsed into a single site. (This phenomenon, although it mimics the previous results, actually comes from the anisotropic nature of the interactions rather than the long-ranged behavior.) One of the great things about this project is that the findings can easily be verified by experiments. The setup for such a small system can easily be created in a lab using techniques like the ones described in Ref. [79] and Ref. [80].

In the following chapter we examined the results of a frustrated system of hard-core bosons on a triangular lattice. By using QMC algorithms we could compare different versions of this XXZ model. We studied short-ranged interactions and compared them to interactions where the dipolar term spanned 5 nearest neighbors and finally where both the dipole-dipole interaction as well as the hopping were long-ranged. Each type of interaction gave a different phase diagram with different regions of superfluidity, crystalization, and supersolidity. It was also here that we ran into the sign problem which prevented us from exploring regions of negative hopping. Later these same regions were studied with a changing temperature in order to see how these different sections (crystal and supersolid) "melt". Models like this also have the ability to be studied experimentally and actually would be able to provide better results for the regions that exhibit the sign problem.

The results for the XXZ model with short-range tunneling apply for ultra-cold gases of polar bosonic molecules in the limit of hard-core bosons. Note that the earlier works [43, 44] have concentrated on the appearance of the supersolid phase and devil's staircase of crystalline phases in the square lattice [43], and supersolid and emulsion phases in the triangular lattice [44]. Here we focus on the hard-core-spin limit, and compare it and stress differences with other models, such as the ones with long-range tunneling, i.e., long-range XX interactions.

The results for the XXZ models with long-range tunneling apply for systems of trapped ions in triangular lattices of microtraps. These results are novel, since so far such models have been only studied using various techniques in 1D, and using the mean-field approach in 2D. While the first experimental demonstrations of such models were restricted to a few ions (see for instance [81]), many experimental groups are working on an extension of such ionic quantum simulators to systems of many ions in microtraps [82]. In fact, very recently the NIST group has engineered 2D Ising interactions in a trapped-ion quantum simulator with hundreds of spins [83]. Although in this experiment the quantum regime has not yet been achieved, it clearly opens the way toward quantum simulators of spin models with long-range interactions. We expect that in the near future the result of our present theoretical study will become directly relevant for experiments.

The final simulation was carried out on a two dimensional square lattice again using the QMC code. This section of the thesis had an addition term added to the already extended Bose-Hubbard model, the density dependent term, which can be derived from the dipolar term. The extra parameter either increased or decreased the overall tunneling depending on whether its sign was the same or opposite of the regular tunneling. Simulations showed that when the two tunneling parameters would have the same sign this would increase the supersolid and superfluid regions and decrease regions of phase separation. If on the other hand the tunneling terms had opposite signs then the the areas of phase separation would grow while supersolid and superfluid phases would diminish.

Turning on long-ranged dipolar effects introduced frustration into the system and the results were devastating. The devil's staircase-like behavior of the density caused fluctuations in the superfluidity to point that no reliable results could be attained from the simulations. As of this moment there does not seem to be a way to experimentally achieve these interactions but according to Ref. [17] this should be achievable in the near future.

A few general problems with some of the experimental setups can arise from different situations. For example the effects of frustration are a geometrical factor and will therefore show up in the experiments not just in the simulations (unlike the sign problem). So the instabilities from the meta-stable states will most likely cause as many problems for experimentalists as they do for theorists. A second major problem relates to the on-going argument about the existence of the supersolid phase. The first claim that a superfluid was observed experimentally was made in Ref. [73]. However in 2007, it was shown that what was interpreted as a supersolid could have actually been a side effect of the elasticity of helium [84]. Just recently the same team that claimed the original discovery restructured the experiment and showed that the supersolid state was completely absent [74]. This has not stopped others continuing the search for this exotic phase and there are still possibilities that in the future it will be uncovered.

Speaking of the future, there is a lot of exciting research still left in the area of long-ranged dipolar bosons. We can look forward to many new fascinating theoretical and experimental results in the near future. One of the easiest ways to improve dipolar interactions is to use atoms with higher dipole moments. Currently the popular choice has been chromium ( $^{87}\text{Cr}$ ) with a dipole moment of  $6\mu_B$  but it is still small because the length scale of the interactions is much smaller than the spacing between the particles. Recently, some research groups have been able to prepare Bose-Einstein condensates using erbium ( $^{168}\text{Er}$ ) which has a dipole moment of  $7\mu_B$  [85] and dysprosium ( $^{164}\text{Dy}$ ) which has a dipole moment of  $10\mu_B$  [86]. These atoms can take the place of the of the more commonly used chromium and provide us with a better understanding of these atomic dipole-dipole interactions. Another approach uses electric fields in order to inducing large dipole-dipole interactions.

According to Ref. [87] and Ref. [88] an AC electric field might possibly produce a large dipole by irradiating a gaseous Bose-Einstein condensate with an off-resonant laser. This process allows the dipolar interactions to be enhanced by many orders of magnitude [88]. Using this technique, Ref. [89] actually achieved large induced dipole-dipole interactions in rubidium ( $^{87}\text{Rb}$ ) Bose-Einstein condensate. Polar molecules seem to also be great candidates for studying dipolar effects. For this we need a heteronuclear diatomic molecule that has a large permanent dipole moment when it is in a low rovibrational state. If this can be achieved then we would be able to get dipole-dipole interactions on the order of a Debye [90, 91]. However scientists have not yet achieved quantum degeneracy and so we are still some time way from being able to use these molecules for experiments in quantum gases. We can also look into using Rydberg atoms to create a dipolar quantum gas. These atoms can have enormous dipole-dipole interactions (1000 times bigger than heteronuclear molecules). Unfortunately the atoms are highly sensitive to ionization and have very short lifetimes [92].

Difficulties can arise even in theoretical studies when looking at such systems in the strongly interacting regime. First of all we can no longer make assumptions along the lines of single band tight-binding approximations and taking into account only the lowest energy Wannier states. These approximations break down because such interactions mix the different bands and the different sites. Also with higher orbitals we have to take into account long-ranged hopping terms. Excited bands have been taken under consideration in several papers but serious complications appear due to the lack of convergence of the results as a function of number of bands taken into consideration. However in Ref. [93] this has been rectified using a new technique which can efficiently describe such systems.

# Appendix A

## Guide to long-ranged interactions using ALPS

The ALPS project (Algorithms and Libraries for Physics Simulations) is an open source code created for simulating strongly correlated systems in quantum mechanics. It provides the user with a multitude of tools to use for simulating many-body systems. Some of the codes included in the project are: exact diagonalization, density matrix renormalization group (DMRG), classical and quantum Monte Carlo (QMC), dynamic mean field theory (DMFT), and others. In this appendix we will only focus on the QMC code. First we will discuss some of the basics needed to get the code to run however most of that information is available on the website. Next we will give some of the more advanced methods for creating simulations with long-ranged interactions.

The first thing that we must do is to decide exactly what kind of system are we going to simulate. So let's ask a few key questions. Are we working with spins, fermions, or bosons? What type of interactions do we want in our Hamiltonian? What kind of lattice do we want to simulate and in how many dimensions? What do we want to measure? Once we have made these decisions we can get started. For the most basic simulations we can just choose a lattice from the lattice library (chain, square, triangular, cubic, etc.) and a model from the model library (spin,

boson, t-J, etc.) and we do not have to make any modifications to either of the files. We can then just choose a code and immediately start getting some results. Most simulations automatically give such values as energy, density, and stiffness but we may be interested in other observables such as the structure factor or different correlations. These extra measurements need to be added to the parameter file manually (but this is all in the tutorials so we will not spend any more time on it here).

Choosing the correct QMC code is possibly the most important thing to consider when using ALPS. Certain codes work faster for certain systems and give more precise results. It is good to keep a few guidelines in mind when choosing which code to use. For example, if you are simulating unfrustrated quantum spin models or soft-core boson models, the worms code works better. For frustrated quantum spin models or soft-core bosons (supposedly even with a sign problem) the SSE code is best. However either code can be used for either situation and sometimes it is a good idea to check one against the other. Once these fundamental steps are finished we can move on to the more difficult process of creating long-ranged simulations. First we will learn how to create a lattice that allows long-ranged interactions by making a custom unit cell. Next we will see how to adjust the definition of the model in order to create long-ranged interactions. Finally we will see how to setup the parameter file to get the program to run everything correctly. Here we will use a two dimensional triangular lattice with long-ranged interactions and the XXZ model for the examples since it will nicely demonstrate all the techniques needed to create long-ranged interactions in ALPS and also because it is the precise simulation that was studied in Chapter 3 of this thesis.

## A.1 Building the lattice

To begin it is a good idea, when creating a new lattice, to create a separate file which contains only the elements needed for your specific lattice. Here we are going to create a 2D triangular lattice with 5 nearest neighbor interactions and

periodic boundary conditions. Below we show what the xml file will look like for this kind of lattice and then we will explain what each section does exactly.

```

<LATTICES>

<LATTICE name="LR triangular lattice" dimension="2">
  <PARAMETER name="a" default="1"/>
  <BASIS>
    <VECTOR>a\text 0</VECTOR>
    <VECTOR>a/2 a*sqrt(3)/2</VECTOR>
  </BASIS>
  <RECIPROCALBASIS>
    <VECTOR>2*pi/a -2*pi/a/sqrt(3)</VECTOR>
    <VECTOR>0 4*pi/a/sqrt(3)</VECTOR>
  </RECIPROCALBASIS>
</LATTICE>

<UNITCELL name="LRtriangular" dimension="2">

  <EDGE type="1"><SOURCE vertex="1" offset="0 0"/>
  <TARGET vertex="1" offset="0 1"/></EDGE>
  <EDGE type="1"><SOURCE vertex="1" offset="0 0"/>
  <TARGET vertex="1" offset="1 0"/></EDGE>
  <EDGE type="1"><SOURCE vertex="1" offset="0 0"/>
  <TARGET vertex="1" offset="-1 1"/></EDGE>

  <EDGE type="2"><SOURCE vertex="1" offset="0 0"/>
  <TARGET vertex="1" offset="1 1"/></EDGE>
  <EDGE type="2"><SOURCE vertex="1" offset="0 0"/>
  <TARGET vertex="1" offset="-1 2"/></EDGE>
  <EDGE type="2"><SOURCE vertex="1" offset="0 0"/>
  <TARGET vertex="1" offset="-2 1"/></EDGE>

```

```
<EDGE type="3"><SOURCE vertex="1" offset="0 0"/>
<TARGET vertex="1" offset="0 2"/></EDGE>
<EDGE type="3"><SOURCE vertex="1" offset="0 0"/>
<TARGET vertex="1" offset="2 0"/></EDGE>
<EDGE type="3"><SOURCE vertex="1" offset="0 0"/>
<TARGET vertex="1" offset="-2 2"/></EDGE>

<EDGE type="4"><SOURCE vertex="1" offset="0 0"/>
<TARGET vertex="1" offset="2 1"/></EDGE>
<EDGE type="4"><SOURCE vertex="1" offset="0 0"/>
<TARGET vertex="1" offset="1 2"/></EDGE>
<EDGE type="4"><SOURCE vertex="1" offset="0 0"/>
<TARGET vertex="1" offset="-1 3"/></EDGE>
<EDGE type="4"><SOURCE vertex="1" offset="0 0"/>
<TARGET vertex="1" offset="-2 3"/></EDGE>
<EDGE type="4"><SOURCE vertex="1" offset="0 0"/>
<TARGET vertex="1" offset="-3 1"/></EDGE>
<EDGE type="4"><SOURCE vertex="1" offset="0 0"/>
<TARGET vertex="1" offset="-3 2"/></EDGE>

<EDGE type="5"><SOURCE vertex="1" offset="0 0"/>
<TARGET vertex="1" offset="0 3"/></EDGE>
<EDGE type="5"><SOURCE vertex="1" offset="0 0"/>
<TARGET vertex="1" offset="3 0"/></EDGE>
<EDGE type="5"><SOURCE vertex="1" offset="0 0"/>
<TARGET vertex="1" offset="-3 3"/></EDGE>

</UNITCELL>

<LATTICEGRAPH name = "LR triangular lattice">
```

```
<FINITELATTICE>
  <LATTICE ref="LR triangular lattice"/>
  <PARAMETER name="W" default="L"/>
  <EXTENT dimension="1" size="L"/>
  <EXTENT dimension="2" size="W"/>
  <BOUNDARY type="periodic"/>
</FINITELATTICE>
<UNITCELL ref="LRtriangular"/>
</LATTICEGRAPH>

</LATTICES>
```

We begin by giving the lattice a name. Here we have called it: LR triangular lattice. Next we define the basis and the reciprocal basis. These shouldn't change from the regular triangular lattice so they can just be copied from the already existing lattice library and pasted in to your file. At the bottom we have a definition of our lattice graph. This also needs a specific name but it can be the same as the name of the lattice so again we call it: LR triangular lattice. This section can also just be copied from the regular lattice library but it is good to give the lattices names that are unique to the simulation. The main thing that needs to be modified is the unit cell definition.

The unit cell specifically lists the each possible interaction on any given site. This unit cell is then copied onto each point of the lattice hence creating a system with as many long-ranged interactions as we want. In the above code we can see that we have 5 separately defined edges. Each edge will correspond to a different interaction that occurs at a different length. If we wanted to only have nearest neighbor interactions on the triangular lattice then we would only need to define the three edges of our triangular unit cell. To begin we have to define the source of the unit cell. Since all the sites will be exactly the same, every edge type will have the source be a vertex of type 1 and will have no offsets. Next we have to create a target for the bond (or edge). For the nearest neighbor we only have

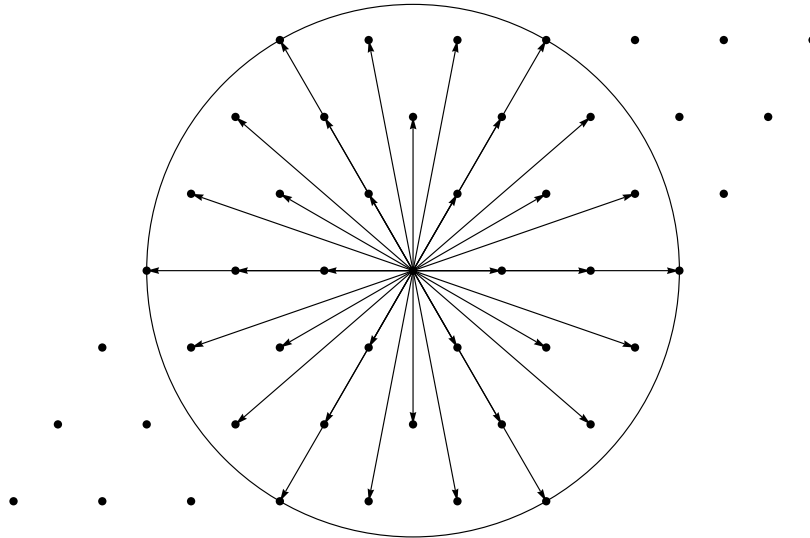


FIGURE A.1: A point on a triangular lattice with 5 nearest neighbor interactions will have 36 different bond terms.

to create a unit cell that goes to three neighboring sites because as the unit cell gets copied onto all the other sites we do not want the bonds to repeat. This is why we only need to define three bond terms in the nearest neighbor unit cell (or edge of type 1). As we can see, each consecutive bond term gets its own edge number so that it can be differentiated later in the model. The entire unit cell can be treated as a set of 5 different unit cells all with different bond lengths that are then superimposed onto each other. When the unit cell is complete it is then copied onto every single site and we get the full range of interactions. Now each site experiences 36 individual interactions at different lengths. This is shown graphically in Fig. A.1 where it is important to keep in mind that the first column and the last column are actually the same column. This is also true for the first and last row. This way the circle only overlaps on the final bonds. This will be taken into account in the parameter file that will be discussed later. So for a  $6 \times 6$  lattice we cannot have interactions farther than 5 nearest neighbors because they will calculate certain bonds more than once and give incorrect results.

## A.2 Building the model

Once the lattice is established and the unit cell is created to extend out to the correct amount of nearest neighbors, we can then create a model that will utilize this lattice. Here we will focus on the long-ranged XXZ model used in Chapter 3. This model as we recall has hard-core bosons that have both long-ranged tunneling and dipole-dipole repulsion.

The first step is to choose a sitebasis and a basis. Here we are working with bosons so we can just copy and paste the required information from the model library in the ALPS program. There are two ways to do this since there exist separate bases for hard-core and soft-core bosons. In this file the soft-core model is chosen since it can then be restricted to the hard-core limit in the parameter file and therefore allows for more options without having to create a new model. For this section of the code no changes are required whether the interactions are short-ranged or long-ranged. We can see this in the sample code provided below.

```
<MODELS>
  <SITEBASIS name="boson">
    <PARAMETER name="Nmax" default="infinity"/>
    <QUANTUMNUMBER name="N" min="0" max="Nmax"/>
    <OPERATOR name="bdag" matrixelement="sqrt(N+1)">
      <CHANGE quantumnumber="N" change="1"/>
    </OPERATOR>
    <OPERATOR name="b" matrixelement="sqrt(N)">
      <CHANGE quantumnumber="N" change="-1"/>
    </OPERATOR>
    <OPERATOR name="n" matrixelement="N"/>
  </SITEBASIS>

  <BASIS name="boson">
    <SITEBASIS ref="boson"/>
```

```

    <CONSTRAINT quantumnumber="N" value="N_total"/>
</BASIS>

<HAMILTONIAN name="XXZ">
  <PARAMETER name="mu" default="0"/>

  <PARAMETER name="J1" default="0"/>
  <PARAMETER name="J2" default="0"/>
  <PARAMETER name="J3" default="0"/>
  <PARAMETER name="J4" default="0"/>
  <PARAMETER name="J5" default="0"/>

  <BASIS ref="boson"/>
  <SITETERM site="i">
    <PARAMETER name="mu#" default="mu"/>
    -mu#*(n(i)-(1/2))
  </SITETERM>

  <BONDTERM source="i" target="j">
    <PARAMETER name="J#" default="0"/>
    J#*(cos(theta)*(n(i)*n(j)-n(i)/2-n(j)/2+1/4)
      +(sin(theta)/2)*(bdag(i)*b(j)+b(i)*bdag(j)))
  </BONDTERM>
</HAMILTONIAN>
</MODELS>

```

The important changes occur in the Hamiltonian. Here we are modeling Hamiltonian 3.1. We see that the two parameters that define the interactions are  $\mu$ , the chemical potential  $J$  the long-ranged interaction term. As we can see we have a single parameter for the chemical potential and we have 5 parameters for the  $J$  term. Each one of the parameters will correspond to a different neighbor. So  $J1$

is the nearest neighbors,  $J_2$  the next nearest neighbors and so on. The default values are set here to zero but these can be changed easily in the parameter file allowing to us to choose any length of interactions from 1 to 5 nearest neighbors. The Hamiltonian is broken up into two terms: the site term and the bond term. The site terms, usually the on-site repulsion  $U$  and chemical potential  $\mu$ , are the values summed over a single index. The bond terms, usually the tunneling  $J$  and dipolar repulsion  $V$ , are the terms with a sum over two indices. The  $J\#$  term in the Hamiltonian will allow us to set all the individual  $J$ 's in the parameter file. Also we see that there is a theta term in the Hamiltonian that we can also be set in the parameter file.

### A.3 Building the parameter file

Finally we can create our parameter file. We begin by choosing our lattice and model from the files that we have just created. Next we choose the values we want for all of our parameters from the Hamiltonian. So here we have entered values in such a way that the potentials change as  $1/r^3$ . Each  $J$  corresponds to the value of a particular nearest neighbor. Next we limit the bosons to only allow one per site in order to attain the hard-core limit. Then we choose our temperature low enough so that we do not have excitations in the simulations since we are interested in getting the ground state. Next we enter any additional observables that we want to calculate. In the sample code below we have decide to calculate some additional correlations. Finally we set our thermalization and sweeps and we are ready to scan over the  $\mu$  parameter and get the results. To run the program just follow the simple steps in the tutorial online.

```
LATTICE_LIBRARY="./lattice.xml";
LATTICE="LR triangular lattice";

MODEL_LIBRARY="./model.xml";
MODEL="XXZ";
```

```
L=6

dist1=1;
dist2=sqrt(3);
dist3=2;
dist4=sqrt(7);
dist5=3;

theta  = -0.15;
pot    = 1.0;

J1     = pot*(1/dist1^3);
J2     = pot*(1/dist2^3);
J3     = pot*(1/dist3^3);
J4     = pot*(1/dist4^3);
J5     = pot*(1/dist5^3)/2;

Nmax=1
T=0.1
MEASURE[Correlations]=true;

THERMALIZATION=600000;
SWEEPS=900000;

{mu = 0.001;}
{mu = 0.1;}
{mu = 0.2;}
{mu = 0.3;}
{mu = 0.4;}
{mu = 0.5;}
```

As a final note, it is good to know how to adjust the sweeps and thermalization for the simulations. These two parameters are very important because they decide how effectively the simulation will run. The sweeps are the number of Monte Carlo steps that are performed after thermalization. Thermalization are just the first Monte Carlo steps that are performed and then discarded before any of the statistics are calculated. A large number of sweeps and thermalization will give more precise answers but will take a longer time to calculate. However if they are chosen to be too small then the code might not converge and this can cause large errors in the results. It is good to play with these parameters until one gets "a good feel" for them. The best way to start is to run through the Worms and SSE tutorials on the ALPS website and adjust these parameters accordingly to one's own specific simulation.

# Bibliography

- [1] R. P. Feynman. Simulating physics with computers. *Int. J. Theor. Phys.*, 21 (467), 1982.
- [2] D. Deutsch. Quantum computational networks. *Proc. R. Soc. Lond. A*, 425 (1868), 1989.
- [3] P. W. Shor. Algorithms for quantum computation: Discrete logarithms and factoring. In *FOCS*, pages 124–134. IEEE Computer Society, 1994.
- [4] M. H. Anderson, J. R. Ensher, M. R. Matthews, C. E. Wieman, and E. A. Cornell. Observation of bose-einstein condensation in a dilute atomic vapor. *Science*, 269(5221), 1995.
- [5] M. Greiner, C.A. Regal, and D.S. Jin. emergence of a molecular bose–einstein condensate from a fermi gas. *Nature*, 426(537), 2003.
- [6] C. A. Regal, M. Greiner, and D. S. Jin. Observation of resonance condensation of fermionic atom pairs. *Phys. Rev. Lett.*, 92(040403), 2004.
- [7] M. Greiner, O. Mandel, T. Esslinger, T. W. Hänsch, and I. Bloch. Quantum phase transition from a superfluid to a mott insulator in a gas of ultracold atoms. *Nature*, 415(39), 2002.
- [8] D. Jaksch, C. Bruder, J. I. Cirac, C. W. Gardiner, and P. Zoller. Cold bosonic atoms in optical lattices. *Phys. Rev. Lett.*, 81(3108), 1998.
- [9] J. Hubbard. Electron correlations in narrow energy bands. *Proc. R. Soc. Lond. A*, 276(1365), 1963.

- 
- [10] H. A. Gersch and G. C. Knollman. Quantum cell model for bosons. *Phys. Rev.*, 129(959), 1963.
- [11] T. Lahaye, C. Menotti, L. Santos, M. Lewenstein, and T. Pfau. The physics of dipolar bosonic quantum gases. *Rep. Prog. Phys.*, 72(12), 2009.
- [12] T. Köhler, K. Góral, and P. S. Julienne. Production of cold molecules via magnetically tunable feshbach resonances. *Rev. Mod. Phys.*, 78(4), 2006.
- [13] C. Chin, R. Grimm, P. Julienne, and E. Tiesinga. Feshbach resonances in ultracold gases. *Rev. Mod. Phys.*, 82(1225), 2010.
- [14] A. Eckardt, C. Weiss, and M. Holthaus. Superfluid-insulator transition in a periodically driven optical lattice. *Phys. Rev. Lett.*, 95(260404), 2005.
- [15] A. Eckardt, P. Hauke, P. Soltan-Panahi, C. Becker, K. Sengstock, and M. Lewenstein. Frustrated quantum antiferromagnetism with ultracold bosons in a triangular lattice. *Eur. Phys. Lett.*, 89(10010), 2010.
- [16] A. Zenesini, H. Lignier, D. Ciampini, O. Morsch, , and E. Arimondo. Coherent control of dressed matter waves. *Phys. Rev. Lett.*, 102(100403), 2009.
- [17] T. Sowiński, O. Dutta, P. Hauke, L. Tagliacozzo, and M. Lewenstein. Dipolar molecules in optical lattices. *Phys. Rev. Lett.*, 108(115301), 2012.
- [18] J. I. Cirac and P. Zoller. Quantum computations with cold trapped ions. *Phys. Rev. Lett.*, 74(4091), 1995.
- [19] D. Porras and J. I. Cirac. Effective quantum spin systems with trapped ions. *Phys. Rev. Lett.*, 92(207901), 2004.
- [20] D. Porras and J. I. Cirac. Quantum manipulation of trapped ions in two dimensional coulomb crystals. *Phys. Rev. Lett.*, 96(250501), 2006.
- [21] B. Bauer, L. D. Carr, H. G. Evertz, A. Feiguin, J. Freire, S. Fuchs, L. Gamper, J. Gukelberger, E. Gull, S. Guertler, A. Hehn, R. Igarashi, S. V. Isakov, D. Koop, P. N. Ma, P. Mates, H. Matsuo, O. Parcollet, G. Pawłowski, J. D. Picon, L. Pollet, E. Santos, V. W. Scarola, U. Schollwöck, C. Silva, B. Surer,

- S. Todo, S. Trebst, M. Troyer, M. L. Wall, P. Werner, and S. Wessel. The alps project release 2.0: open source software for strongly correlated systems. *J. Stat. Mech.*, P05001, 2011.
- [22] K. Góral, L. Santos, and M. Lewenstein. Quantum phases of dipolar bosons in optical lattices. *Phys. Rev. Lett.*, 88(170406), 2002.
- [23] E. G. Dalla Torre, E. Berg, and E. Altman. Hidden order in 1d bose insulators. *Phys. Rev. Lett.*, 97(260401), 2006.
- [24] X. Deng and L. Santos. Entanglement spectrum of one-dimensional extended bose-hubbard models. *Phys. Rev. B*, 85(085138), 2011.
- [25] S. Müller, J. Billy, E. A. L. Henn, H. Kadau, A. Griesmaier, M. Jona-Lasinio, L. Santos, and T. Pfau. Stability of a dipolar bose-einstein condensate in a one-dimensional lattice. *Phys. Rev. A*, 84(053601), 2011.
- [26] R. M. Wilson and J. L. Bohn. Emergent structure in a dipolar bose gas in a one-dimensional lattice. *Phys. Rev. A*, 83(023623), 2011.
- [27] T. Roscilde and M. Boninsegni. Off-diagonal correlations in a one-dimensional gas of dipolar bosons. *New J. Phys.*, 12(033032), 2010.
- [28] R. B. Lehoucq, D. C. Sorensen, and C. Yang. Arpack users guide: Solution of large scale eigenvalue problems by implicitly restarted arnoldi methods., 1997.
- [29] C. Lanczos. An iteration method for the solution of the eigenvalue problem of linear differential and integral operators. *J. Res. Nat. Bureau Standards*, 45(255), 1950.
- [30] G. G. Batrouni and R. T. Scalettar. World-line quantum monte carlo algorithm for a one-dimensional bose model. *Phys. Rev. B*, 46(9051), 1992.
- [31] E. J. Mueller, T. Ho, M. Ueda, and G. Baym. Fragmentation of bose-einstein condensates. *Phys. Rev. A*, 73(033612), 2006.

- 
- [32] R. Roth and K. Burnett. Phase diagram of bosonic atoms in two-color superlattices. *Phys. Rev. A*, 68(023604), 2003.
- [33] S. Zöllner, G. M. Brunn, C. J. Pethick, and S. M. Reimann. Bosonic and fermionic dipoles on a ring. *Phys. Rev. Lett.*, 107(035301), 2011.
- [34] R. W. Spekkens and J. E. Sipe. Spatial fragmentation of a bose-einstein condensate in a double-well potential. *Phys. Rev. A*, 59(3868), 1999.
- [35] M. W. Jack and M. Yamashita. Bose-hubbard model with attractive interactions. *Phys. Rev. A*, 71(023610), 2005.
- [36] M. Abad, M. Guilleumas, R. Mayol, M. Pi, and D. M. Jezek. Dipolar condensates confined in a toroidal trap: Ground state and vortices. *Phys. Rev. A*, 81(043619), 2010.
- [37] P. Hauke, F. M. Cucchietti, L. Tagliacozzo, I. Deutsch, and M. Lewenstein. Can one trust quantum simulators? *Rep. Prog. Phys.*, 75(082401), 2011.
- [38] D. Peter, S. Müller, S. Wessel, and H. P. Büchler. Anomalous behavior of spin systems with dipolar interactions. *Phys. Rev. Lett.*, 109(025303), 2012.
- [39] R. Barnett, D. Petrov, M. Lukin, and E. Demler. Quantum magnetism with multicomponent dipolar molecules in an optical lattice. *Phys. Rev. Lett.*, 96(190401), 2006.
- [40] A. V. Gorshkov, S. R. Manmana, G. Chen, J. Ye, E. Demler, M. D. Lukin, and A. M. Rey. Tunable superfluidity and quantum magnetism with ultracold polar molecules. *Phys. Rev. Lett.*, 107(115301), 2011.
- [41] G. G. Batrouni, F. Hébert, and R. T. Scalettar. Supersolid phases in the one-dimensional extended soft-core bosonic hubbard model. *Phys. Rev. Lett.*, 97(087209), 2006.
- [42] P. Sengupta, L. P. Pryadko, F. Alet, M. Troyer, and G. Schmid. Supersolids versus phase separation in two-dimensional lattice bosons. *Phys. Rev. Lett.*, 94(207202), 2005.

- [43] B. Capogrosso-Sansone, C. Trefzger, M. Lewenstein, P. Zoller, and G. Pupillo. Quantum phases of cold polar molecules in 2d optical lattices. *Phys. Rev. Lett.*, 104(125301), 2010.
- [44] L. Pollet, J. D. Picon, H.P. Büchler, and M. Troyer. Supersolid phase with cold polar molecules on a triangular lattice. *Phys. Rev. Lett.*, 104(125302), 2010.
- [45] C. Menotti, C. Trefzger, and M. Lewenstein. Metastable states of a gas of dipolar bosons in a 2d optical lattice. *Phys. Rev. Lett.*, 98(235301), 2007.
- [46] C. Trefzger, C. Menotti, and M. Lewenstein. Ultracold dipolar gas in an optical lattice: The fate of metastable states. *Phys. Rev. A*, 78(043604), 2008.
- [47] T. Ohgoe, T. Suzuki, and N. Kawashima. Quantum phases of hard-core bosons on two-dimensional lattices with anisotropic dipole-dipole interaction. *Phys. Rev. A*, 86(063635), 2012.
- [48] P. Hauke, F. M. Cucchietti, A. Müller-Hermes, M. Ba nuls, J. I. Cirac, and M. Lewenstein. Complete devil's staircase and crystalsuperfluid transitions in a dipolar xxz spin chain: a trapped ion quantum simulation. *New J. Phys.*, 12(113037), 2010.
- [49] P. Bak and R. Bruinsma. One-dimensional ising model and the complete devil's staircase. *Phys. Rev. Lett.*, 49(249), 1982.
- [50] X. L. Deng, D. Porras, and J. I. Cirac. Effective spin quantum phases in systems of trapped ions. *Phys. Rev. A*, 72(063407), 2005.
- [51] J. Freericks and H. Monien. Strong-coupling expansions for the pure and disordered bose-hubbard model. *Phys. Rev. B*, 53(2691), 1996.
- [52] M. Maik, P. Buonsante, A. Vezzani, and J. Zakrzewski. Dipolar bosons on an optical lattice ring. *Phys. Rev. A*, 84(053615), 2011.

- 
- [53] R. Citro, E. Orignac, S. De Palo, and M. L. Chiofalo. Evidence of luttinger-liquid behavior in one-dimensional dipolar quantum gases. *Phys. Rev. A*, 75(051602), 2007.
- [54] R. Citro, S. De Palo, E. Orignac, P. Pedri, and M. L. Chiofalo. Luttinger hydrodynamics of confined one-dimensional bose gases with dipolar interactions. *New J. Phys.*, 10(045011), 2008.
- [55] M. Dalmonte, G. Pupillo, and P. Zoller. One-dimensional quantum liquids with power-law interactions: The luttinger staircase. *Phys. Rev. Lett.*, 105(140401), 2010.
- [56] S. Wessel and M. Troyer. Supersolid hard-core bosons on the triangular lattice. *Phys. Rev. Lett.*, 95(127205), 2005.
- [57] D. Heidarian and K. Damle. Persistent supersolid phase of hard-core bosons on the triangular lattice. *Phys. Rev. Lett.*, 95(127206), 2005.
- [58] R. G. Melko, A. Paramekanti, A. A. Burkov, A. Vishwanath, D. N. Sheng, and L. Balents. Supersolid order from disorder: Hard-core bosons on the triangular lattice. *Phys. Rev. Lett.*, 95(127207), 2005.
- [59] F. J. Burnell, M. M. Parish, N. R. Cooper, and S. L. Sondhi. Devils staircases and supersolids in a one-dimensional dipolar bose gas. *Phys. Rev. B*, 80(174519), 2009.
- [60] H. Ozawa and I. Ichinose. Phase structure of repulsive hard-core bosons in a stacked triangular lattice. *Phys Rev. A*, 86(015601), 2012.
- [61] M. Lewenstein, A. Sanpera, V. Ahufinger, B. Damski, A. Sen De, and U. Sen. Ultracold atomic gases in optical lattices: mimicking condensed matter physics and beyond. *Adv.Phys.*, 56(243), 2007.
- [62] I. Bloch, J. Dalibard, and W. Zwerger. Many-body physics with ultracold gases. *Rev. Mod. Phys.*, 80(885), 2008.
- [63] J. E. Hirsch. Superconductivity. *Physica C*, 158(326), 1989.

- 
- [64] O. Dutta, A. Eckardt, P. Hauke, B. Malomed, and M. Lewenstein. Bose–hubbard model with occupation-dependent parameters. *New J. Phys.*, 13(023019), 2011.
- [65] D.-S. Lühmann, O. Jrgensen, and K. Sengstock. Multi-orbital and density-induced tunneling of bosons in optical lattices. *New J. Phys.*, 14(033021), 2012.
- [66] M. Lacki, D. Delande, and J. Zakrzewski. Dynamics of cold bosons in optical lattices: effects of higher bloch bands. *New J. Phys.*, 15(013062), 2013.
- [67] U. Bissbort, F. Deuretzbacher, and W. Hofstetter. Effective multi-body induced tunneling and interactions in the bose-hubbard model of the lowest dressed band of an optical lattice. *Phys. Rev. A*, 86(023617), 2012.
- [68] A. Mering and M. Fleischhauer. Multiband and nonlinear hopping corrections to the three-dimensional bose-fermi-hubbard model. *Phys. Rev. Lett.*, 83(063630), 2011.
- [69] C. Ospelkaus, S. Ospelkaus, K. Sengstock, and K. Bongs. Interaction-driven dynamics of k40-rb87 fermion-boson gas mixtures in the large-particle-number limit. *Phys. Rev. Lett.*, 96(020401), 2006.
- [70] K. Günter, T. Stöferle, H. Moritz, M. Köhl, and T. Esslinger. Bose–fermi mixtures in a three-dimensional optical lattice. *Phys. Rev. Lett.*, 96(180402), 2006.
- [71] J. Catani, L. De Sarlo, G. Barontini, F. Minardi, and M. Inguscio. Degenerate bose-bose mixture in a three-dimensional optical lattice. *Phys. Rev. A*, 77(011603), 2008.
- [72] E. Kim and M. H. W. Chan. Probable observation of a supersolid helium phase. *Nature*, 427(225), 2004.
- [73] E. Kim and M. H. W. Chan. Observation of superflow in solid helium. *Science*, 305(5692), 2004.

- 
- [74] D. Y. Kim and M. H. W. Chan. Absence of supersolidity in solid helium in porous vycor glass. *Phys. Rev. Lett.*, 109(155301), 2012.
- [75] A. B. Kuklov, N.V. Prokof'ev, and B. V. Svistunov. How solid is supersolid? *Physics*, 4(109), 2011.
- [76] T. Takekoshi, M. Debatin, R. Rameshan, F. Ferlaino, R. Grimm, H. Nägerl, C. R. Le Sueur, J. M. Hutson, P. S. Julienne, S. Kotochigova, and E. Tiemann. Towards the production of ultracold ground-state rbc molecules: Feshbach resonances, weakly bound states, and the coupled-channel model. *Phys. Rev. A*, 85(032506), 2012.
- [77] K. Aikawa, D. Akamatsu, M. Hayashi, K. Oasa, J. Kobayashi, P. Naidon, T. Kishimoto, M. Ueda, and S. Inoué. Coherent transfer of photoassociated molecules into the rovibrational ground state. *Phys. Rev. Lett.*, 105(203001), 2010.
- [78] L. Bonnes and S. Wessel. Pair superfluidity of three-body constrained bosons in two dimensions. *Phys. Rev. Lett.*, 106(185302), 2011.
- [79] J. F. Sherson, C. Weitenberg, M. Endres, M. Cheneau, I. Bloch, and S. Kuhr. Single-atom-resolved fluorescence imaging of an atomic mott insulator. *Nature*, 467(7311), 2010.
- [80] C. Weitenberg, M. Endres, J. F. Sherson, M. Cheneau, P. Schauf, T. Fukuhara, I. Bloch, and S. Kuhr. Single-spin addressing in an atomic mott insulator. *Nature*, 471(7338), 2011.
- [81] A. Friedenauer, H. Schmitz, J. T. Glueckert, D. Porras, and T. Schaetz. Simulating a quantum magnet with trapped ions. *Nat. Phys.*, 4(757), 2008.
- [82] D. Wineland, C. Monroe, T. Schätz, and R. Blatt. private communication, 2012.

- 
- [83] J.W. Britton, B.C. Sawyer, A.C. Keith, C.-C.J. Wang, J.K. Freericks, H. Uys, M.J. Biercuk, and J.J. Bollinger. Engineered two-dimensional ising interactions in a trapped-ion quantum simulator with hundreds of spins. *Nature*, 484(489), 2012.
- [84] H. J. Maris. Effect of elasticity on torsional oscillator experiments probing the possible supersolidity of helium. *Phys. Rev. B*, 86(020502), 2012.
- [85] K. Aikawa, A. Frisch, M. Mark, S. Baier, A. Rietzler, R. Grimm, and F. Ferlaino. Bose-einstein condensation of erbium. *Phys. Rev. Lett.*, 108(210401), 2012.
- [86] M. Lu, N. Q. Burdick, S. Youn, and B. L. Lev. Strongly dipolar bose-einstein condensate of dysprosium. *Phys. Rev. Lett.*, 107(190401), 2011.
- [87] I. E. Mazets, D. H. J. Odell, G. Kurizki, N. Davidson, and W. P. Schleich. Depletion of a bose-einstein condensate by laser-induced dipole-dipole interactions. *Journal of Physics B: Atomic, Molecular and Optical Physics*, 37(S155), 2004.
- [88] D. H. J. Odell, S. Giovanazzi, and G. Kurizki. Roton in gaseous bose-einstein condensates irradiated by a laser. *Phys. Rev. Lett.*, 90(110402), 2003.
- [89] R. Mottl, F. Brennecke, K. Baumann, R. Landig, T. Donner, and T. Esslinger. Roton-type mode softening in a quantum gas with cavity-mediated long-range interactions. *Science*, 336(6088), 2012.
- [90] K. K. Ni, S. Ospelkaus, M. H. G. de Miranda, A. Pe'er, B. Neyenhuis, J. J. Zirbel, S. Kotochigova, P. S. Julienne, D. S. Jin, and J. Ye. A high phase-space-density gas of polar molecules. *Science*, 322(5899), 2008.
- [91] J. Deiglmayr, A. Grochola, M. Repp, K. Mörzlbauer, C. Glück, J. Lange, O. Dulieu, R. Wester, and M. Weidemüller. Formation of ultracold polar molecules in the rovibrational ground state. *Phys. Rev. Lett.*, 101(133004), 2008.

- 
- [92] W. Li, M. W. Noel, M. P. Robinson, P. J. Tanner, T. F. Gallagher, D. Comparat, B. Laburthe Tolra, N. Vanhaecke, T. Vogt, N. Zahzam, P. Pillet, and D. A. Tate. Evolution dynamics of a dense frozen rydberg gas to plasma. *Phys. Rev. A*, 70(042713), 2004.
- [93] O. Dutta, M. Lewenstein, and J. Zakrzewski. Frustration by population trapping with polar molecules. *arXiv:1310.7757*, 2013.